

# **Biaxial apparatus testing for dike stability assessment**

MSc Thesis Project  
Geo Engineering AESM2606  
Technische Universiteit Delft

**Student:**

Matthijs Bölger

**Student number:**

4484983

**Reviewer:**

Dr. Ir. Cor Zwanenburg

**Thesis Committee:**

Dr. Ir. Cor Zwanenburg – Technical University Delft, Geo-Engineering  
Dr. Ir. Ronald Brinkgreve - Technical University Delft, Geo-Engineering  
Dr. Ir. Stefano Muraro - Technical University Delft, Geo-Engineering  
Dr. Ir. Hans Teunissen – Deltares  
Dr. Ir. Cong Mai Van - Technical University Delft, Hydraulic Engineering

# Table of Contents

<b>Abstract .....</b>	<b>5</b>
<b>1. Introduction .....</b>	<b>6</b>
1.1. Background .....	6
1.2. Problem description .....	6
1.3. Research Questions .....	8
1.4. Methodology .....	8
<b>2. Biaxial apparatus .....</b>	<b>10</b>
2.1. Plane strain conditions .....	10
2.2. Biaxial devices .....	14
2.3. Biaxial apparatus by Allersma (1993) .....	18
2.4. Test procedure by Allersma (1993) .....	21
2.5. Improvements of biaxial device .....	24
2.5.1. Technical specifications and safety .....	24
2.5.2. Input panel and apparatus control .....	26
2.5.3. Desired improvements .....	27
2.6. Preliminary testing phase .....	27
2.7. Adjustments after preliminary tests .....	30
2.7.1. Alternation of bottom plate .....	30
2.7.2. Adjustment of pore pressure measurement system .....	32
2.7.3. Uncontrolled drained conditions at the biaxial cell boundaries .....	33
<b>3. Material Description .....</b>	<b>34</b>
3.1. OVP clay in literature .....	34
3.2. OVP clay used .....	38
<b>4. Numerical pre-analysis .....</b>	<b>39</b>
4.1. PLAXIS soil test .....	39
4.2. PLAXIS 2D .....	41
4.2.1. Project Properties .....	41
4.2.2. Material selection .....	42
4.2.3. Initial stress configuration .....	42
4.2.5. Biaxial test set up in PLAXIS2D .....	44
4.2.5.1. Groundwater flow boundary conditions .....	44
4.2.5.2. Biaxial loading .....	46
4.2.5.3. 1D consolidation .....	50
4.2.5.4. Biaxial shearing .....	51
4.2.5.5. Excess pore pressure development during biaxial shearing .....	53
4.3. PLAXIS 3D .....	55

4.3.1. Project properties .....	55
4.3.2. Initial stress configuration .....	56
<b>4.4. Biaxial test set up in PLAXIS3D .....</b>	<b>57</b>
4.4.1. Groundwater flow boundary conditions .....	57
4.4.2. Biaxial loading .....	58
4.4.3. Biaxial shearing .....	62
<b>5. Biaxial test results .....</b>	<b>63</b>
<b>5.1. Test results .....</b>	<b>63</b>
5.1.1. Test 1 .....	63
5.1.2. Test 2 .....	65
5.1.3. Test 3 .....	71
5.1.4. Test 4 .....	74
5.1.4. Test 5 .....	78
<b>5.2. Numerical simulation for laboratory tests .....</b>	<b>79</b>
5.2.1. Numerical analysis test 1 .....	79
5.2.2. Numerical analysis test 2 .....	80
5.2.3. Numerical analysis test 3 .....	83
5.2.4. Numerical analysis test 4 .....	84
<b>5.3. Conclusions test results .....</b>	<b>87</b>
5.3.1. Conclusion test 1 .....	87
5.3.2. Conclusion test 2 .....	87
5.3.3. Conclusion test 3 .....	88
5.3.4. Conclusion test 4 .....	91
5.3.5. Conclusion test 5 .....	94
<b>6. Yield Surface Representation .....</b>	<b>95</b>
6.1. Yield criterion .....	95
6.2. Strength criterion representation .....	96
6.3. Stress invariants .....	98
<b>7. Yield surfaces and criteria .....</b>	<b>101</b>
7.1. Mohr-Coulomb failure criterion .....	101
7.2. Drucker Prager .....	102
7.3. Matsuoka-Nakai failure criterion .....	103
7.3. Lagioia and Panteghini .....	105
7.4. Teunissen (2022) .....	107
7.5. Plane strain parameters versus axial symmetric parameters .....	108
<b>8. Conclusion .....</b>	<b>109</b>
<b>9. Discussion and recommendations .....</b>	<b>111</b>
9.1. Technical specifications .....	111
9.2. Biaxial test set up .....	112
9.3. Numerical analysis .....	113
9.4. Future recommendations .....	113
<b>10. References .....</b>	<b>115</b>

<b>Appendix A. Pore pressure measurement. ....</b>	<b>119</b>
<b>Appendix B. General relation stress invariants .....</b>	<b>125</b>
<b>Appendix C. Constitutive models .....</b>	<b>126</b>
<b>C.1 Elasticity .....</b>	<b>126</b>
<b>C.2 Elastoplastic model .....</b>	<b>127</b>
<b>C.3 Cam-clay model.....</b>	<b>128</b>
<b>C.4 Soft Soil Model.....</b>	<b>130</b>

# Abstract

Stability assessment for dikes and dike reinforcement requires insight in soil strength behaviour. The required parameters for this assessment are typically obtained from conventional laboratory tests. These conventional tests are not performed under conditions found in the field. For example, a dike section resembles to plane strain conditions. Limited research is available for laboratory test under plane strain conditions, especially for organic clays. The plane strain biaxial apparatus presented by Allersma (1993) is used to perform tests on organic clay. The apparatus has not been used for several decades and it is described how the machine is refurbished. Preliminary tests and further improvements lead to familiarization with the apparatus. After this stage, laboratory tests on organic clay are performed and presented. The soil sample is loaded, leading to stress and pore pressure measurement. The measurements from laboratory tests are presented in chronological order. Several test set ups, most notably varying in their method to control the drainage conditions and to measure the pore pressure, are used. Assessment of the standard of these results in terms of accuracy, reliability and reproductivity is given. A notable challenge arising in the tests, is the uncontrolled drainage boundaries at the boundary between soil sample and soil sample enclosure: the biaxial cell. Conclusions are drawn from individual tests and consequentially improvements are made on the test set up. The test is re-created and numerically analysed in finite element programmes PLAXIS2D and PLAXIS3D. The numerical analysis and laboratory are compared and help to understand and predict the stress conditions found during tests in the laboratory. Remaining challenges are discussed on technical specifications and laboratory test set up. Concluded is that tests with this biaxial apparatus do not lead to results of a sufficiently high standard for further soil testing.

# 1. Introduction

## 1.1. Background

Dikes are constructed to protect land vulnerable to flooding. In low-lying regions, such as the Netherlands, high safety standards are prescribed for dikes and dike reinforcement. Stability assessment following these standards require a thorough insight in soil strength behaviour. The required parameters for this assessment are typically determined using the strength from conventional laboratory tests (van Duinen, 2014). Namely, triaxial compression, triaxial extension and direct simple shear tests. These laboratory tests are conducted on cylindrical samples which have a uniform radial stress. This may not resemble to the stress conditions found in the field. For example, a cross section of a dike segment has different horizontal stresses perpendicular and parallel to the dike.

The triaxial compression and triaxial extension tests are performed under axial symmetric conditions, where a soil sample is under the same conditions if rotated around the symmetric axis. Again, this may not correspond to the conditions found if considering a dike segment. A dike can be considered an infinitely lengthy component constrained by large mass on either side along this length axis. These conditions resemble to plane strain conditions. This implies two perpendicular directions with non-zero strains which form a two-dimensional plane. In the direction normal to this plane there is zero strain. The direction of zero-strain resembling to the ‘infinitely’ long direction of the dike.

Different stress conditions occur for axial symmetric and plane strain tests, leading to different stress behaviour (Zwanenburg et al., 2019). Calculations for plane strain field conditions are generally based on stress behaviour from axial symmetric laboratory tests (Zwanenburg et al., 2019). This mismatch can be remedied by conducting plane strain laboratory tests for plane strain design calculations.

The Technical University Delft has testing facility allowing for laboratory soil tests under plane strain conditions. The is the biaxial apparatus designed and presented by Allersma (1993). It is one of the few devices allowing for plane strain tests and experimental evidence with the biaxial device is limited.

## 1.2. Problem description

The biaxial device at the Technical University Delft is used for soil testing in this thesis. There are several problems to overcome before getting useful results. The apparatus has not been used for 18 years and was not workable at the start of this research work. Extensive refurbishments have been made on the apparatus to get it back to a usable state. This includes efforts on control, safety, stress measurement, drainage conditions and reliability of the device.

After these improvements, the first challenge is to assess the working of the apparatus thoroughly. There are two parts in this. First, the technical working of the apparatus such as stress measurement and control of the apparatus. Secondly, the working of the apparatus with soils. This might uncover the presence of several undesired phenomena. One of the most difficult proving to be the control of the drainage conditions. Other

examples including, undesired presence of friction, presence of air in the test set up and inconsistent stress measurements with identical displacement schemes exerted on the same soil.

The second challenge of the tests is to get reliable results with the biaxial apparatus. A soil sample can be tested with the biaxial apparatus by applying displacements, with a known displacement rate, under plane strain conditions. Loading is applied to the soil and the outcome is obtained in the form of stress measurements. These two, the displacements and resulting stress measurements, should fit to make the test reliable. Also, the tests should be reproducible to be reliable.

The process towards reliable results is fragile and little reference is available. Increasing confidence and understanding in the obtained biaxial laboratory results is necessary. To do this, the laboratory tests are performed hand in hand to a corresponding numerical analysis. The laboratory tests with the biaxial apparatus are recreated numerically. This is done using PLAXIS2D and PLAXIS3D, special purpose finite element programs used to perform numerical analysis for geotechnical applications. The analysis has three main purposes. Firstly, the numerical analysis is done to predict behaviour of the biaxial soil tests. Secondly, it aids in selection of valuable tests to be performed in the laboratory. Thirdly, it helps to understand and validate the results obtained. To do this, the intended and performed laboratory biaxial displacement schemes are re-created in the program. The soil parameters from previous laboratory analyses are incorporated into the numerical analysis.

The third challenge is to load the soil towards stress conditions leading to failure. Different stress configurations, compared to the conventional tests, are expected to be found if plane strain conditions are met. This difference in stress conditions can be represented with a failure criterion which describes the condition for which the stress is too large, and a soil will fail. This failure condition for the previously mentioned conventional tests are relatively well known. The stress conditions and its failure criteria for a biaxial apparatus is less known. Performing test under the conditions of the biaxial apparatus might lead to new insights on the failure criteria and the strength of soils. They are represented in the form of a 3D strength criterium (Zwanenburg et al., 2019). An organic clay soil is used for these tests and is also used for the biaxial tests. In a later stage, when confidence is gained in the working of the apparatus, the soil is loaded towards failure. If the stress conditions are represented by a 3D strength criterium, a comparison can be made between the strength for tests with conventional devices and the biaxial device.

Executing the third challenge, described in the previous paragraph, proved to be too complex within the works of this thesis. As several obstacles, presented in this thesis, had to be overcome. It is discussed if it is feasible to tackle the third challenge, and other types of laboratory tests, with the biaxial device in future studies.

There lies interest in documenting the method to achieving these challenges. One of the major problems faced in this work is the lack of reference on plane strain biaxial testing with this type of soil. Also, there is limited research on working of this biaxial apparatus. Advising and recommending the steps to be taken with the biaxial device will be beneficial for future studies.

### 1.3. Research Questions

The main challenge is to verify plane strain results with organic clay using the biaxial device. As mentioned, results are obtained by displacing a soil and recording the stresses. The two should fit to one another. To gain trust in this, the laboratory results are compared to PLAXIS2D and PLAXIS3D in which the laboratory set up is re-created. Also, the tests should be reproducible to prove verifiable. This gives the research question: *Are the results on organic clay with the biaxial device verifiable?*

To be able to answer this question the first sub question needs to be treated: *What challenges should be overcome to get results with the biaxial device?* This research question aims to describe the pathway towards results with the biaxial device itself and includes documenting the technical challenges with the apparatus. Also, describing the challenges related to biaxial testing with the soil.

The test results can be compared to PLAXIS analysis. The results obtained by numerical simulation in PLAXIS are compared to the results of the biaxial apparatus. The next research question focusses on describing to what extent the results, with the biaxial test, can be explained. The results should be verifiable. However, by numerical simulation in PLAXIS, undesired phenomena can be thoroughly understood. This includes uncertain drainage conditions and unreliable soil parameters applicable to the biaxial laboratory tests. Describing uncertainty of these phenomena in the numerical analysis will explain the test results obtained and give an insight on: *What is the validity of the biaxial laboratory test results.*

The last research question focuses on the third challenge, loading the soil in the apparatus towards failure. This was the initial problem for this thesis: to compare results with the biaxial device to results with other, conventional, tests done with the same soil. If not possible, there lies a challenge in describing the requirements to be able to meet this challenge. This gives the following question and related sub question: *How is the failure criterion obtained with the biaxial apparatus related to the failure criterion from conventional tests? And if not, what should be tackled in future studies to reach this goal?*

### 1.4. Methodology

The first step is to get results with the biaxial apparatus as the device has not been used for two decades and needs to be refurbished. This includes technical procedures such as re-installment and calibration of the sensors, placement of new motors, creating a new input panel. Hereafter, test drives are made with test clay, artificial clay available for research, to get familiar with the working of the apparatus with soils. Performing tests with clay will reveal insights concerning safety, output accuracy, stress limitations, stability of the device and procedures for system control.

The second step is to do biaxial tests with organic clay. Tests to be performed in the laboratory are pre-analysed using PLAXIS. The organic clay is then loaded, resulting in stress measurements. After processing these stress measurements, the output found via the laboratory is compared to the numerical analysis. This will give insight on the



verifiability of the laboratory results. If required, the test procedure is altered. This includes changes in stress measurement, test set-up and applied displacement and displacement rate.

Tests are reproduced to prove verifiability of the test procedure, or to prove the limitations in the test procedure. Following these insights conclusions are drawn from these tests. Recommendations are made for future studies.

## 2. Biaxial apparatus

The plane strain biaxial apparatus used in this research work is introduced. The apparatus meets plane strain conditions. In the first paragraph these conditions and its applicability are discussed. Hereafter, plane strain biaxial devices found in literature are shown. Research on these devices has relevance to the biaxial apparatus introduced by Allersma (1993), which is described extensively. Improvements are made on this apparatus, which are presented in the latter paragraphs.

### 2.1. Plane strain conditions

Stress is an externally applied load that develops a force per unit area. Stress components act normal and parallel upon a surface. The stresses are given by the symbol  $\sigma$  with the first subscript giving the plane on which the stress acts and the second subscript the direction of stress. The stress vectors acting on a material body are shown below.

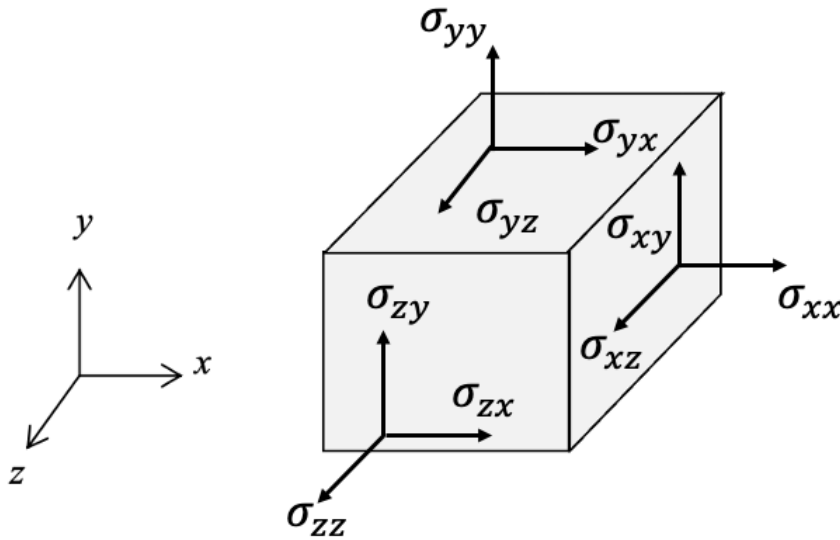


Figure 1: Stress vectors acting on a material body.

The general three-dimensional stress matrix acting on a material body is given in Formula 1. Stresses which act tangentially to the surface are called shear stresses, stresses acting normal to the surface are normal stresses.

$$\begin{bmatrix} \sigma_{xx} & \sigma_{xy} & \sigma_{xz} \\ \sigma_{yx} & \sigma_{yy} & \sigma_{yz} \\ \sigma_{zx} & \sigma_{zy} & \sigma_{zz} \end{bmatrix} \quad (1)$$

For a soil body the stress is differentiated by stresses in the particles, denoted by the effective stress,  $\sigma'$  and by a pore pressure in the water,  $p$ . These two are related to the stress,  $\sigma$  according to  $\sigma = \sigma' - p$ . The stress,  $\sigma$ , is referred to as total stress.

The pore pressure does not contribute to the transmission of shear stresses and only applies to the normal stresses. This gives the following relations for the normal stresses. The total stress denoted without accent and the effective stresses denoted with accent.

$$\sigma_{xx} = \sigma'_{xx} + p \quad (2)$$

$$\sigma_{yy} = \sigma'_{yy} + p \quad (3)$$

$$\sigma_{zz} = \sigma'_{zz} + p \quad (4)$$

Normal stresses acting on a boundary plane of zero shear stress are referred to as principal stresses. These principal stresses can also be given in three directions by subscripts 1, 2 and 3.  $\sigma_1$ ,  $\sigma_2$  and  $\sigma_3$  giving the maximum, intermediate and minimum principal stress, respectively. The allocation of these principal stresses is independent of a defined coordinate axes in x- y- and z-direction. They depend on the sequence of magnitude with  $\sigma_1 = \sigma_2 = \sigma_3$ ,  $\sigma_1 = \sigma_2$ , or  $\sigma_2 = \sigma_3$ , else,  $\sigma_1 > \sigma_2 > \sigma_3$ .

Due to these stresses a material changes its size and/or shape and deforms. The term describing this concept is called strain.  $\epsilon$ , being the strain, with the first subscript giving the plane on which the strain acts and the second subscript the direction of strain. The strain vectors acting on a material body are shown in Figure 2.

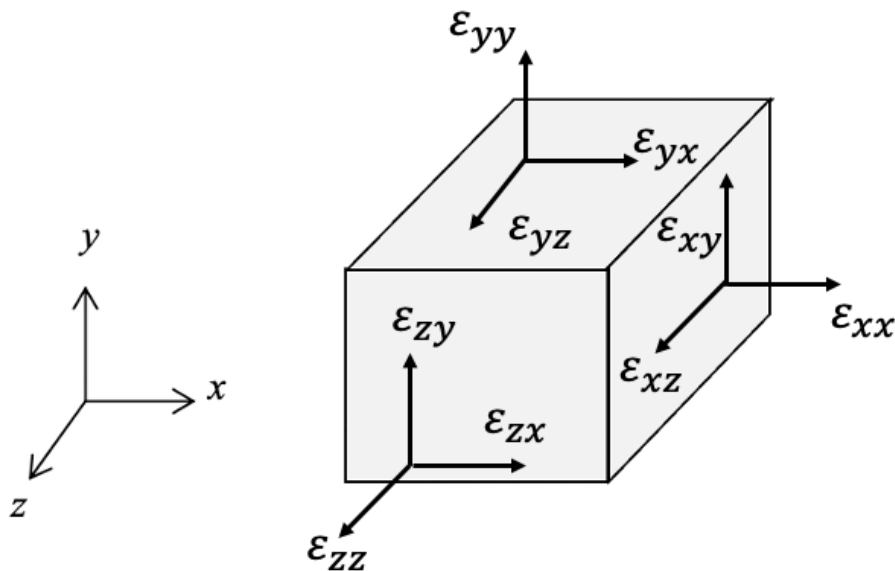


Figure 2: Strain vectors acting on a material body.

The general three-dimensional strain matrix acting on a material body is given in Formula 5.

$$\begin{bmatrix} \epsilon_{xx} & \epsilon_{xy} & \epsilon_{xz} \\ \epsilon_{yx} & \epsilon_{yy} & \epsilon_{yz} \\ \epsilon_{zx} & \epsilon_{zy} & \epsilon_{zz} \end{bmatrix} \quad (5)$$

A state of plane strain is such that non-zero strain components act in one plane only (Kelly, 2013). The axes are chosen such that this x – y plane is the plane with non-zero strains. The strain in z-direction equals zero, and the following holds:  $\epsilon_{zx} = \epsilon_{xz} =$

$\varepsilon_{yz} = \varepsilon_{zy} = \varepsilon_{zz} = 0$ . A representative three-dimensional material body for this situation is shown in Figure 3. It is constrained by rigid walls which prevent normal strain in direction of z,  $\varepsilon_{zz} = 0$ .

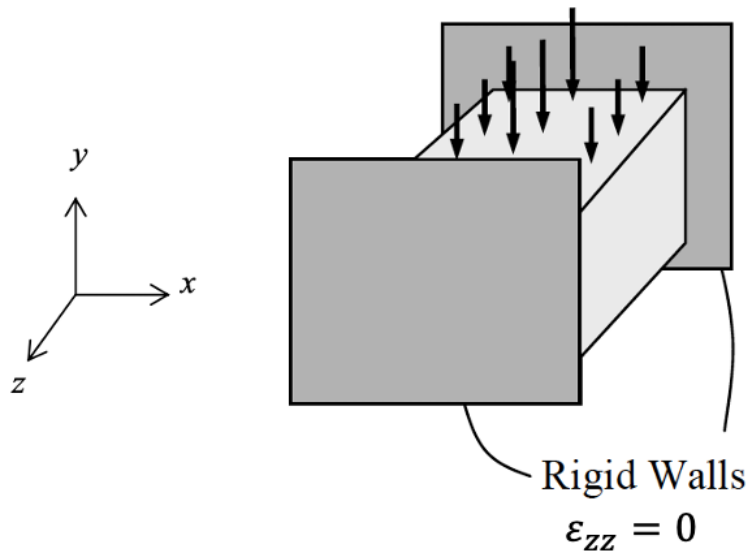


Figure 3: Block of material section constrained by rigid walls (adjusted from Kelly, 2013).

This reduces the three-dimensional matrix above to the two-dimensional matrix below for the state of plane strain.

$$\begin{bmatrix} \varepsilon_{xx} & \varepsilon_{xy} \\ \varepsilon_{yx} & \varepsilon_{yy} \end{bmatrix} \quad (6)$$

In addition, if the loading is the same acting on all cross sections parallel to the y-z plane (purple load vectors with triangle annotation, Figure 4) or cross sections parallel to the x-z plane (green load vector, Figure 4), then  $\varepsilon_{zx} = \varepsilon_{xz} = \varepsilon_{yz} = \varepsilon_{zy} = 0$  (Kelly, 2013). These stresses shown are normal to the surface. Parallel to the y-z plane the normal stress is given by  $\sigma_{xx}$ . Parallel to the x-z plane the normal stress is given by  $\sigma_{yy}$ . Although normal strain  $\varepsilon_{zz} = 0$ , the normal stress acting in z-direction is not restricted and  $\sigma_{zz} \neq 0$ .

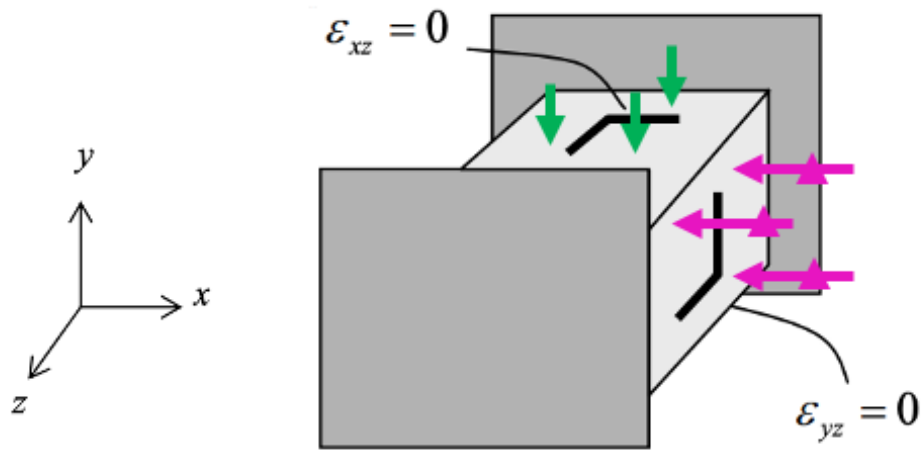


Figure 4: Block of material section with equal loading in either direction of  $x$  or  $y$  (adjusted from Kelly, 2013).

This state of plane strain often coincides with the state of very thick sections. The constructions found in reality, can be simplified to match the state of plane strain. To do this in design calculations, a characteristic cross section is taken representing a relevant material body. In Figure 5 a characteristic cross section of a dike section is shown. For the design of this dike section an infinitely thick cross section in the direction of its length is assumed. Strain is constrained in direction  $z$ ,  $\epsilon_{zz} = 0$ . A dike section is then in state of plane strain.

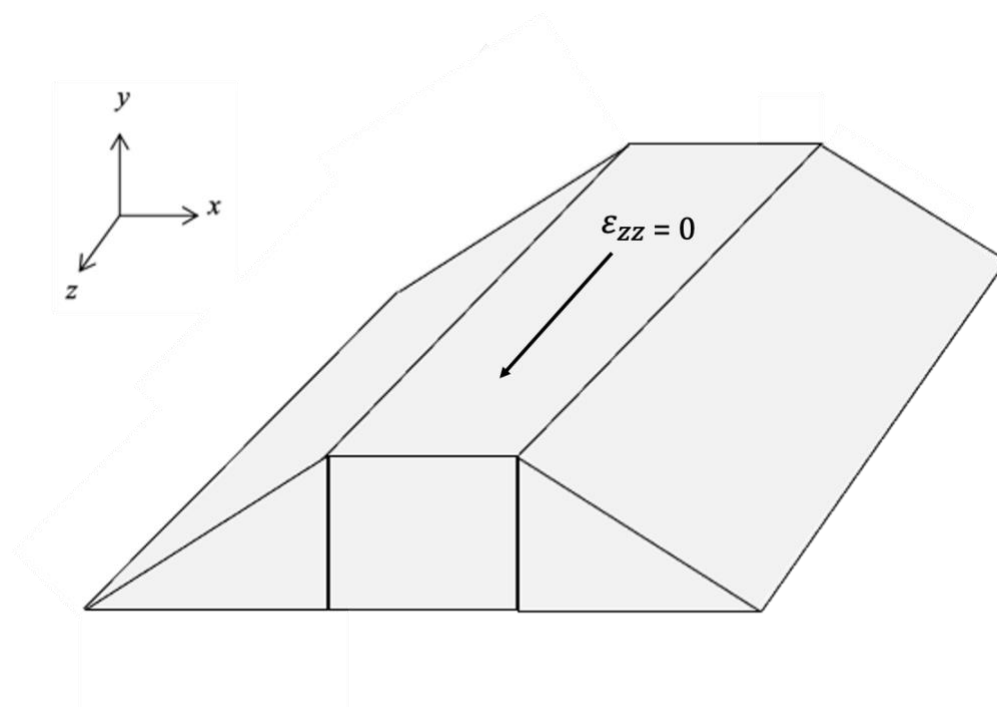


Figure 5: Sketch of cross section dike with plane strain condition.

## 2.2. Biaxial devices

In theory, biaxial devices allow for direct testing of soils under plane strain conditions. Various engineers have attempted to test soil in plane strain condition using different apparatuses. The essential differences between these devices are the shape of the specimen and the method of preventing deformation in the zero-strain direction (Ramamurthy et al., 1989). The specimens can be of prismatic or cuboidal shape. The plane strain condition is usually managed with rigidly connected solid plates.

In the past decades researchers focused their studies on the strength and deformation characteristics of granular materials. For granular material the failure patterns are different from failure patterns observed in a conventional triaxial test. This facilitates a more accurate assessment of shear banding phenomena and stress-strain-strength parameters under these conditions (Cruz, et al., 2012).

The behaviour of clay has been studied less extensively. Allersma (1993) designed a biaxial plain-strain apparatus at the Technical University Delft. It is used to investigate long term creep behaviour on soft clay (Bizzarri et al., 1998). This inspired further investigation on this matter in the early 2000's (Bizzarri, 2002; Cheng, 2004). The apparatus by Allersma (1993) is used for this thesis and will be described extensively in the next paragraph.

Despite the potential of a biaxial plane strain apparatus there are some recurring challenges found for the evaluated devices. Tailor made accessories, membranes and molds need to be designed and difficulties arise with the preparation of a prismatic soil specimen. Techniques to reduce the boundary constraints were difficult to adopt.

Wood (1958) was one of the first investigators to use rectangular shaped specimen along with a rigid system to impose the plane strain condition. In a later stage Hambly et al., (1969) designed a new biaxial plane-strain apparatus seen in the picture below. It can apply large strain on rectangular prismatic samples, confined between four movable rigid platens, marked by A, B, C and D in the picture. Two fixed rigid glass plates confine the sample vertically. Strains are recorded by X-ray methods.

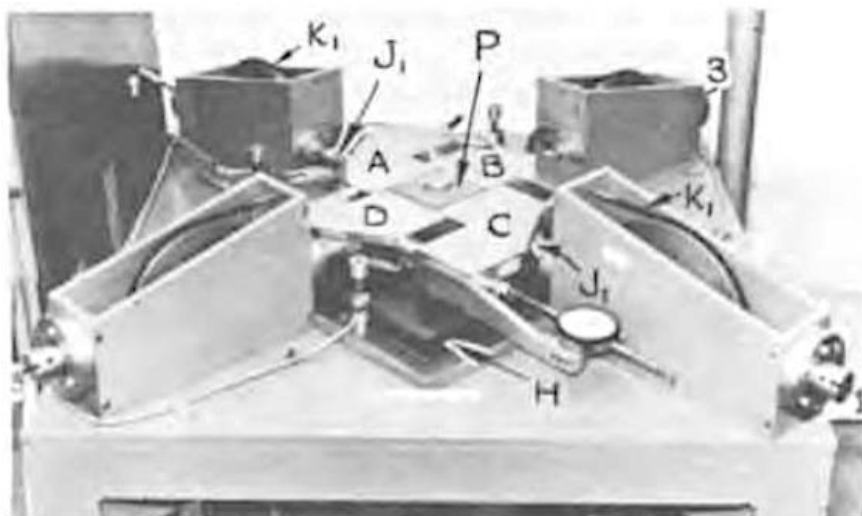


Figure 6: Picture of biaxial apparatus by Hambly et al. (1969).

A soil sample is enclosed by a latex membrane, perforated by discs allowing connection to drainage tubes. A clay sample was sheared to failure. These results were presented in the form of horizontal stress measurements. The stress for the zero-strain plane was not measured.

Topolnicki (1990) investigated further on the principle presented by Hambly et al., (1969). A cuboidal sample is sealed by a rubber membrane and bounded by two vertical plates 50 mm apart. The vertical faces of the sample are in contact with smooth metal plates. In horizontal direction the platens are moveable in both directions. The sample is fixed in vertical direction by a sealing disc, not shown in the image. Displacement is recorded with four displacement transducers mounted on the gear boxes.

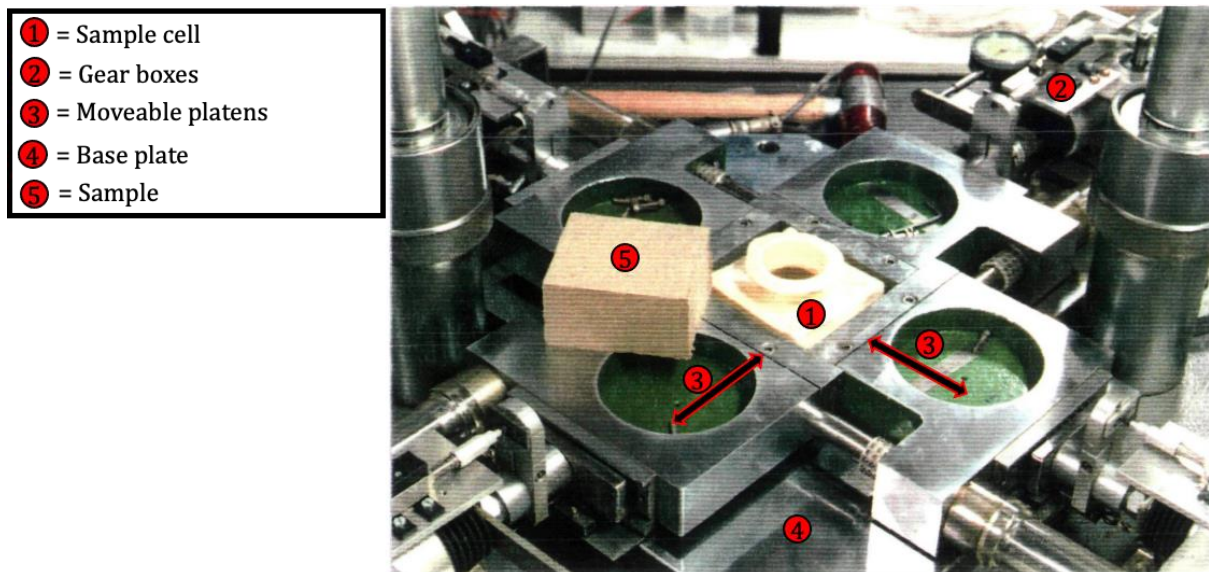


Figure 7: Foto with annotations of biaxial apparatus by Topolnicki (1990).

The undrained stress strain behaviour of saturated remoulded clay is examined using this apparatus. The excess pore pressure is measured using a hypodermic needle placed into the bottom of the sample.

The observations included the stress response dependency on the stress level and the observation of stress paths for continued straining after reaching the failure envelope. A downside of the apparatus by Topolnicki (1990) is the completely sealed cell, restricting observation of shear band formation.

The work by Topolnicki (1990) inspired Allersma (1993) to design a new biaxial device with a few improvements to its predecessors. Potential downfalls of these predecessors, as mentioned by Allersma (1993), are the synchronisation realised by complex gearing systems and measurement of the displacement by transducers. Another disadvantage is that the boundary stresses in previous designs involve significant friction components.

Fauziaz et al., (2008) investigate the stress-strain behaviour of unsaturated clay under plane strain conditions. A rectangular sample is used and restrained by two perspex plates restraining out-of plane strain as seen in the picture below. A submersible load cell applies axial load on top of the specimen. Three pore pressure transducers are



installed into the bottom plate. These transducers measure the cell pressure, back pressure and pore pressure.



Figure 8: Foto of plane strain apparatus by Fauziyaz et al. (2008).

Another notable test design is that of Vardoulakis (1977), found to be the inspirational design for other plane-strain devices, is shown in Figure 9. A tabular specimen is used which is restricted to deform in the longitudinal direction. Lateral displacements are measured in two opposite points of the face of the specimen. The base plate, marked with a 2, is placed on a roller bearing, marked with a 4. This enables movement in the horizontal direction. It gives the sample freedom to fail along a plane shear band, dividing the soil into two rigid bodies.

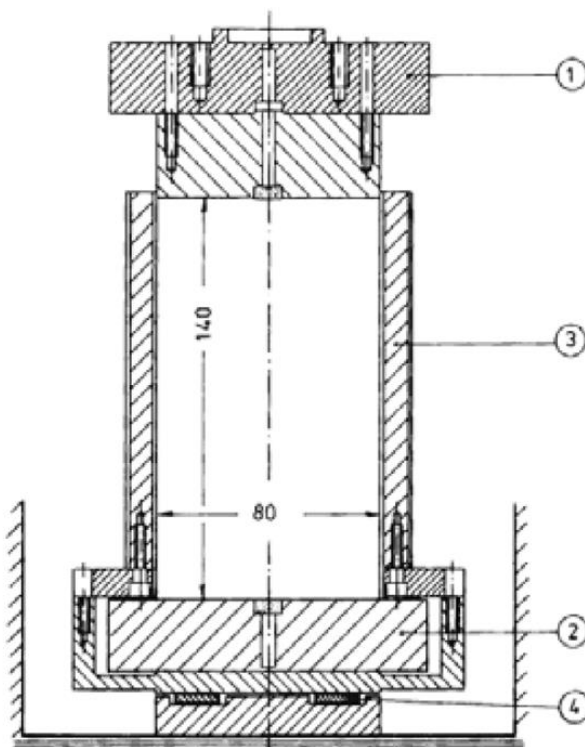


Figure 9: Schematic diagram of plane strain apparatus by Vardoulakis et al. (1981).



Han et al., (1991) studied the behaviour of fine-grained sand in plane-strain conditions using this apparatus. Plane strain compression tests were carried out on a fine sand. Bifurcation phenomena, such as deformation instability and strain localisation, were studied.

Wanatowski et al., (2006) describe a new plane-strain apparatus enabling various stress and strain paths to be controlled under plane-strain conditions. A prismatic granular soil specimen is placed in the centre of the apparatus shown below. An axial load is applied in vertical direction via the top cap. The lateral stress was measured by four pressure transducers, embedded in the two fixed lateral loading platens marked in the picture. The strain in the out-of-figure direction, is measured using submersible linear variable differential transformers, LVDT's.

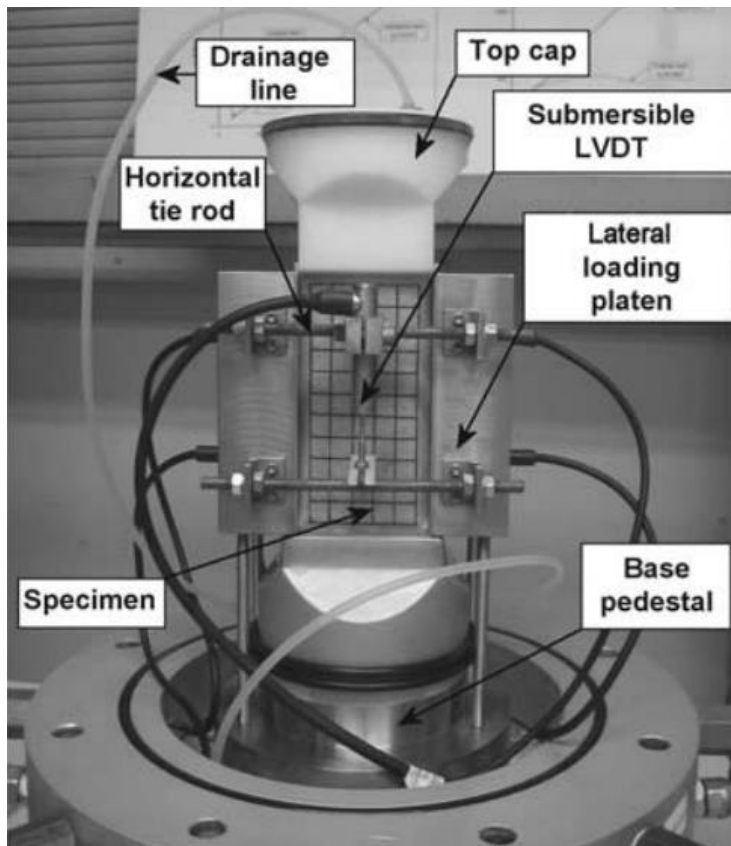


Figure 10: Photograph of plane strain apparatus by Wanatowski et al. (2006).

Drained plane-strain compression tests are carried out on sand obtaining failure states. This is accompanied by the process of shear band formation, monitored by photography. The start of this shear band formation can be detected by the divergence in the four lateral stress measurements. Found is that the critical state line for plane-strain conditions is different from that under axisymmetric conditions.

### 2.3. Biaxial apparatus by Allersma (1993)

The apparatus designed by Allersma (1993) is shown in Figure 11. The axes with respect to the apparatus are depicted and used as reference in this report. In the centre of the image, the biaxial cell is highlighted in black. A soil body can be placed in this biaxial cell with a surface ranging from  $2,500 \text{ mm}^2$  to  $22,500 \text{ mm}^2$  and a fixed height of  $50 \text{ mm}$ .

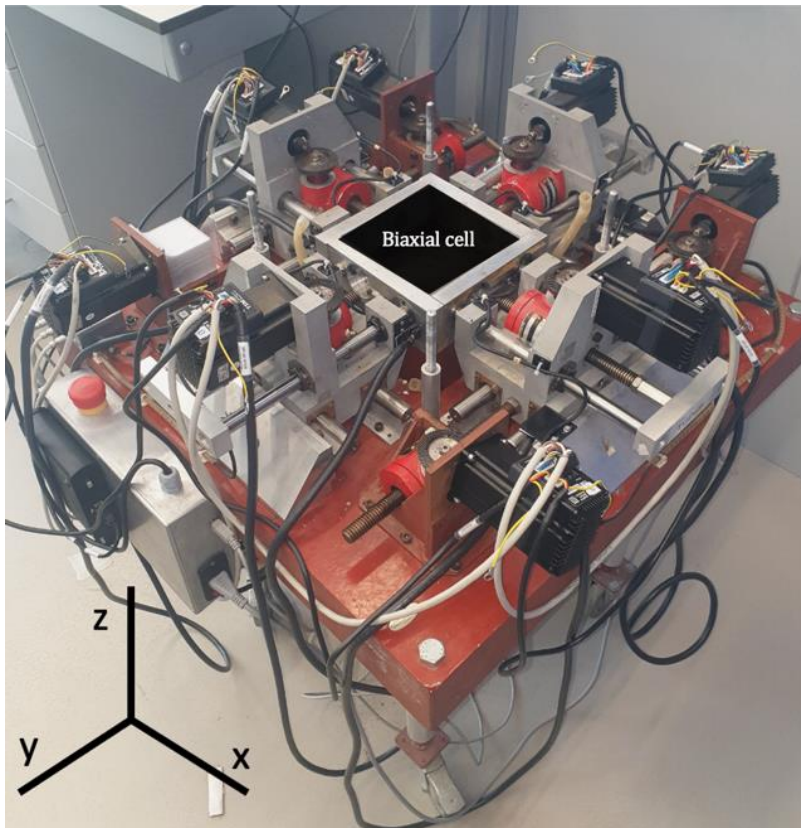


Figure 11: Picture of biaxial apparatus with axes and biaxial cell marked.

In theory, a test performed with the biaxial apparatus by Allersma (1993) will occur under plane strain conditions. Figure 12 gives a sketch of the top view of the biaxial cell with corresponding strains indicated. Normal strains are imposed by the biaxial apparatus in direction of  $x$  and  $y$  with shear strains equal to zero.

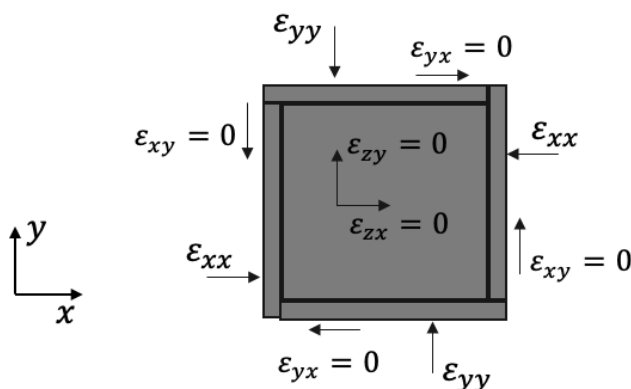


Figure 12: Sketch of top view biaxial cell with indication of strains.

A side view, in the direction of  $y$ , shows the normal strain in  $z$  direction to be zero. The material body is confined by two boundaries represented by two dashed red lines to effectuate this zero-strain condition. The state of plane strain previously introduced, applies to the state of the material body used in the biaxial cell.

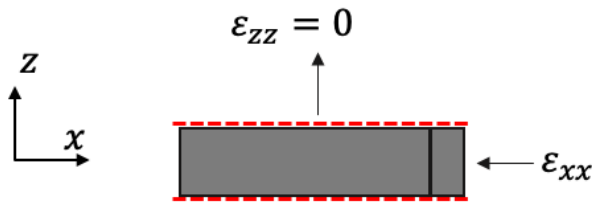


Figure 13: Sketch of side view biaxial cell with indication of strains.

The normal strain applied by the apparatus lead to normal stresses  $\sigma_{xx}$ ,  $\sigma_{yy}$  and  $\sigma_{zz} \neq 0$  acting on the boundary planes of the material body. With the shear strains on these planes equal to zero, the shear stresses  $\sigma_{xy}$ ,  $\sigma_{xz}$ ,  $\sigma_{yx}$ ,  $\sigma_{yz}$ ,  $\sigma_{zx}$  and  $\sigma_{zy} = 0$ .

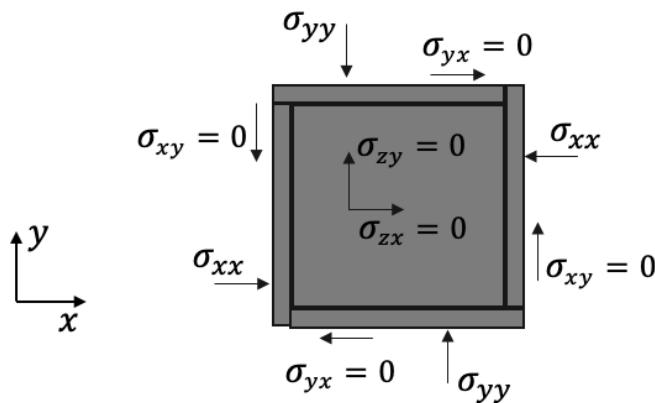


Figure 14: Sketch of top view biaxial cell with indication of stresses.

A side view of biaxial cell with the stresses acting on the soil is shown below.

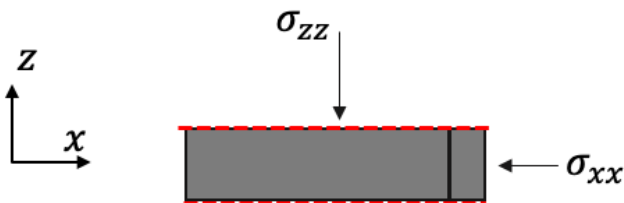


Figure 15: Sketch of side view of biaxial cell with indication of stresses.

For the biaxial test, normal stresses are applied perpendicular to the boundary with the shear stresses equal to zero. As a result, the measured stresses in the laboratory and in the numerical analysis are equal to the principal stresses.

Chapters 4 and 5, presenting the PLAXIS analysis and laboratory results, use the stress annotation shown in Formula 1 with normal stresses in the  $x$ -,  $y$ - and  $z$ -direction as  $\sigma_{xx}$ ,  $\sigma_{yy}$ ,  $\sigma_{zz}$ , respectively. These stress subscripts correspond to the axes set for the laboratory test set up introduced in this paragraph. The theory in Chapters 6 and 7 use principal stress annotation to define the stresses.

The soil sample is placed in the biaxial cell which is confined by four vertical metal plates and two horizontal glass plates. The horizontal glass makes it possible to observe deformations. Displacements are applied to the boundary conditions in both horizontal directions, which are computer controlled. The computer activates eight individual step motors by sending a pulse. Each pulse coincides with a step of  $1/20,000$  mm displacement. The motor on its turn activates two activators which displace the four plates. The four plates can be displaced individually.

The plates can shift in two perpendicular directions. Namely, corresponding with compression, movement towards the opposite plate or extension, movement apart from the opposite plate. A top view of the biaxial apparatus is shown in Figure 16, with the direction of compressional movement marked by blue arrows. The plates move in lateral direction to avoid collision between the plates, this displacement is indicated with the red arrows in Figure 16.

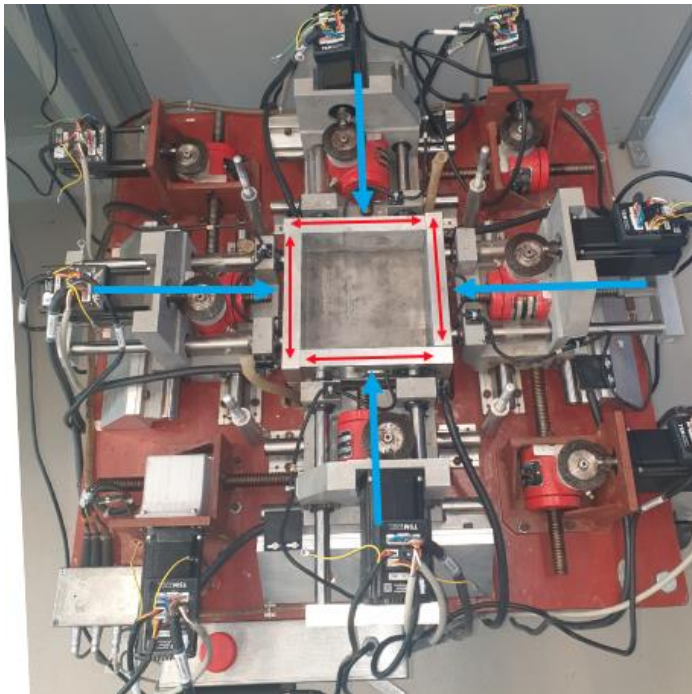


Figure 16: Top view of biaxial apparatus.

The opposing plates can be mechanically linked, leading to a synchronized displacement. This gives two advantages. First, the imposed loading on the sample will be symmetrical. Thus, the expected behaviour of a homogeneous soil on one side of the sample is expected to be analogous the other side of the sample ((Topolnicki, 1990). Secondly, another advantage of mechanically linked plates is the convenience of measuring the pore pressure (Topolnicki, 1990). The centre of the sample does not move, making it an appropriate position to place a stress or pore pressure transducer.

The accuracy in control operations, such as the ceasing or rewinding of the moving loading platens, is well below  $0.01$  mm, but it is not certain whether this is enough for relaxation or constant volume shearing tests, which could cause a relatively quick and significant change of stress (Cheng, 2004).

## 2.4. Test procedure by Allersma (1993)

The platens of the apparatus by Allersma (1993) can be put into motion and the movement in the x- and y-direction is recorded. The total stress is measured by four pressure sensors in x- and y-direction. The sensors are installed in the metal plates and make direct contact onto the surface of the clay sample. This avoids the effect of frictional components between the sample and the plate. Allersma (1993), did not implement a sensor in z-direction but mentioned the possibility to do so.

The pore pressure is measured at the centre of the sample. Allersma (1993) uses a pore pressure needle with a transducer. The whole is placed in a 2.5 cm long tube and inserted into the sample. A sketch of the top view and side view of the biaxial cell are shown below, indicating the position of the total stress sensors and the pore pressure needle. In the sketch of the top view a red dotted line indicates the cross section taken for the side view.

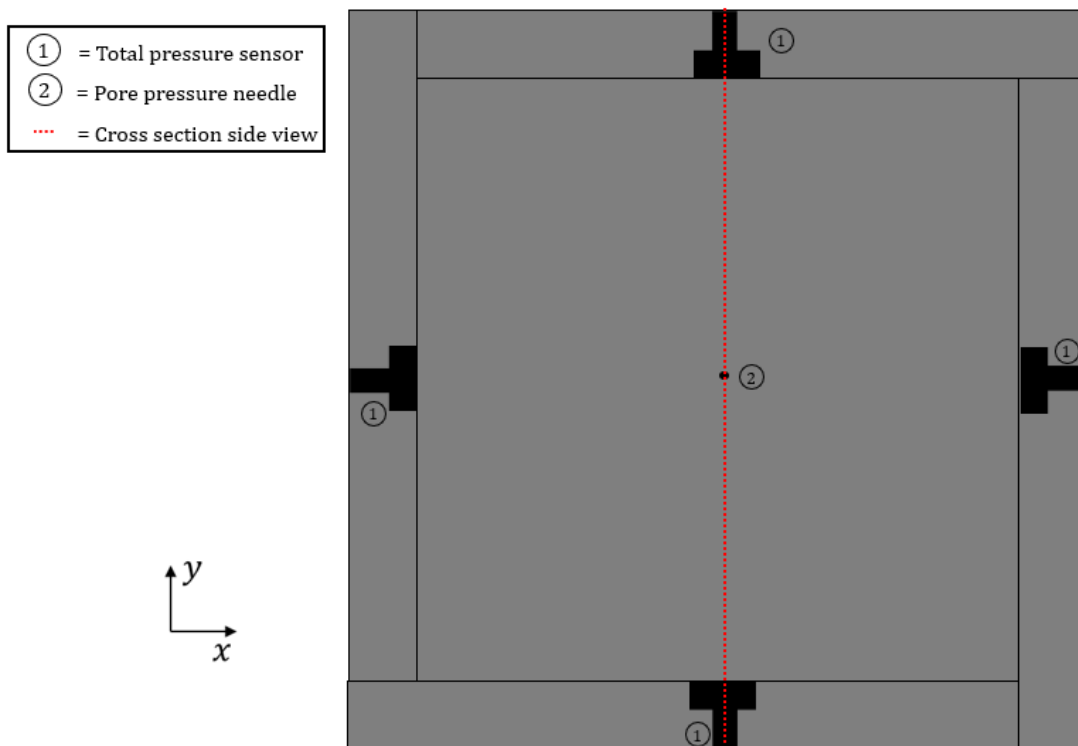


Figure 17: Sketch of top view biaxial apparatus by Allersma (1993).



Figure 18: Sketch of side view biaxial apparatus by Allersma (1993).

Allersma (1993) describes that the device can be driven in either displacement or stress control mode. A constant displacement can be managed to maintain displacement

control mode giving the stress-time relationship. A constant stress can be managed to maintain stress control mode giving the strain-time relationship.

In test procedures presented by Bizzarri et al., (1995, 1998) a combination of both modes is used. The desired load is reached by applying constant strain in the x- and y-direction. Once this load is reached the two parallel plates in the x-direction continue to displace and maintain the desired constant stress. The plates in y- and z- direction are fixed and the stress in x- and y-direction is measured.

There are various factors which could influence the consistency of the biaxial test. Bizzarri et al., (1995) describe that relatively large differences develop between stresses measured on two opposite plates of the biaxial device. One-dimensional compression tests were performed to investigate the behaviour of the sample during the test procedure. A slurry of clay and de-aired water was poured in the apparatus. To avoid friction, the plates were covered with vaseline. Later, it was covered with thin plastic. An additional advantage being the prevention of water and clay entering the gaps between the metal plates.

The slurry was loaded in x- and y-direction until a desired total stress is reached in both directions. This is marked with a red cross in the plot of Figure 19. Hereafter, solely the two active plates compressing in the y-direction continue to move. One of the two load cells was used to control the stress. This load cell is indicated by  $p_y(2)$ . The opposite plate  $p_y(1)$  moves independently from the stress measured on the opposite plate. Stress differences develop between the opposite plate. Bizzari et al., (1995) find that this is independent of the applied total load and that in the worst case a difference of 5% in stress is found. The passive plates in x-direction, indicated with  $p_x(1)$  and  $p_x(2)$  in Figure 19, show little difference.

It is concluded that movement of the plates causes inhomogeneous consolidation. As a result, water flows asymmetrically out of the sample. The plastic sheet is found to strengthen this inhomogeneous consolidation. Use of vaseline gave more symmetric results. Bizzarri et al., (1995) conclude that they will use preconsolidated samples and perform experiments without a filter sheet in the future.



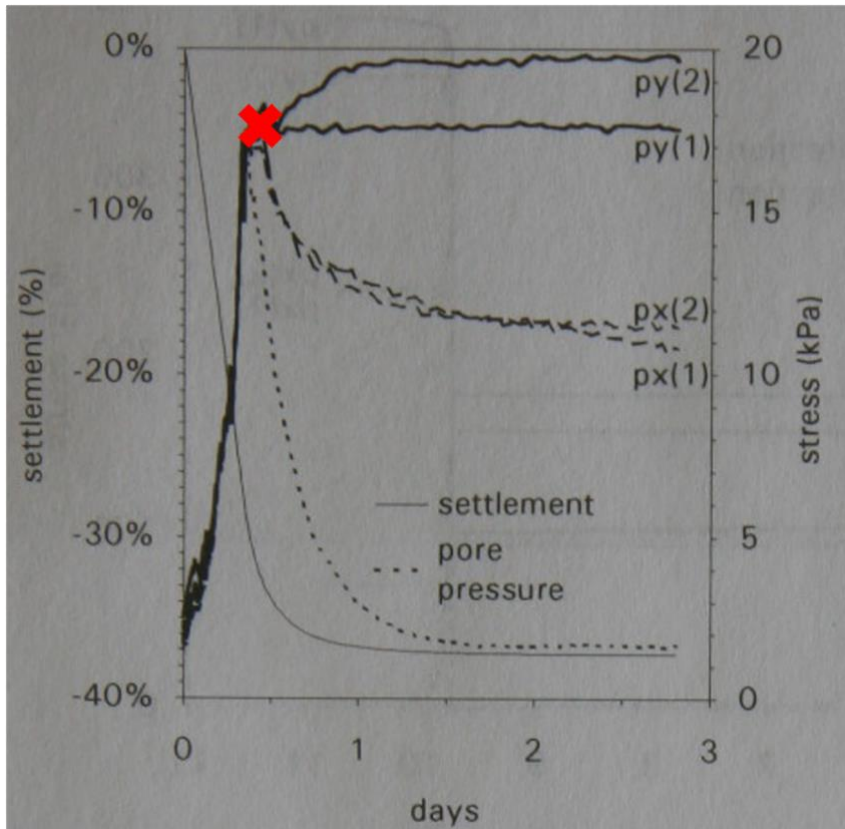


Figure 19: Time, stress and settlement diagram for one-dimensional compression test on clay with biaxial apparatus. A thin plastic sheet was used to avoid friction for this test. (Bizzarri et al., 1995).

Cheng (2004) investigated the stress-strain relationship and rate-dependency of failure patterns with OVP Clay using the biaxial device of Allersma (1993). The clay is found to be more instable when a slower displacement rate is applied. It is mentioned that the desired undrained conditions are difficult to maintain in practice.

The drainage conditions are unidentifiable, and the pore pressures give scattered results due leakage between walls and lack of saturation. Cheng (2004) encloses the samples in liquid latex to maintain undrained conditions for slow undrained shear tests. Suggested is to improve the knowledge of local drainage in the sample to consistently determine the strength of the clay.

## 2.5. Improvements of biaxial device

In the present study it is investigated how to get results with the biaxial device presented by Allersma (1993). The biaxial apparatus has not been used for 18 years and documentation on the specifications of the apparatus are limited. The apparatus at the beginning of this study is shown in the figure below.

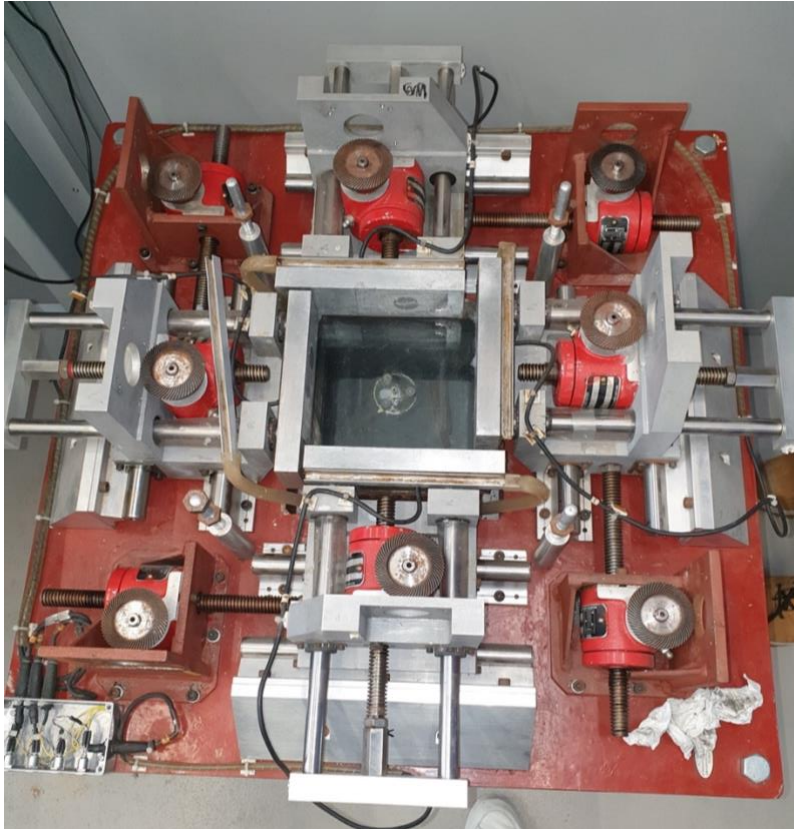


Figure 20: Top view picture of state of biaxial apparatus not used for 18 years.

No program was available to control the apparatus and the technical components were lacking (motors, wiring). Several steps regarding installation, control, safety and technical specifications are required to redevelop the apparatus and are described in the coming paragraph.

### 2.5.1. Technical specifications and safety

Eight new step motors are placed to drive the boundary plates. TSM23S-3RG – NEMA 23 Integrated StepSERVO™ motors are used manufactured by Applied Motion Products. It has a built-in encoder which makes 20,000 counts per revolution making it possible to attain highly accurate displacement rate and position control.

Four *BED A* small-sized soil pressure transducer developed by Kyowa Electronic Instruments are used to measure the total stress. The pressure sensors were placed by Allersma (1993) and are maintained as the metal side platens are cut-out to exactly suit these sensors.



The sensors are developed to measure the soil pressure distribution in short-term or model experiments. This enables the transducer to measure pressure up to a capacity of 1 MPa. The accuracy is given by the percentage of rated output, RO. It expresses the maximum difference in output when the same load is measured. For the total stress sensors this is set within  $\pm 1\%$  of the RO.

The sensors are calibrated by applying controlled air pressure to the sensors and verifying the output pressure given by the sensor. This gives the gain and offset required to link the applied pressure to the output pressure. The sensors are assessed for reliability and instable sensors are replaced by spare sensors of the same type.

Precautions are added to enhance the safety of the device. An emergency button is placed to the side of the apparatus. By pressing it, the entire device is switched off and displacements are stopped. Recording of the stresses is maintained. Plastic casings are placed around the step motors to avoid accidents due to contact.

A reference state of the plates is referred to as the *home position* which corresponds to the largest cell volume of 22,500 mm<sup>2</sup>. During the testing phase a plastic tube blocked the home position switch sensor. This made the plates displace beyond the home position causing damage to the plates. Two measures were taken to prevent this in the future. The tubing was shortened as much as possible. Also, a more robust switch sensor was installed.

The horizontal glass plate can withstand a maximum pressure of approximately 1000 kPa. This value was found unintentionally after the pressure increased upon breaking of the glass. To prevent recurrence of this event a maximum pressure of 600 kPa was set as standard. The maximum pressure can manually be set to values lower than the standard.

The specifications are annotated in the picture below.

- ① = Switch sensor
- ② = Robust wiring
- ③ = Plastic casing
- ④ = Emergency button
- ⑤ = Data acquisition device
- ⑥ = Step motor

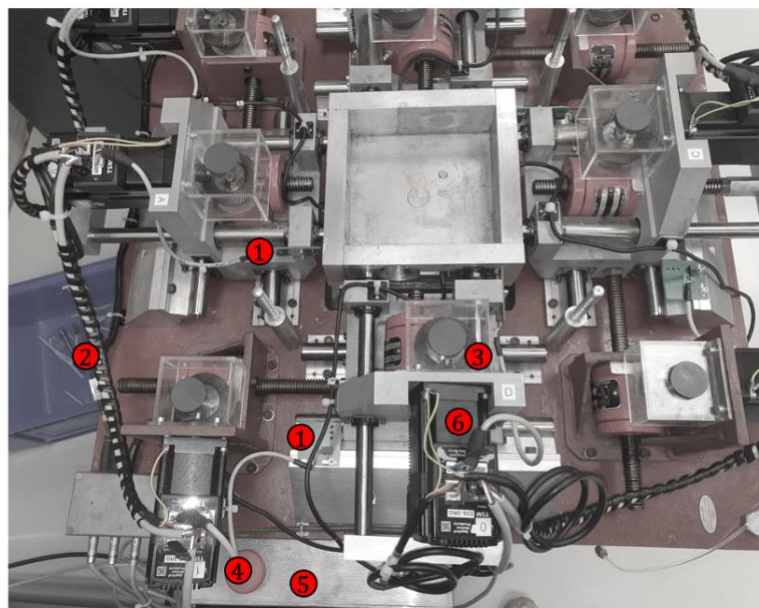


Figure 21: Biaxial apparatus with specifications annotated.

## 2.5.2 Input panel and apparatus control

The input panel to control the apparatus is not documented by Allersma (1993). The system-design platform LabVIEW is used to visually program the displacement management. The result is an input panel giving a graphical approach to control the motors. The interface is shown and explained in Appendix A.6.

To acquire the signal from the sensors, two USB-2404-UI Measurement Computing™ data acquisition devices are installed. These devices have an accuracy of  $\pm 0.3\%$  of their acquired reading. Each device has four channels to measure signals from sensors. It translates the signal to the LabVIEW program, giving the required output.

The input can set displacements for each individual motor and associated plate. This is done by setting the desired displacement in  $mm$  and the displacement rate in  $\frac{mm}{s}$ . The reference state of the *home position* corresponds to the largest cell volume of  $22,500 mm^2$ . Displacement to this reference state is available as input on the panel. A switch sensor is activated once the plate reaches its home position. This application gives the advantage that the plates can be displaced to a known position, despite of being in an unknown configuration. Often, this is the case when the device has been switched off and has lost memory of its position. Further displacement can either be given as an absolute position with respect to the home position or as a relative displacement with respect to the current position. Each plate can be given a displacement individually in either compression or extension.

The panel gives a visual output in the form of a graph of the stress per sensor for time. An example of this graph is shown in Figure 24. In a later stage, a selection tick box is made available, allowing saving these stress values in a text file. The stresses can be recorded for a desired incremental time value. The panel also gives a visual output of the time versus the displacement. The displacement values are also saved in a text file in correspondence with the stress measurements.

The displacement is verified using a KYOTO displacement tool. First, the plates are put into the home position. A set of relative displacements of consecutively  $-0.05 mm$ ,  $-0.07 mm$  and  $-0.1 mm$  are repeatedly applied to the horizontal plate. The measured displacement gradually increases before reaching the intended displacement. The gearbox of the step motor needs to shift into the correct transmission. This is done by displacing the plates into the home position and applying a few displacement increments.

The minimum possible displacement rate is found to be  $0.00021 \frac{mm}{s}$ . The displacement rate can only be set at increments of this minimum displacement rate. Which gives the second slowest displacement rate possible being  $0.00042 \frac{mm}{s}$ . It possible to set displacement rates between two incremental values on the input panel. The panel will then automatically signal the displacement rate of the greatest next increment to the motors.

### 2.5.3. Desired improvements

Allersma (1993) does not report total pressure measurement in z-direction. The horizontal bottom plate encountered at the beginning of this thesis, did not match the description by Allersma (1993), as there was no pore hypodermic needle present. Both these issues are addressed in the present study to measure pore pressure and total stress in z-direction.

Cheng (2004) mentions the difficulty of maintaining the drainage conditions. Alterations to the biaxial device and forthcoming analysis are performed to control and understand these drainage conditions.

### 2.6. Preliminary testing phase

The preliminary tests were aimed to verify the basic applications of the apparatus. In the first stages a plastic mold was made to fit into the biaxial cell and simple tests were performed. Hereafter, a  $10,000 \text{ mm}^2$  test clay sample was placed in the cell. The sample was displaced according to the configuration scheme in Figure 22 at  $0.01 \frac{\text{mm}}{\text{s}}$  taking approximately 5 minutes.

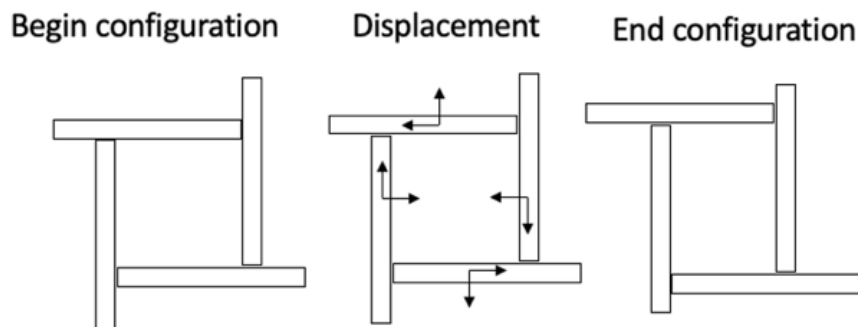


Figure 22: General configuration scheme for preliminary tests.

The deformed clay sample is shown below in Figure 23. At the corners of the clay sample contact is lost with the plates. This is due to friction between the plates and the sample. The friction phenomenon is undesired as it implies nonzero shear strains, not corresponding to plane strain conditions. To prevent friction the plates are greased in with vaseline. This reduced the amount of friction significantly which ensured symmetrical contact made by the sample in future tests.



Figure 23: Deformed sample after applying the configuration of Figure 22.

The output panel for this test is given in Figure 24. During these first preliminary tests transforming the data to a text file was not yet implemented in the input panel. The colour of the lines in the output panel correspond to the colour of the numbered plates in Figure 23. The two sensors corresponding to active plates are shown in green and white and are marked with an elongated dashed arrow. The two sensors corresponding to the passive plates are shown in orange and blue and are marked by the densely dashed arrow. The output corresponding to the active plates show noisy signals. These two sensors are replaced in a later stage.

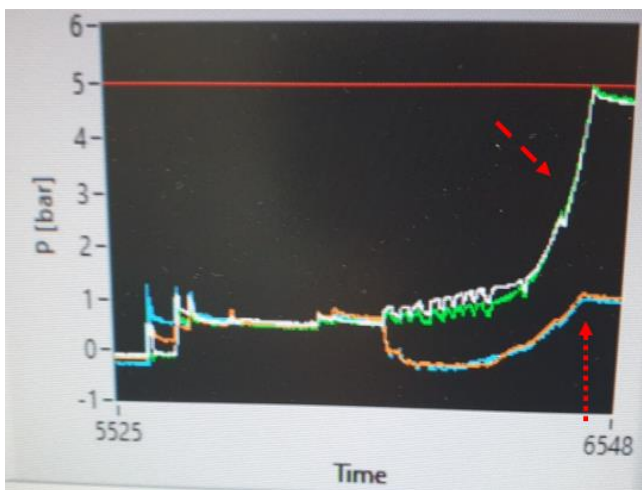
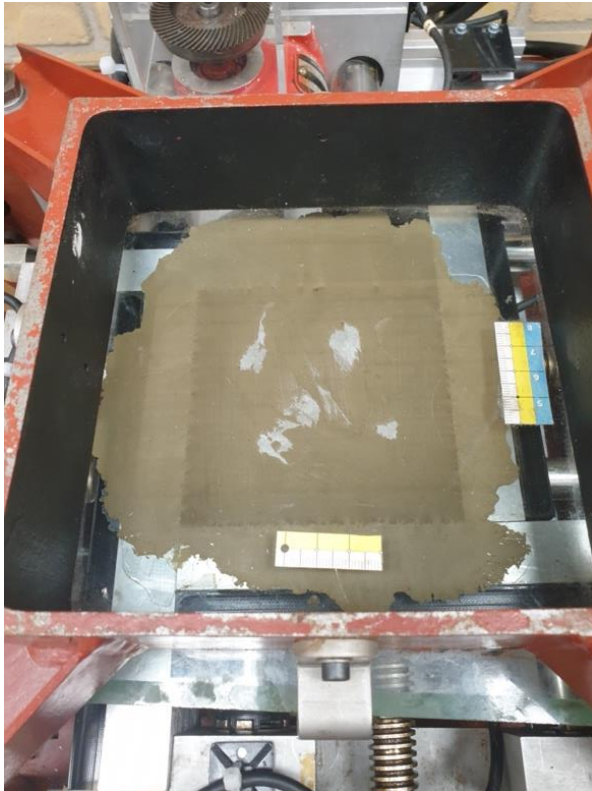


Figure 24: Time [s] versus stress [bar] panel plot of displacement according to Figure 22. Note: During these first preliminary tests transforming the data to a text file was not yet implemented in the input panel.

This output is realistic as the active plates sensors increase in pressure as the passive plates sensors show a decrease before slightly increasing in pressure. The opposite plates are given the same displacement rate and displacement which should give identical pressures. Slight deviations are seen although it should be noted that not full

care was taken for the consistency of this test regarding friction and preparation of the sample. Further tests are carried out to verify the response of the apparatus.

Another challenge occurs when carrying out time consuming tests in the order of hours. The test clay slowly pressed out of the biaxial cell as seen in Figure 25. The bottom plate was tightened up. The downside of this measure being that the vertical plates scoured the bottom plate. By trial and error, a balance in tightness of the bottom plate, yet preventing pressing out of clay, is found.



*Figure 25: Clay pressing out during 4-hour test.*

## 2.7. Adjustments after preliminary tests

After the first improvements, Paragraph 2.5, and preliminary testing phase, Paragraph 2.6, further adjustments were made to the apparatus.

### 2.7.1. Alternation of bottom plate

In this stage the bottom metal plate was changed. A total pressure sensor of the same type is placed in the centre of the plate. A hole was drilled, close to the centre of the bottom plate. This allowed the placement of a 7 mm diameter bolt. A porous stone enclosed by a metal bolt is installed. This porous stone is connected to a water pressure meter. A top view and side view of the biaxial cell, including dimensions, are shown below.

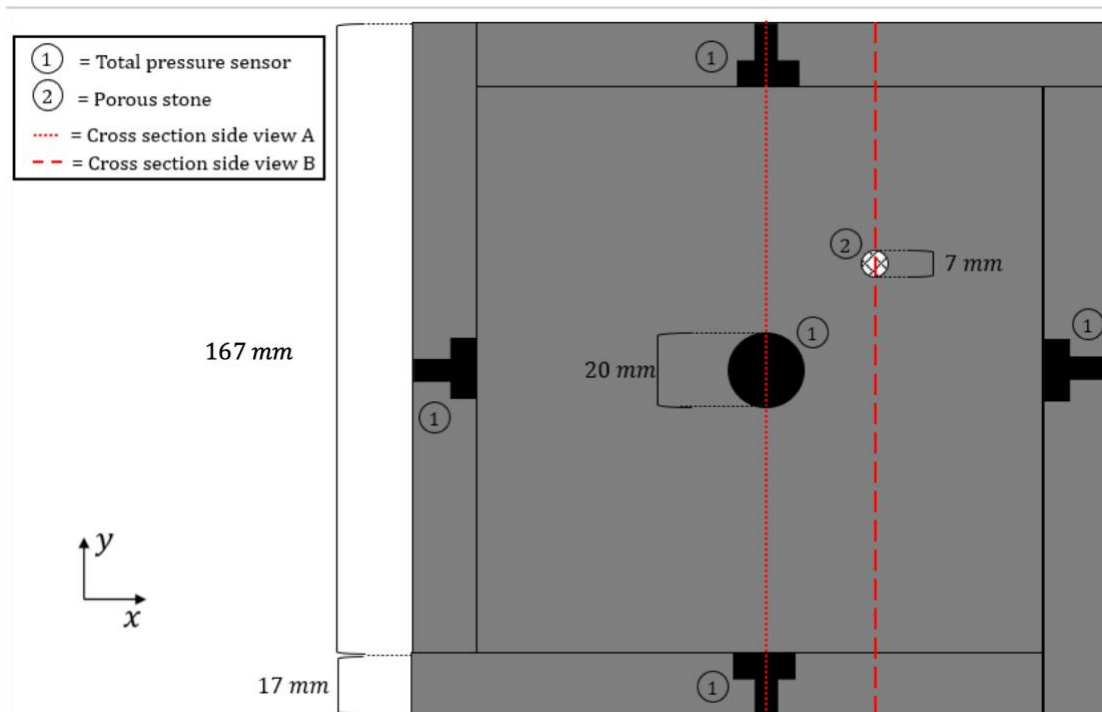


Figure 26: Sketch top view biaxial apparatus.

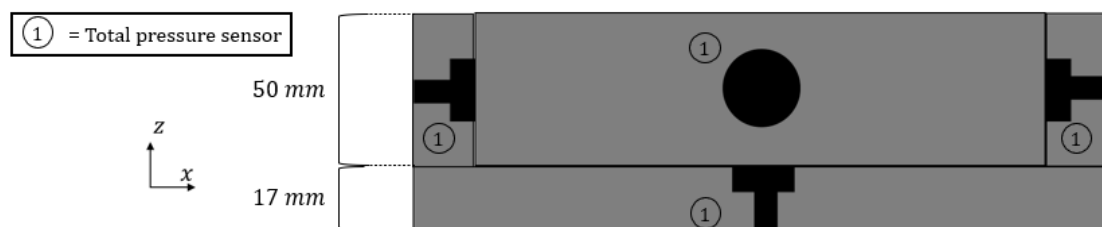


Figure 27: Sketch of side view biaxial apparatus, cross section annotated by 'Cross section side view A' in Figure 26.

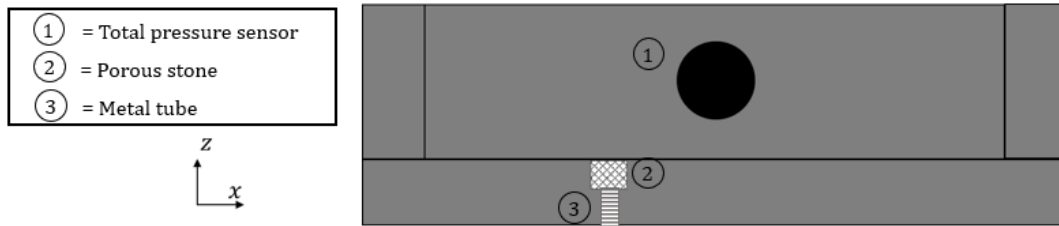


Figure 28: Sketch side view biaxial apparatus, cross section annotated by 'Cross section side view B' in Figure 26.

A first design is made to measure the pore pressure and is described in Appendix A.1. Along with pore pressure measurement, this design also aims to control drainage conditions through the porous stone. To saturate the water system, a water injection needle is used flushing the metal and plastic tubes with water. A sample is placed inside the biaxial cell. Test 1, T1, further described in Paragraph 5.1, gives water pressure measurement close to zero. This does not coincide with the results seen for the numerical analysis presented in Chapter 5.

A theory for the measurement of zero pore pressure is that the porous stone is clogged with clay particles of preceding tests. This blocks the flow of excess pore water. Another restricting factor is the presence of air bubbles in the relatively long system of tubes. To get this system fully saturated with water, a different design is believed to be needed. Further adjustments are made to the water pressure measurement.

T1 intended drained conditions through the porous stone. However, no excess pore water is seen flowing towards the water outlet. The concept of controlling the drainage conditions through the porous stone and the water outlet was rested. In the coming designs measuring pore pressure was prioritized and undrained conditions prevailed through the porous stone.

During performance of the tests water is seen seeping out of the biaxial cell, marked by the dashed box in the picture below. This occurs at the gaps between the plates. These gaps are measured and found to range between 0.05 mm and 0.2 mm.





Figure 29: Seepage of water between the bottom plate and vertical plates during biaxial loading.

These drained conditions at the border of the biaxial cell are uncontrolled. To understand this behaviour during the laboratory tests, this phenomenon is implemented into the numerical analysis, shown in Chapter 4.

### 2.7.2. Adjustment of pore pressure measurement system

During T1 no excess pore pressure is recorded. There are two explanations proposed for this zero recording. A clogged porous stone which restricts pore pressure to flow towards the water pressure transducer and/or an unsaturated tubing system. For an unsaturated system, air bubbles still present in the tubes will compress first. Once they are compressed the excess water pressure will build up due to further loading. This would give a delayed increase in water pressure towards the water pressure transducer.

These two explanations are verified with the set up shown in Figure 30. For this, half a meter of water column was put on top of the porous stone. This gave an increase of 50 kPa as expected.





Figure 30: Verification of excess pore pressure measurement using a water column.

Next, the water measurement system was saturated according to the steps shown in Appendix A.2. Again, half a meter of water column was put on top of the porous stone. This water column gave the corresponding increase of water pressure. From these measurements it is concluded that the pore pressure measurement system itself works. This features a permeable porous stone and a saturated tubing system towards the water pressure transducer.

After this validation three new designs were made to measure the pore pressure during a laboratory test. Both designs entail undrained conditions through the porous stone and are saturated according to the steps of Appendix A.2. These designs are shown in Appendix A.3, Appendix A.4, Appendix A.5.

### 2.7.3. Uncontrolled drained conditions at the biaxial cell boundaries

During performance of the tests water is seen seeping out of the biaxial cell. This occurs at the gaps between the horizontal and vertical plates. These drained conditions at the border of the biaxial cell are uncontrolled, shown in Figure 29. To understand it, this phenomenon is implemented into the numerical analysis introduced in Chapter 4

### 3. Material Description

Tests with the biaxial apparatus will be performed on remoulded Oostvaardersplassen, OVP, clay. This soil is found at the diked marshland of southern Flevoland, central Netherlands. This soil is believed to be a representative of Dutch organic and calciferous clay (Cheng et al., 2003).

#### 3.1. OVP clay in literature

Physical properties of this clay have been tested since the 90's (den Haan, 1995). It is found that the OVP clay has a high effective friction angle (den Haan, 1999). Extensive direct shear, triaxial and  $K_0$ -CRS, constant rate of strain, tests on remoulded samples of OVP clay were performed by Tigchelaar (2001). The experimental evidence on the stress development of the OVP clay with the biaxial device is limited. However, biaxial tests with the same apparatus were performed on the same soil (Bizzarri et al., 1995; Bizzarri et al., 1998). These tests investigate OVP Clay creep behaviour and mention the soil having a low hydraulic conductivity resulting in relative time-consuming tests. Hence, further research of this material is desired using the biaxial apparatus.

The clay shows a variation in properties, possibly related to the fact that natural OVP clay deposition contains an upwards decreasing amount of organic matter. Also, thin layers of silts and fine sand are encountered in the clay deposition (Van Loon et al., 1975). Tigchelaar (2001) mentions that the water content can vary by 25% with a depth difference of 10 cm. Therefore, Tigchelaar (2001) chose to gather a broad set of OVP clay samples from different locations at the Oostvaardersplassen. The average OVP clay material properties found by Tigchelaar (2001) are shown in Table 1.

Table 1: OVP clay material parameters found by Tigchelaar et al. (2001).

Parameters, Tigchelaar et al. (2001)	Value
Liquid limit, $w_l$ [%]	120.0
Plastic limit, $w_p$ [%]	37.0
Saturated weight, $\gamma_{sat}$ [ $\text{kN}/\text{m}^3$ ]	14.0
Organic content [%]	9.5
$\text{CaCO}_3$ content [%]	9.2

Stress development for DSS, direct simple shear, triaxial compression and triaxial extension tests, presented by Zwanenburg et al. (2019), are also done with OVP clay. The characteristics for the remoulded clay used by Zwanenburg et al., (2019) are shown below in Table 2.

Table 2: OVP clay material parameters found by Zwanenburg et al. (2019).

Parameters, Zwanenburg et al. (2019)	Value
Liquid limit, $w_l$ , [%]	165.6
Plastic limit, $w_p$ , [%]	55.5

Saturated weight, $\gamma_{sat}$ [kN/m <sup>3</sup> ]	13.2
Dry weight, $\gamma_{dry}$ [kN/m <sup>3</sup> ]	6.3
Water content, $w$ [%]	110.4
Initial void ratio, $e_0$	2.69
Compression index $C_c$ [-]	1.23

Zwanenburg et al., (2019) reached critical state stress conditions at the end of the large direct simple shear, LDSS, tests. A sketch of this device is shown below. Tests on this apparatus are conducted for plane strain conditions, with  $\epsilon_{zz} = 0$ , similar to the tests done with the biaxial apparatus. The following stresses are recorded, the effective out of plane horizontal stress,  $\sigma'_{zz}$ , the vertical effective stress,  $\sigma'_v$  and the shear stress,  $\tau_{xy}$ .

The LDSS apparatus has rectangular-shaped cell, allowing a 26 cm long, 22 cm wide and 6 to 12 cm high sample to be placed. The end boundaries are formed by a stack of plastic strips. As the sample is sheared, under true constant-volume conditions, the strips are guided to slide one over the other. Vertical loading is applied on the upper plate and shear loading is applied on the bottom plate. In the direction of  $z$ , the sample is confined by two glass plates.

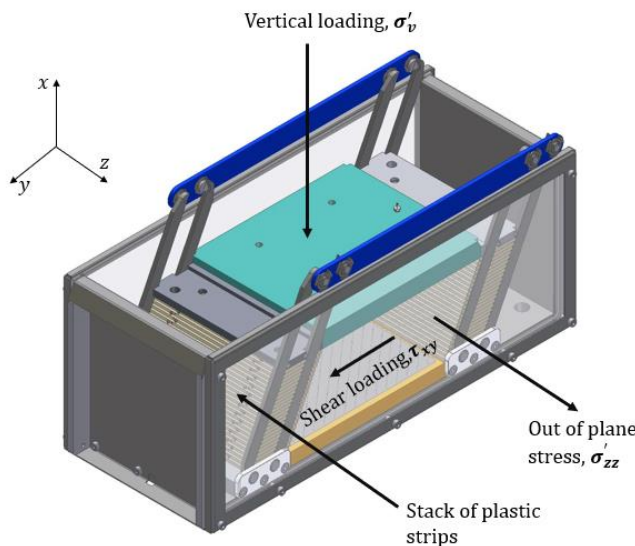


Figure 31: Sketch of LDSS by Den Haan et al. (2014). Altered for illustrative purposes.

Average values at critical state, distinguished for undrained and drained conditions, are shown in Table 3.

Table 3: Stress conditions at critical state found by Zwanenburg et al. (2019). Average value for three undrained LDSS tests and two drained LDSS test.

Test conditions	$\sigma'_v$ [kPa]	$\tau_{xy}$ [kPa]	$\sigma'_{zz}$ [kPa]
undrained	40.60	30.08	25.92
drained	75.00	47.09	84.58

To prepare the samples, Zwanenburg (2019) and Bizzarri et al., (1998) remoulded the clay under vacuum conditions and mixed it with water. Such a procedure changes the fabric of the intact clay, making it remoulded clay. Remoulding the material results in

near homogeneous properties throughout the sample making reproduction of tests less challenging.

Zwanenburg et al. (2018) reports two  $K_0$ -CRS tests with OVP clay. They find the hydraulic conductivity to depend on the void ratio shown in Figures 32 and 33. The relation between change in void ratio and change in hydraulic conductivity is given by Formula 7, with  $C_k$  defining the change in hydraulic conductivity.

$$C_k = \frac{\Delta e}{\log\left(\frac{k}{k_0}\right)} \quad (7)$$

For CRS *test 1* the initial hydraulic conductivity,  $k_{e_0}$ , was found to  $1.39 * 10^{-9} \frac{m}{s}$  and the final hydraulic conductivity,  $k_{e_1}$ , equals  $4.3 * 10^{-12} \frac{m}{s}$ . The fitted function gives a slope of 1.39, with the slope equal to  $\frac{1}{C_k}$ . The corresponding parameters are given in Table 4.

Table 4: OVP clay material parameters for CRS test 1 found by Zwanenburg et al. (2018).

Parameter, Zwanenburg et al. (2018)	Value
Initial hydraulic conductivity, $k_{e_0} [\frac{m}{s}]$	$1.39 * 10^{-9}$
Final hydraulic conductivity, $k_{e_1} [\frac{m}{s}]$	$4.3 * 10^{-12}$
Saturated weight, $\gamma_{sat} [kN/m^3]$	13.3
Dry weight, $\gamma_{dry} [kN/m^3]$	6.1
Water content	113.9
Initial void ratio $e_0$	2.79
Poisson's ratio $\nu [-]$	0.18
$\frac{\sigma'_{xx}}{\sigma'_{yy}}$ stress ratio initial, $K_0 [-]$	0.40

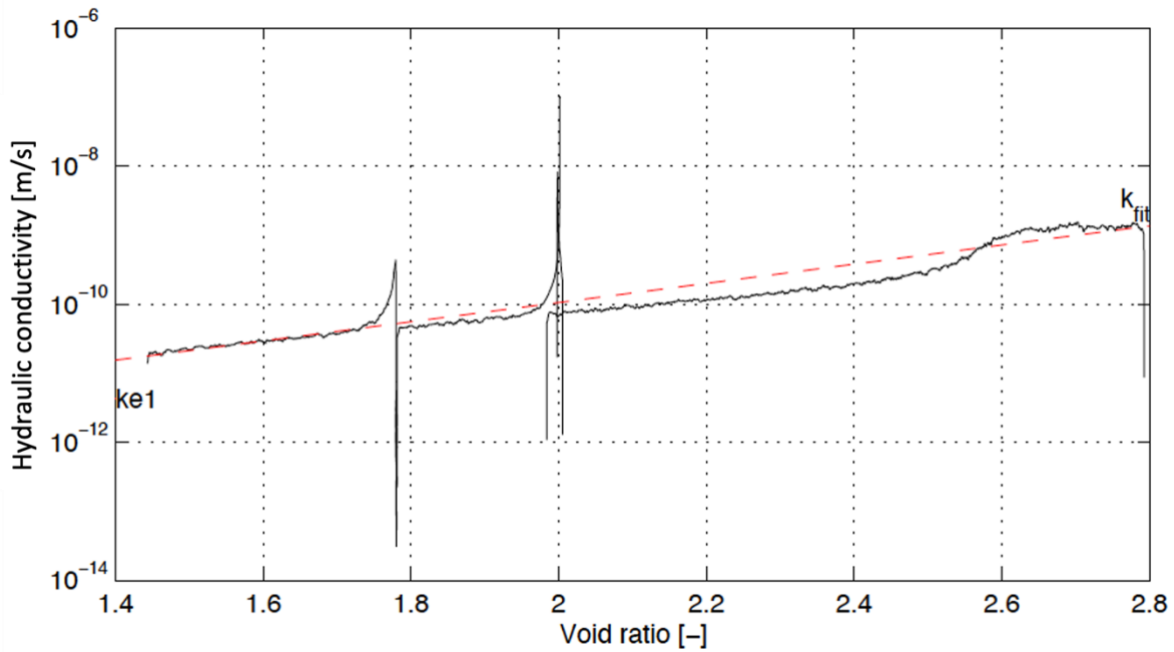


Figure 32: Void ratio versus hydraulic conductivity for CRS test 1 with OVP clay (Zwanenburg et al., 2018).

CRS test 13 gives  $k_{e_0} = 7.4 * 10^{-10} \frac{m}{s}$  and the final hydraulic conductivity,  $k_{e_1}$ , equals  $2.7 * 10^{-12} \frac{m}{s}$ . The fitted function gives a slope of 1.5. The corresponding parameters are given in Table 5.

Table 5: OVP clay material parameters for CRS test 13 found by Zwanenburg et al. (2018).

Parameter, Zwanenburg et al. (2018)	Value
Initial hydraulic conductivity, $k_{e_0} [\frac{m}{s}]$	$7.4 * 10^{-10}$
Final hydraulic conductivity, $k_{e_1} [\frac{m}{s}]$	$2.7 * 10^{-12}$
Saturated weight, $\gamma_{sat} [kN/m^3]$	13.3
Dry weight, $\gamma_{dry} [kN/m^3]$	6.4
Water content, $w [\%]$	107.0
Initial void ratio, $e_0$	2.62
Poisson's ratio, $\nu [-]$	0.18
$\frac{\sigma'_{xx}}{\sigma'_{yy}}$ stress ratio initial, $K_0 [-]$	0.38

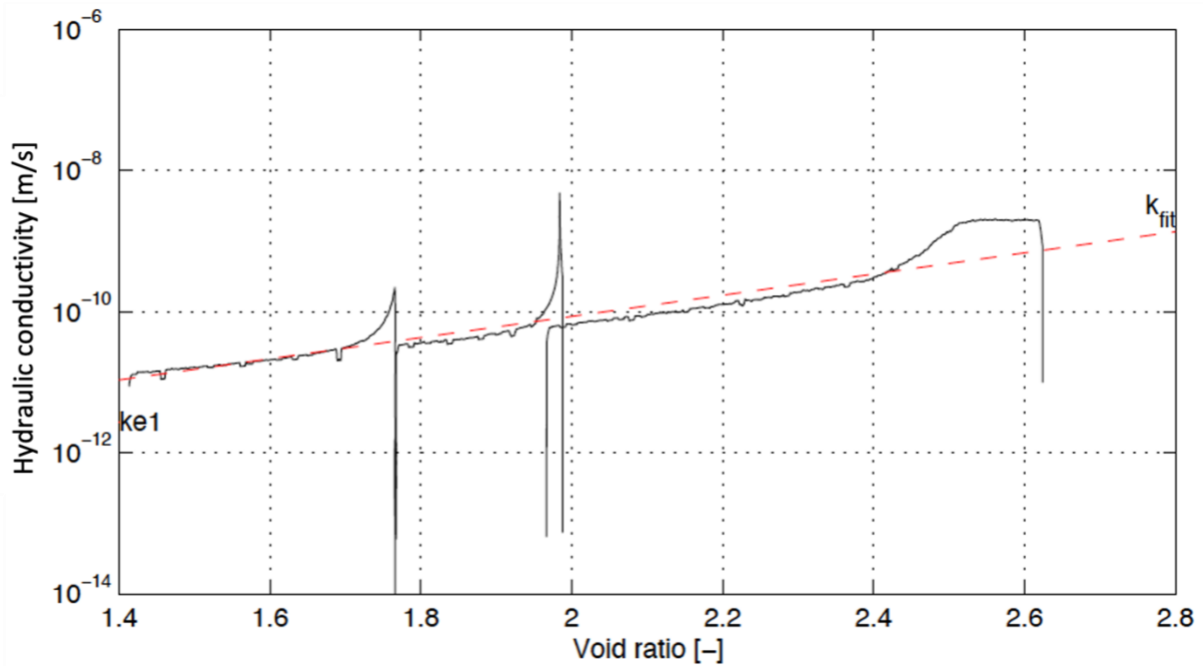


Figure 33: Void ratio versus hydraulic conductivity for CRS test 13 with OVP clay (Zwanenburg et al, 2018).

### 3.2. OVP clay used

For the test described in this thesis, remoulded OVP Clay received from Deltares, is used. It is consolidated under  $K_0$ -conditions for 27,27 days. The vertical total stress is controlled at  $\sigma_v = -40 \text{ kPa}$ . The value of  $K_0$  was found to be 0.43, giving a radial stress of,  $\sigma_r = -17.2 \text{ kPa}$ . The OVP clay prepared is allocated to Deltares project 11207357-051. The parameters shown in Table 6 are used for this project.

Table 6: Parameters OVP clay received by Deltares.

Parameter, Deltares	Value
Saturated weight, $\gamma_{sat}$ [ $\text{kN/m}^3$ ]	13.36
Initial void ratio, $e_0$ [-]	3.0
Cohesion, $c$ [kPa]	3.3
Dilatancy angle, $\psi$ [ $^\circ$ ]	0
Friction angle, $\varphi'$ [ $^\circ$ ]	27.7
Hydraulic conductivity, $k_x, k_y$ [ $\text{m/day}$ ]	$4.92 * 10^{-5}$
Modified compression index, $\lambda^*$ [-]	0.11349
Modified swelling index, $\kappa^*$ [-]	0.01149
Poisson's ratio for unloading - reloading, $\nu_{ur}$ [-]	0.15
Change in hydraulic conductivity, $C_k$ [-]	2.5

## 4. Numerical pre-analysis

A numerical finite element analyses is carried out using PLAXIS 2D CONNECT Edition V22 and PLAXIS 3D CONNECT Edition V22. These are special purpose finite element programs used to perform analysis for geotechnical applications. The intended biaxial loading schemes in the laboratory are re-created in this application. It is done to predict and understand the behaviour of the biaxial test to be performed in the laboratory. A stepwise explanation of the structure of analysis in PLAXIS is given in this chapter. The results in the laboratory are then compared to the corresponding numerical outcome in Chapter 5. Also, using PLAXIS, the effect of uncontrolled drainage conditions is implemented in the analysis to explain the results found in the laboratory.

The input parameters for the Soft Soil Creep material model used in PLAXIS are given in Table 7. These parameters are based on the parameters obtained by Deltares, introduced in Chapter 3.

Table 7: Input parameters for Soft Soil Creep model.

Parameters	Value
Initial void ratio, $e_0$ [-]	3.0
Modified compression index, $\lambda^*$ [-]	0.1135
Modified swelling index, $\kappa^*$ [-]	0.01149
Modified creep index, $\mu^*$ [-]	0.0724
Poisson's ratio for unloading - reloading, $\nu_{ur}$ [-]	0.15
$\frac{\sigma'_{xx}}{\sigma'_{yy}}$ stress ratio in normal consolidation state, $K_0^{nc}$ [-]	0.43
Effective cohesion, $c'_{ref}$ [kPa]	3.3
Friction angle, $\varphi'$ [°]	27.7
Dilatancy angle, $\psi$ [°]	0.0
Hydraulic conductivity, $k_x, k_y$ [m/day]	$4.92 \cdot 10^{-5}$
Change in hydraulic conductivity, $C_k$ [-]	2.5
Over consolidation ratio, OCR [-]	1

### 4.1. PLAXIS soil test

First, the *SoilTest* option is used to simulate the biaxial laboratory test. This is done using the Soft Soil Creep model. This tool simulates a basic soil test based on a single point. The *General* tab sheet is selected allowing definition of arbitrary stress and strain conditions.

The *SoilTest* simulation is used to gain a general understanding of the laboratory test to be performed. Two phases are simulated separately: a biaxial loading phase and a biaxial shearing phase. Ideally, the biaxial loading phase is a drained type of test and the biaxial shearing phase an undrained type of test. For the *SoilTest* analysis, the applicable drainage conditions are selected for the two phases individually.

During laboratory tests with the biaxial apparatus it is found that the apparatus does not allow controlled drainage conditions. For this, the two phases are analysed in more detail

using a 2D and 3D model including the uncontrolled drainage conditions in forthcoming paragraphs.

For the biaxial loading phase the test is set to a drained conditions. The initial stresses are set to  $\sigma_{xx} = -1 \text{ kPa}$ ,  $\sigma_{yy} = -1 \text{ kPa}$  and  $\sigma_{zz} = -1 \text{ kPa}$ . For the shearing phase the test is set to undrained conditions. The initial stresses are set to:  $\sigma_{xx} = -16 \text{ kPa}$ ,  $\sigma_{yy} = -40 \text{ kPa}$  and  $\sigma_{zz} = -16 \text{ kPa}$ . In the subsequent phase biaxial shearing is defined by setting  $\Delta\varepsilon_{xx} = 8 \%$ ,  $\Delta\varepsilon_{yy} = -8\%$  and  $\Delta\varepsilon_{zz} = 0 \%$ .

The isotropic stress versus deviatoric stress,  $p' - q$  plot for biaxial shearing is shown below. It reaches the failure line at  $\Delta\varepsilon_{xx} = 3.6 \%$ ,  $\Delta\varepsilon_{yy} = -3.6 \%$  and  $\Delta\varepsilon_{zz} = 0 \%$ . During the test, constant values of  $p_{excess} = 0 \text{ kPa}$  and  $\Delta\varepsilon_v = 0 \%$  are found. The volume remains constant during undrained conditions giving no generation of  $p_{excess}$ . Notably, the mean effective stress decreases upon failure.

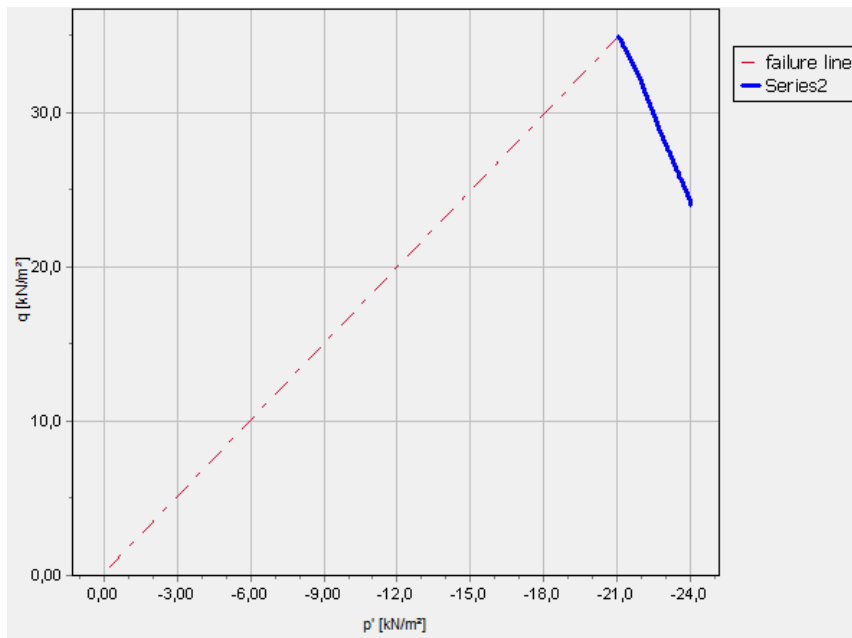


Figure 34:  $p' - q$  plot for biaxial shearing using the Soft Soil creep model.



## 4.2. PLAXIS 2D

The laboratory set-up of the biaxial test is re-created two-dimensionally in PLAXIS2D. The numerical set up for this program is discussed in this paragraph.

### 4.2.1. Project Properties

A complete finite element model is created with the *plane strain* boundary condition is selected in the project tab sheet. For this definition, displacements and strains in the *z*-direction are set to zero whilst accounting for the normal stresses in the *z*-direction.

The contour of the geometry model is taken as a quarter of the OVP clay sample used in the biaxial device. For the parameters  $x_{min}$ ,  $x_{max}$ ,  $y_{min}$  and  $y_{max}$  values of 0 m, 0.05 m, 0 m and 0.05 m are taken, respectively. The mesh is taken as a horizontal cut though at the bottom of the biaxial cell illustrated below.

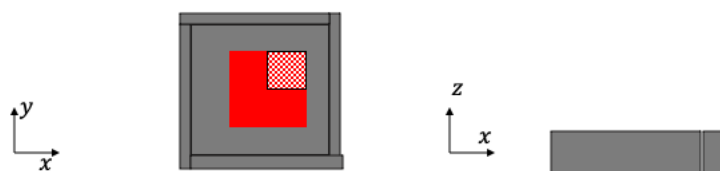


Figure 35: Position of PLAXIS2D mesh with respect to biaxial cell. On the left, quarter of the highlighted sample. On the right, cut through at bottom of plate.

As a reference, the red crosses with corresponding code abbreviation, represent the position of total stress sensors on the *x – y plane*. The blue circle gives the position of the water pressure sensor on the *x – y plane*. Nodes are selected based on the position of the sensor on the *x-y plane*. In the biaxial cell, the sensors are located at different position along the *z-axis*. For a 2D model this limits the precision of the simulation. As an example, the distance between S1 and S3 in the test set up will be larger than accounted for in this 2D model.

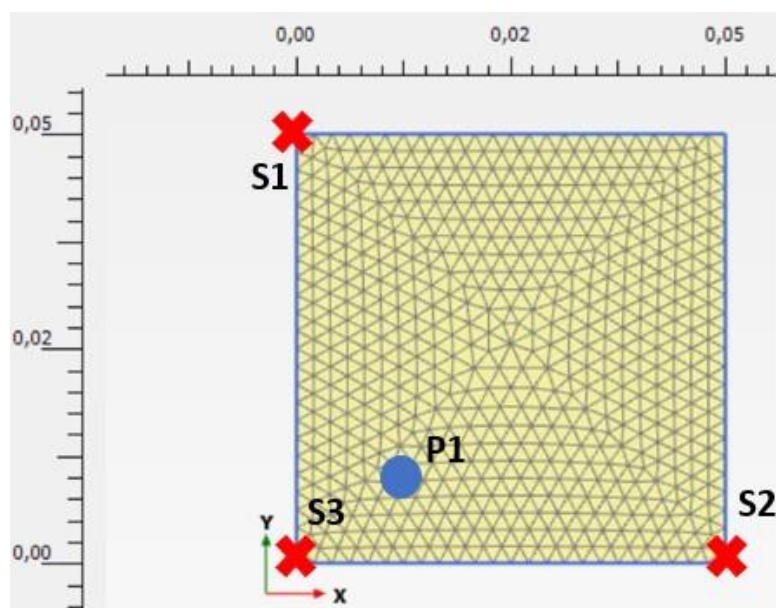


Figure 36: Sample mesh with position of sensors on the *x – y plane*.

The default 15-node triangle is used as element type. A *very fine* element distribution is selected.

#### 4.2.2. Material selection

The self-weight of the material can be disregarded when modelling the biaxial soil test. This is due to its relatively small proportion. Hence, the external displacements on the sample create stresses which are significantly greater compared to the material weight. Moreover, there is a mismatch between the gravitational force direction in PLAXIS2D and reality. In PLAXIS2D it works along the y-axis while along the z-axis in the test set up. This is accounted for in PLAXIS 2D by setting  $\sum M_{weight}$ , the total multiplier for the material weight, to zero.

The hydrostatic pressure, equal to the pressure of water multiplied by the depth, is desired to be zero throughout the sample as well. Setting  $\sum M_{weight}$  to zero will disregard the hydrostatic water pressures.

The phreatic level is set below the vertical position of the sample. The sample is situated in an unsaturated zone. In an unsaturated zone, active pore pressure is the effective saturation times the pore water pressure. By choosing the setting *ignore the suction*, the effective saturation has a uniform value of 100%. This leads to a saturated soil in the unsaturated zone, as desired.

#### 4.2.3. Initial stress configuration

This paragraph explains the method to reach a desired initial stress configuration. With the method any set of initial stresses can be reached. For instance, the stress configuration encountered in the laboratory. The stress configuration corresponding to the consolidation conditions at Deltares, as described below, are used as an example in this paragraph.

The OVP Clay received from Deltares, is consolidated under K0-conditions for 27.27 days. The vertical total stress is controlled at  $\sigma_v = -40 \text{ kPa}$ . A K0 test was done by Deltares giving a value of  $K_0 = 0.43$ . The radial stress on the sample is then  $\sigma_r = -17.2 \text{ kPa}$ . For a cubical block placed in the biaxial cell this corresponds to  $\sigma_{xx} = -17.2 \text{ kPa}$ ,  $\sigma_{yy} = -40 \text{ kPa}$  and  $\sigma_{zz} = -17.17 \text{ kPa}$ .

Two phases in PLAXIS2D are required to reach a desired configuration of total stresses. In the first phase, two uniform line loads of  $-17.2 \text{ kPa}$  are applied, acting in x- and y-direction. The linear elastic soil model is used. Formula C.7 gives the relation between the change in  $d\sigma_{zz}$  and the stresses  $d\sigma_{xx}$  and  $d\sigma_{yy}$  for this soil model. Setting  $\nu = 0.499$  generates  $d\sigma_{zz} = -17.17 \text{ kPa}$ . Note that letters in black, shown in Figure 37, are used as reference for the four individual sides of the sample throughout this report.

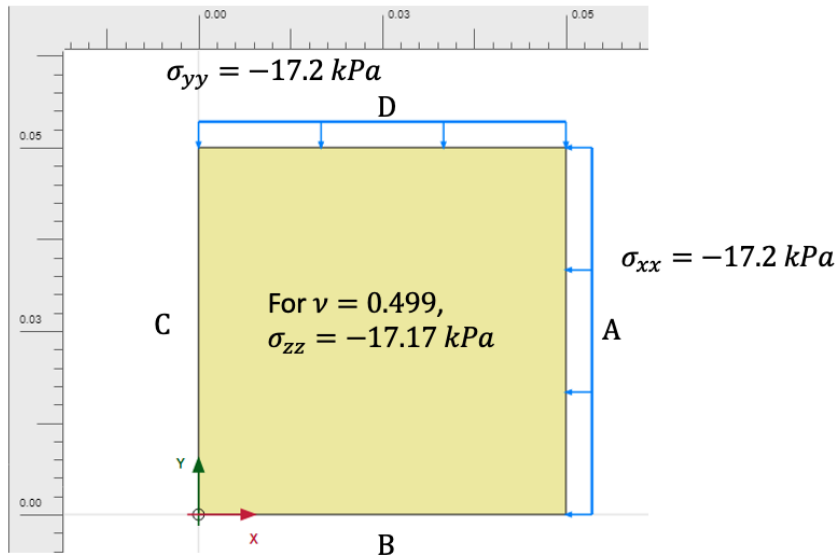


Figure 37: Phase 1 of initial stress generation

In the next phase, uniform line loads of  $-17.2 \text{ kPa}$  and  $-40 \text{ kPa}$  are applied in x- and y-direction, respectively. Setting  $\nu = 0$  will give  $d\sigma_{zz} = 0 \text{ kPa}$ . At the end of these two phases the following stresses are found:  $\sigma_{xx} = -17.2 \text{ kPa}$ ,  $\sigma_{yy} = -40 \text{ kPa}$  and  $\sigma_{zz} = -17.17 \text{ kPa}$ . For both phases described above the drainage type is set to *drained* allowing no excess pore pressure to be generated. The total stresses shown are equivalent to the effective stresses.

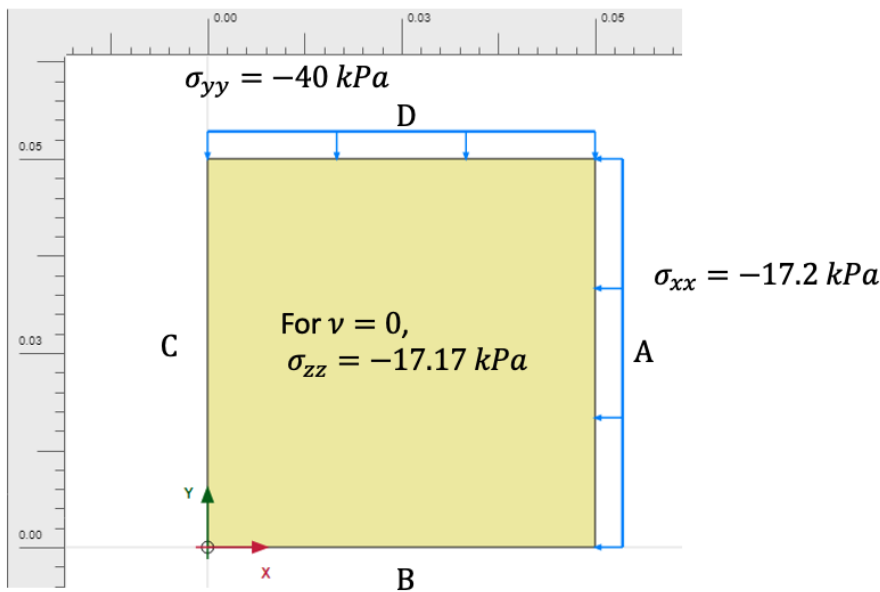


Figure 38: Phase 2 of initial stress generation.

The line displacements and time for both these phases are shown below in Table 8.

Table 8: Line displacement, time and phase type for initial stress configuration.

Phase	Line displacement side A [x, y]	Line displacement side B [x, y]	Line displacement side C [x, y]	Line displacement side D [x, y]	Time [days]	Calculation type

<b>Initial stress configuration phase 1 &amp; 2</b>	[free, free]	[free, fixed]	[fixed, free]	[free, free]	0	Plastic
---	--------------	---------------	---------------	--------------	---	---------

The initial stress configuration is used to reach any set of stresses. These can be made equivalent to the stresses found in a biaxial test prior to the biaxial loading or prior to a biaxial shearing phase. For the phases described above, displacements obtained are reset to zero at the beginning of the next phase.

#### 4.2.4. Relaxation

A relaxation phase is analysed in PLAXIS2D to simulate the state of relaxation. The plates remain stationary and the volume constant. Continued decrease of volume during biaxial loading, with the minimum displacement rate, will generate extremely large stress values. Therefore, phases of relaxation are alternated with phases of biaxial loading in the laboratory. These relaxation phases can be added to the numerical simulation. The prescribed displacements and phase type are given below.

Table 9: Line displacements and phase type for the relaxation phase.

Phase	Line displacement side A [x, y]	Line displacement side B [x, y]	Line displacement side C [x, y]	Line displacement side D [x, y]	Calculation type
<b>Relaxation</b>	[fixed, free]	[free, fixed]	[fixed, free]	[free, fixed]	Consolidation

During the numerical simulation of this phase the excess pore pressure dissipates out of the sample via the seepage boundaries. This is accompanied by a decrease in total stress throughout the sample.

#### 4.2.5. Biaxial test set up in PLAXIS2D

In the next two paragraphs the laboratory displacement schemes are simulated in PLAXIS2D using the Soft Soil Creep model. These are two possible phases, starting with a biaxial loading phase and followed by a shearing phase. The initial stress configuration is used as a starting point.

##### 4.2.5.1. Groundwater flow boundary conditions

Cheng (2004) described the difficulty of managing the drainage conditions in the biaxial device. It is described that water can drain out of the biaxial cell through the small gaps between the plates. This is also seen during the tests performed with the biaxial apparatus in this thesis.

It is implemented in the numerical simulation by setting the groundwater flow boundary conditions in PLAXIS2D accordingly. Apart from the uncontrolled drainage at the boundary of the biaxial cell, different drainage conditions are imposed at the centre of the biaxial cell, described in Appendix A. These drainage conditions are implemented individually in PLAXIS and used based on the test to be recreated.

The design of Appendix A.1 is represented by setting the groundwater flow boundary condition at the centre of the sample to seepage. The water can flow out through the porous stone. This is shown in figure 39 with the seepage boundary condition indicated by the blue accolades.

For sides A and D, gaps are measured between the bottom plate and the vertical plates. Water can flow out through the tiny gaps. Therefore, groundwater flow boundary conditions are set to seepage at sides A and D. With this design a uniform boundary flow condition is assumed for sides A and D. This does not coincide to the laboratory, where only the gaps allow for drainage, and not sides A and D in their totality.

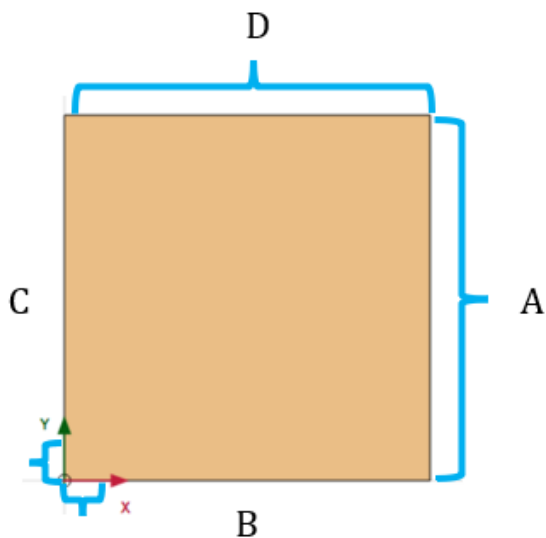


Figure 39: Sample with drainage conditions set to seepage at sides A and D and at the centre of the sample.

In a later stage of the laboratory experiments, the porous stone is not connected to a drainage outlet. This signifies undrained conditions in the centre of the sample, marked by the drainage conditions shown in Figure 40.

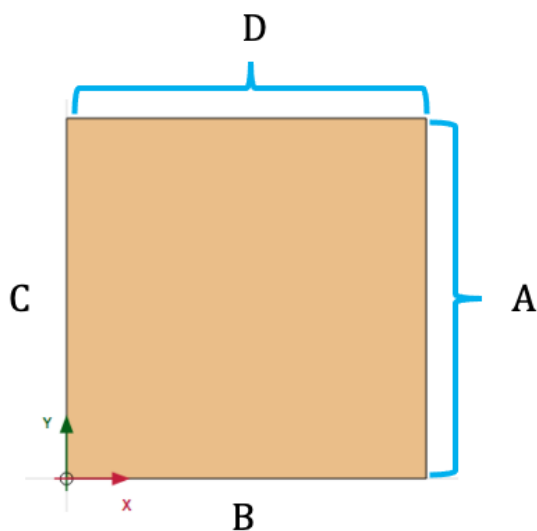


Figure 40: Sample with drainage conditions set to seepage at sides A and D.

#### 4.2.5.2. Biaxial loading

To reach suitable values of effective stress, phases of biaxial loading are carried out first in the laboratory. The biaxial apparatus allows loading by biaxial loading or 1D loading. For biaxial loading the OVP Clay is displaced in two directions. For convenience, Table 10 below provide an overview of the prescribed displacements and time corresponding to the biaxial loading phase introduced in this paragraph.

Table 10: Line displacements, time and calculation type used for biaxial loading example in this paragraph.

Phase	Line displacement side A [x, y]	Line displacement side B [x, y]	Line displacement side C [x, y]	Line displacement side D [x, y]	Time [days]	Calculation type
<b>Biaxial loading</b>	[-0.1 mm, free]	[free, fixed]	[fixed, free]	[free, -0.1 mm]	0.006	Consolidation

The initial stress configuration was previously introduced in Paragraph 4.2.3. This phase can precede the biaxial loading step to reach any set of initial set of total stresses. For the example presented in this paragraph the initial stresses are set to  $\sigma'_{xx} = -1 \text{ kPa}$ ,  $\sigma'_{yy} = -1 \text{ kPa}$  and  $\sigma'_{zz} = -1 \text{ kPa}$ . The drainage conditions allowing seepage only at sides A and D are used, as shown in Figure 40.

Consolidation occurs when excess pore pressure can drain out of the sample due to loading of the sample. Although difficult to manage, this is what is expected during this phase. Pore pressure seeps out of the sample via sides A and D. This consolidation behaviour can be analysed by selecting the *consolidation* calculation type. This makes it possible to analyse the dissipation of excess pore pressure in a saturated clay type soil as function of time (PLAXIS2D reference manual, 2021).

To calculate the groundwater flow and consolidation, it is required to give input of the permeabilities. This is done with parameters  $k_x$  and  $k_y$ , the hydraulic conductivity in the principal directions  $x$  and  $y$ , respectively, allowing for anisotropic hydraulic conductivity of the soil. These are given by,  $k_x = k_y = 4.92 * 10^{-5} \frac{m}{day}$ .

For biaxial loading the sample is displaced in two directions, which is shown in Figure 41. The line displacement is specified on all four sides of the sample and given in Table 10. The fixities are indicated by the small green parallel lines (||) in Figure 41. The prescribed displacements are shown by the lines adjacent to the arrows in purple.

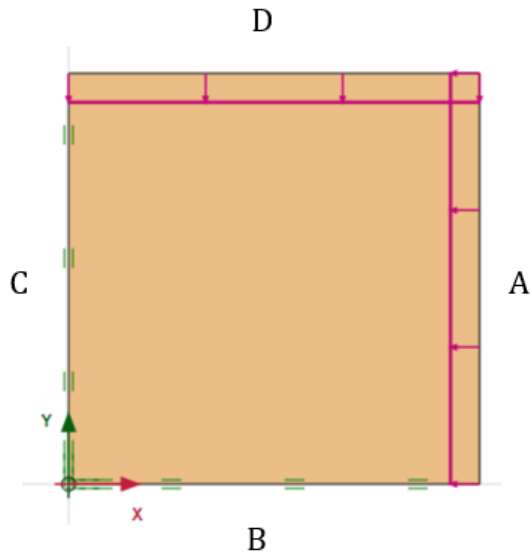


Figure 41: Biaxial loading with prescribed displacements.

This leads to a deformed mesh as shown in Figure 42. The outer contour gives the dimensions of the mesh prior to biaxial loading. Biaxial loading leads to the area marked with the element distribution contour.

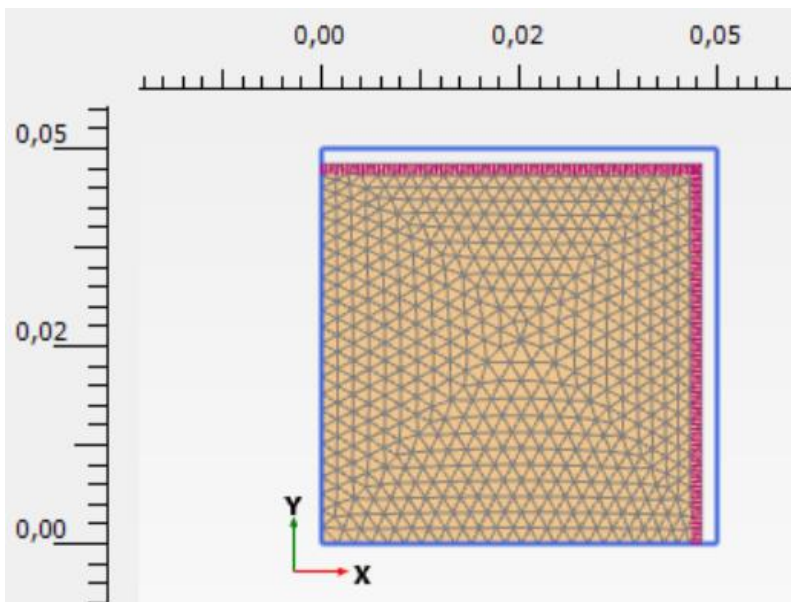


Figure 42: Deformed mesh due to biaxial loading. Deformation scaled up to 20 times.

The deformed mesh is found after a prescribed displacement of  $-0.1 \text{ mm}$  both in x- and y-direction. To match the minimum displacement rate of  $0.00021 \frac{\text{mm}}{\text{s}}$ , the time during this phase is set at  $0.006 \text{ days}$ .

The curves for total stresses  $\sigma_{xx}$ ,  $\sigma_{yy}$  and  $\sigma_{zz}$  are given below for the biaxial loading phase. The curves are generated according to the position of total stress measurement in the laboratory; total stresses  $\sigma_{xx}$ ,  $\sigma_{yy}$  and  $\sigma_{zz}$  are taken for S2, S1 and S3, respectively. These positions were presented in Figure 36. All three total stresses show a similar increase in total stress.



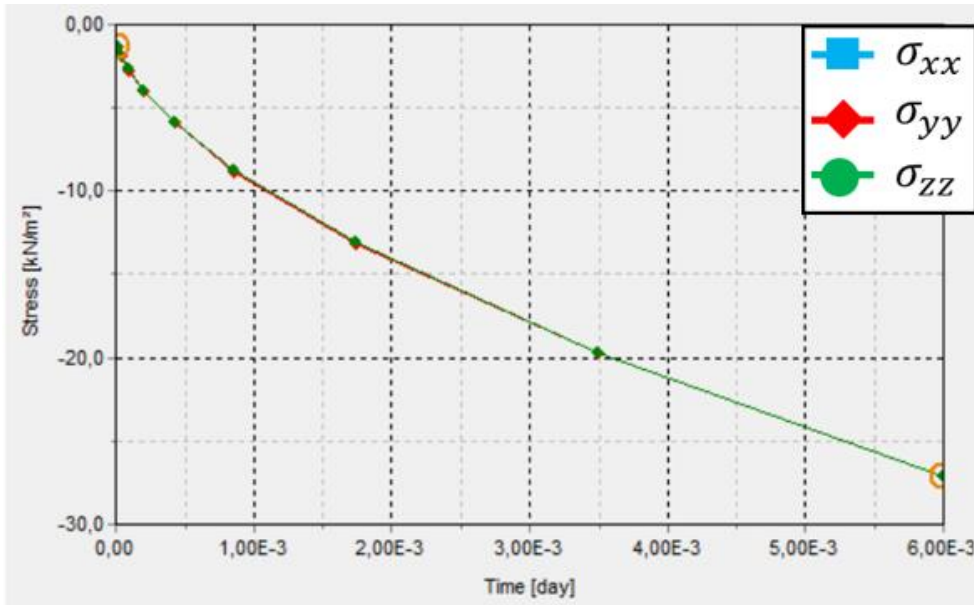


Figure 43: Total and effective stresses for biaxial loading of -0.1 mm.

The development of the excess pore pressure mesh is shown below for  $t = 0.003 \text{ days}$  and  $t = 0.006 \text{ days}$ . The displacement leads to  $\Delta\varepsilon_v = < 0 \%$ , generating excess pore pressure in the sample. Simultaneously, excess pore pressure is allowed to drain out of the sample with boundary flow conditions on sides A and D set to seepage. Zero excess pore pressures are found at the seepage boundaries. Gradually increasing towards the centre of the sample. For  $t = 0.003 \text{ days}$  the excess pore pressure is at a maximum value of -18.7 kPa

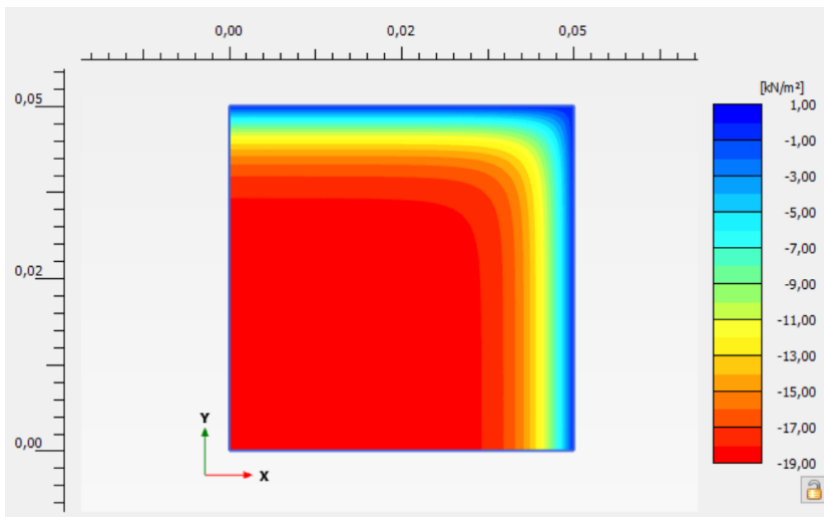


Figure 44: Excess pore pressure mesh for biaxial loading of -0.1 mm at  $t = 0.003 \text{ days}$ .

At the end of the phase the excess pore pressure distribution increases more gradually towards the centre. At the centre, the excess pore pressure equals  $-28.0 \text{ kPa}$ .

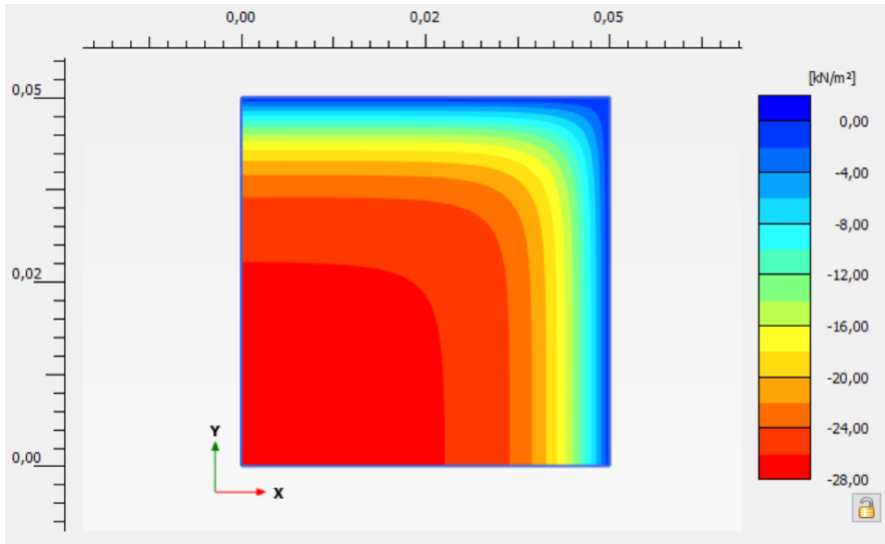


Figure 45: Excess pore pressure mesh for biaxial loading of -0.1 mm at  $t = 0.006$  days.

$\sigma_{xx}$ ,  $\sigma_{yy}$  and  $\sigma_{zz}$  in the total stress plot above show an analogous increase for the biaxial loading step. The total stress is made up of pore pressure, shown above, and effective stress. The meshes at  $t = 0.006$  days for effective stress in direction of x, y and z,  $\sigma'_{xx}$ ,  $\sigma'_{yy}$  and  $\sigma'_{zz}$ , respectively, are given below.

The mesh for  $\sigma'_{xx}$  is given. The values for  $\sigma'_{xx}$  are zero towards the centre of the mesh. At the boundary between plate and sample in x-direction,  $\sigma'_{xx} = -20.0 \text{ kPa}$ . Excess pore pressure dissipates through the gaps. As the active plate moves in x-direction it generates  $\sigma'_{xx}$  making up  $\sigma_{xx}$ . According to this numerical analysis, the value of  $\sigma_{xx}$  measured at the sensor solely consists of effective stress.

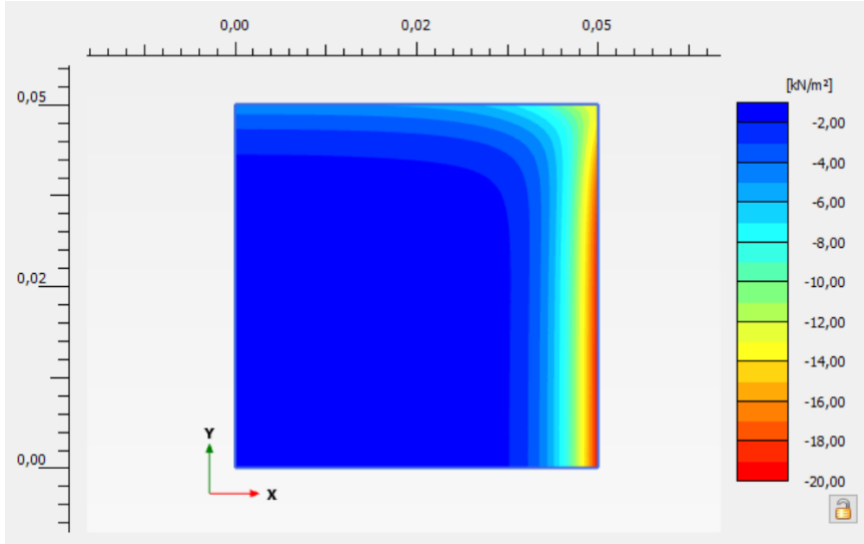


Figure 46:  $\sigma'_{xx}$  mesh for biaxial loading of -0.1 mm at  $t = 0.006$  days.

A similar observation is seen for the mesh for  $\sigma'_{yy}$ . Again, the value of  $\sigma_{yy}$  measured at the sensor solely consists of effective stress.

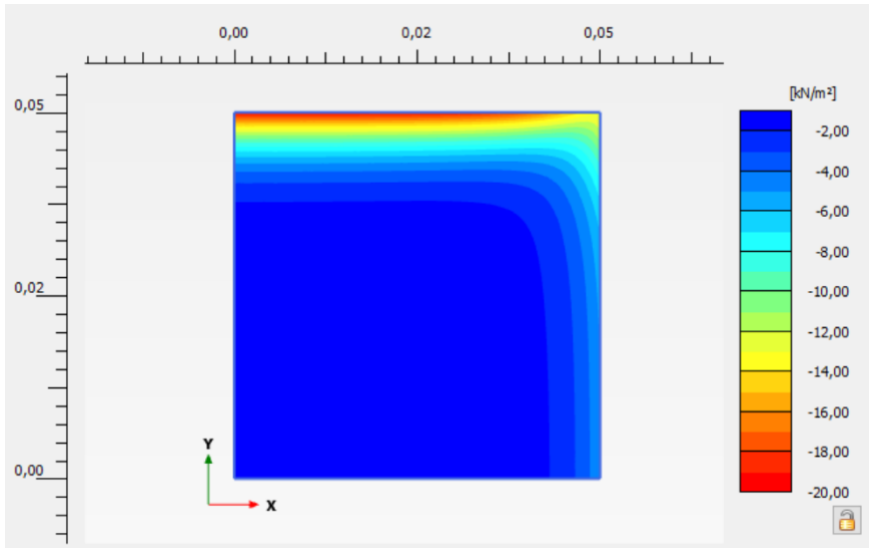


Figure 47:  $\sigma'_{yy}$  mesh for biaxial loading of  $-0.1 \text{ mm}$  at  $t = 0.006 \text{ days}$ .

The mesh for  $\sigma'_{zz}$  is given below. The value of  $\sigma'_{zz}$  is at maximum  $\sigma'_{xx} = -20.0 \text{ kPa}$  and found at the interface between sample and plate. At the position of total stress measurement,  $\sigma'_{zz}$  approaches zero and  $\sigma_{zz}$  is made up of pore pressure.

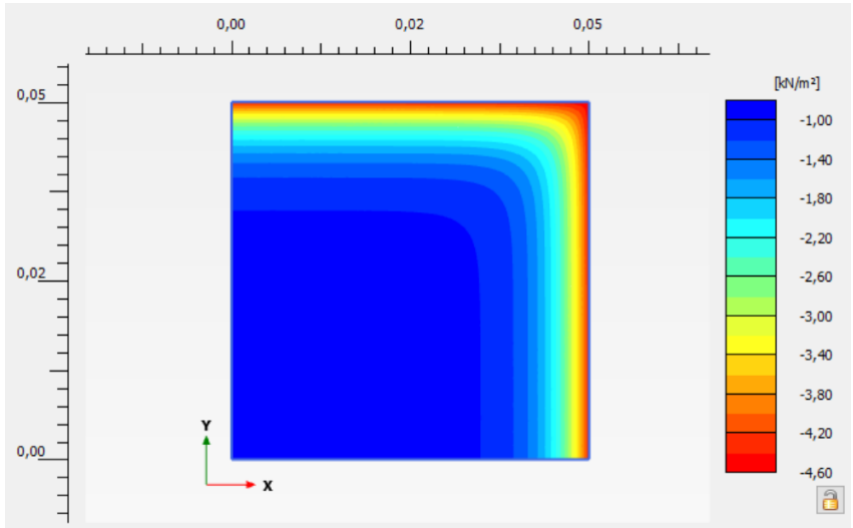


Figure 48:  $\sigma'_{zz}$  mesh for biaxial loading of  $-0.1 \text{ mm}$  at  $t = 0.006 \text{ days}$ .

**4.2.5.3. 1D consolidation**

Another option is to displace the sample in one dimension. A prescribed compressional displacement can be set in either x- or y-direction. The prescribed displacements are visualized in Figure 49.

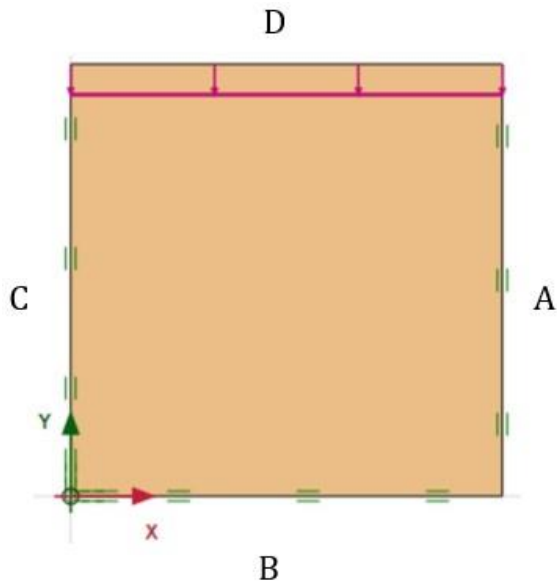


Figure 49: 1D consolidation with prescribed displacements.

The corresponding prescribed displacements and calculation type are given in Table 11.

Table 11: Prescribed displacements for 1D consolidation.

Phase	Line displacement side A [x, y]	Line displacement side B [x, y]	Line displacement side C [x, y]	Line displacement side D [x, y]	Calculation type
1D loading	[fixed, free]	[free, fixed]	[fixed, free]	[free, - 1 mm]	Consolidation

#### 4.2.5.4. Biaxial shearing

In biaxial shearing the sample is extended in one direction whilst in the other direction a compressional displacement is imposed, shown in Figure 50. It chosen to use the initial stress configuration  $\sigma'_{xx} = -10 \text{ kPa}$ ,  $\sigma'_{yy} = -10 \text{ kPa}$  and  $\sigma'_{zz} = -10 \text{ kPa}$  as starting point. The boundary flow conditions are corresponding to the groundwater flow boundary conditions introduced in Paragraph 4.2.5.1, creating partly drained conditions.

Next, the sample is sheared until failure using the Soft Soil Creep model. Again, the line displacement is specified on all four sides of the sample and given in the table below. Note that this phase has time set at 0.4 days, this is not possible in the laboratory with a displacement of 1 mm. In reality, phases of biaxial shearing have to be altered with phases of relaxation to reach this displacement in the set time.

Phase	Line displacement side A [x, y]	Line displacement side B [x, y]	Line displacement side C [x, y]	Line displacement side D [x, y]	Time [days]	Calculation type
Biaxial shearing	[1 mm, free]	[free, fixed]	[fixed, free]	[free,-1 mm]	0.4	Consolidation

A prescribed displacement is defined in subsequently the x and y-direction shown in purple in the figure below.

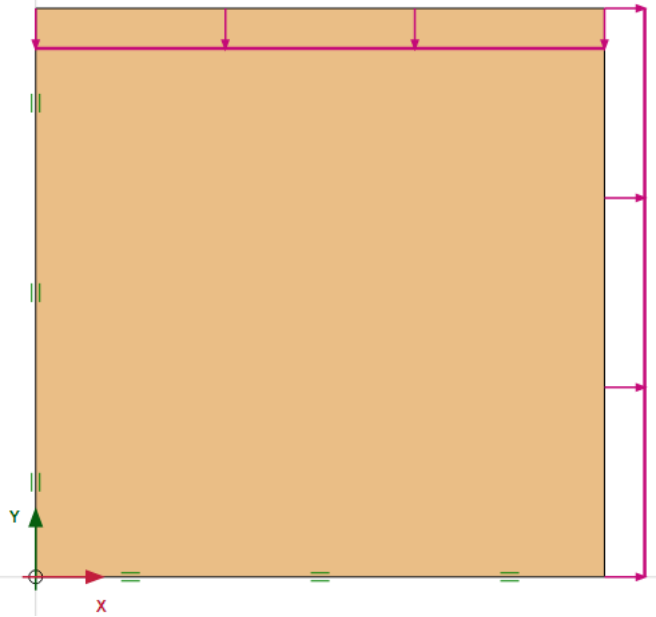


Figure 50: Biaxial shearing with corresponding prescribed displacement.

Displacements of  $-1\text{ mm}$  and  $1\text{ mm}$  are applied in y-direction and x-direction, respectively. This leads to compression in y-direction and extension in x-direction as shown by the deformed mesh in Figure 51.

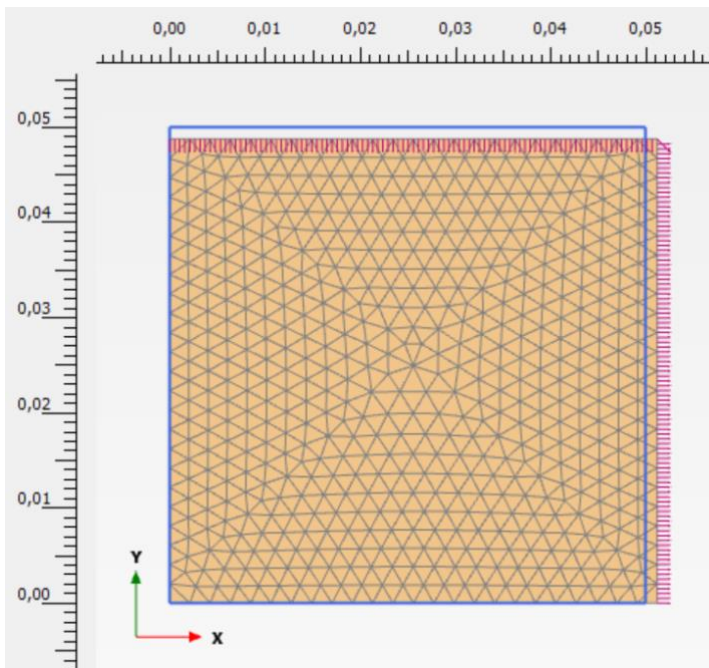


Figure 51: Deformed mesh due to biaxial shearing. Deformation scaled up to 0.2 times

The effective stress development corresponding to this phase are shown in the figure.

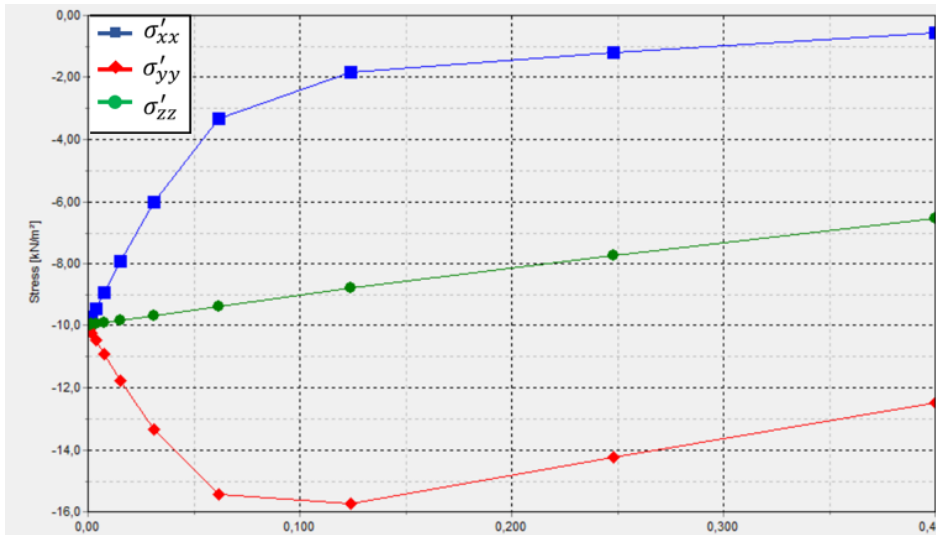


Figure 52: Time versus total and effective stress plot for biaxial shearing.

The relates to the  $p'$ - $q$  plot shown below. The expansion of the yield cap is indicated by the blue semi-circles. The red dotted line represents the critical state line which is reached during biaxial shearing.

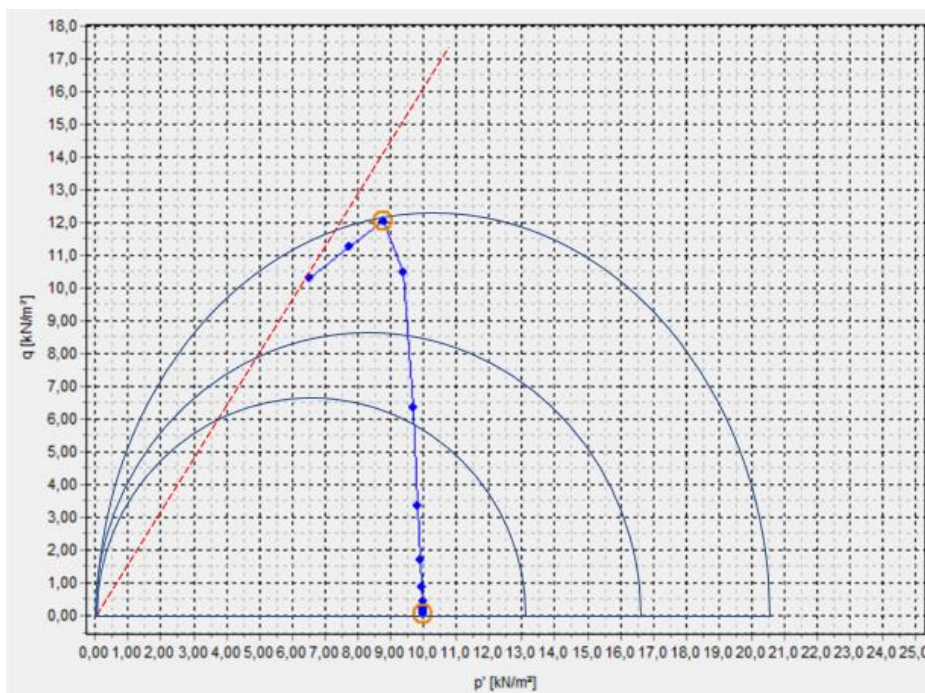


Figure 53:  $p'$ - $q$  plot for biaxial shearing.

#### 4.2.5.5. Excess pore pressure development during biaxial shearing.

The behaviour of pore pressure during biaxial shearing is analysed by changing the scenario. A biaxial loading phase and a relaxation phase are added, foregoing the biaxial shearing phase. The boundary flow conditions for all boundaries during the biaxial shearing phase are set to *undrained*. This allows excess pore pressure to be generated. Note, this conflicts with the groundwater flow boundary conditions introduced in Paragraph 4.2.5.1.

The excess pore pressure distribution following the phase of biaxial shearing is shown below. There is no build-up of excess pore pressure due to biaxial shearing, solely redistribution. Keeping the volume constant and not applying external load leads to no significant excess pore pressure generation during biaxial shearing.

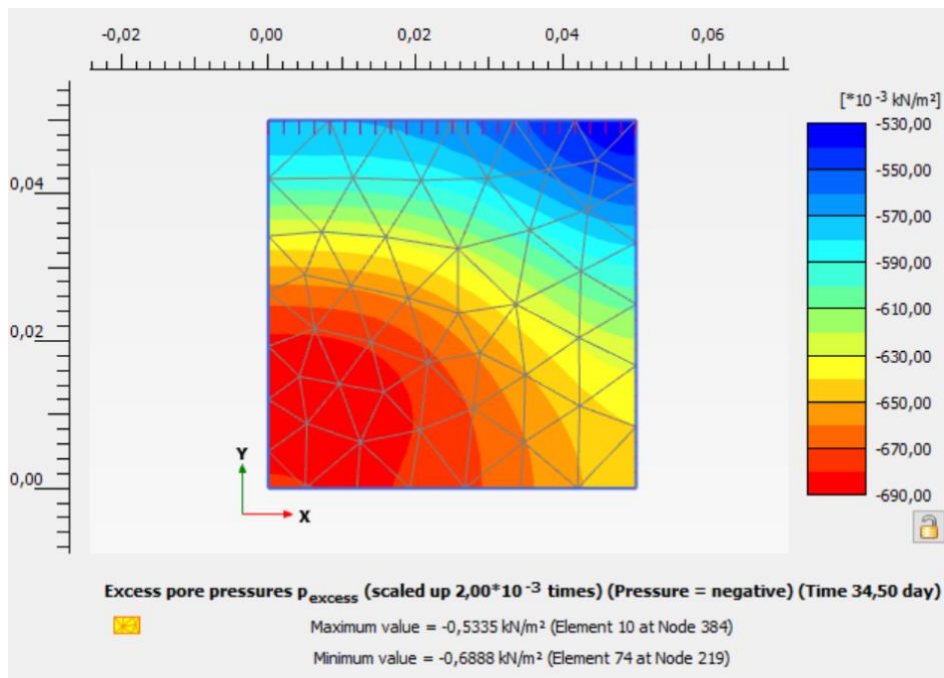


Figure 54: Excess pore pressure distribution due to biaxial shearing following biaxial loading.



### 4.3. PLAXIS 3D

The two-dimensional approach in PLAXIS is given in Paragraph 4.2, which represents the sample in the biaxial cell in a two-dimensional plane. This gives some limitations when making the translation to the situation in reality. The measurement of total stress occurs at different positions with respect to the z-axis, seen in Paragraph 2.7.1. Also, the boundary flow conditions turn out to be more complicated. These are not symmetrical and differ with position along the axis. Assuming the entire x- and y- boundary to be identical along the z-axis does not justify the conditions found in the laboratory. It is possible to incorporate this in a three-dimensional problem instead of a two-dimensional approach.

#### 4.3.1. Project properties

A finite element model is created with a three-dimensional volume. The boundary value points of the volume are:  $[x_{min}, x_{max}, y_{min}, y_{max}, z_{min}, z_{max}] = [0, 10, 0, 10, 0, 5]$ , given in *mm*. This corresponds to the dimensions of the soil sample placed in the biaxial cell. The geometry of the model is represented below, with a view from underneath the model along the isotropic coordinate axis. The position of the three out of six total stress sensors, which can be seen from this position, and the position of water pressure measurement are marked with red circles and a dotted blue circle, respectively.

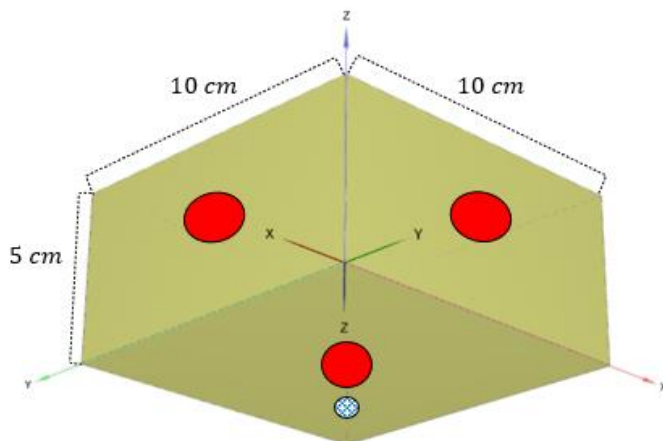


Figure 55: Model in PLAXIS3D with indication of sensor position.

A default 10-noded element type is selected, and the *very fine* element distribution is selected.

For the analysis for PLAXIS3D the two extra sides required are annotated by the letters 'E' and 'F'. All sides with abbreviation are shown below in a top view and side view cross section.

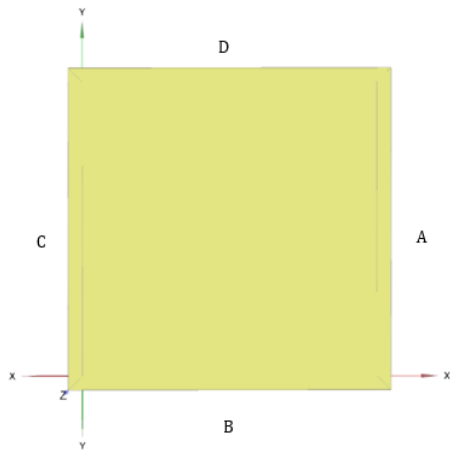


Figure 56: Top view of mesh in PLAXIS3D with side annotation.

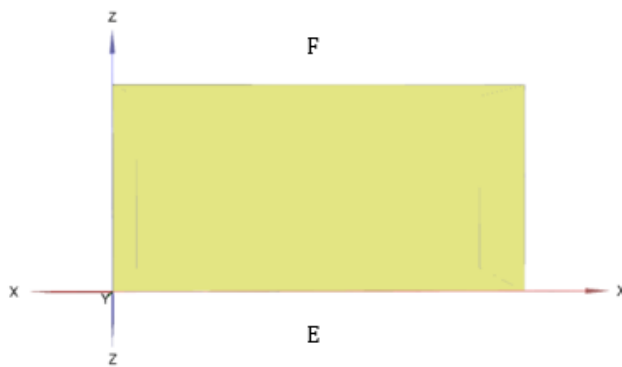


Figure 57: Side view of mesh in PLAXIS3D with side annotation.

### 4.3.2. Initial stress configuration

In PLAXIS3D a single phase is required to reach any desired set of initial stresses. On sides A, B and F a surface load is given with any desired value. This results in the mesh uniformly obtaining the total stress value corresponding to the direction of applied load. The surface loads applied to the mesh are shown below.

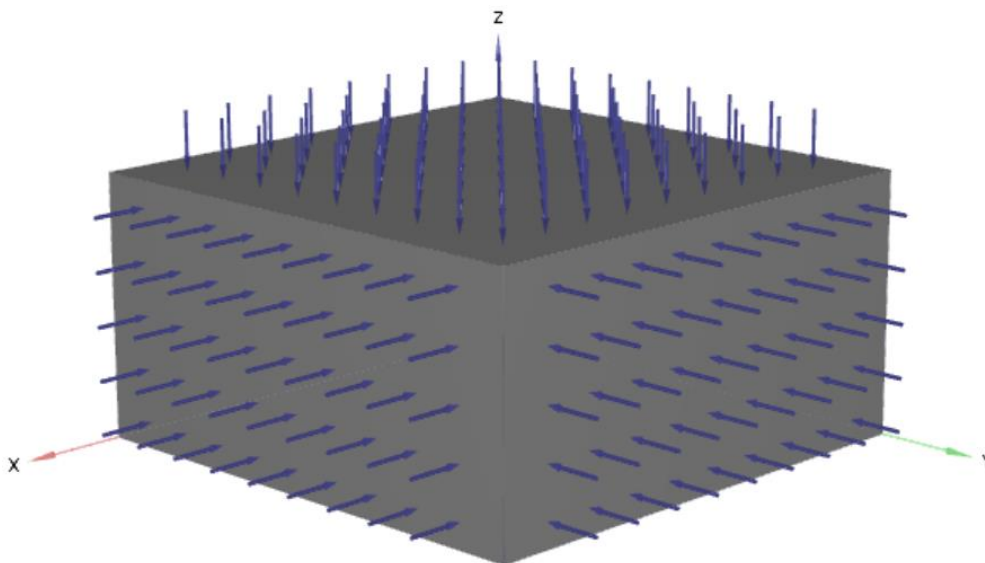


Figure 58: Mesh in PLAXIS3D with loads for initial stress configuration.

The deformation model conditions for all six sides, time and calculation type are given below.

Table 12: Boundary conditions for initial stress configuration.

Phase	Boundary 'A'	Boundary 'B'	Boundary 'C'	Boundary 'D'	Boundary 'E'	Boundary 'F'	Time [days]	Calculation type
Initial stress configuration	Free	Normally fixed	Normally fixed	Free	Normally fixed	Free	0	Plastic

#### 4.4. Biaxial test set up in PLAXIS3D

In the next two paragraphs the laboratory displacements schemes are simulated in PLAXIS3D using the Soft Soil Creep model. Again, biaxial loading and shearing are presented.

##### 4.4.1. Groundwater flow boundary conditions.

For the 2D model it was mentioned that the groundwater flow boundary conditions do not fully resemble to the condition for the test set up. The boundary differentiates with position along the z-axis. In a 3D model this can be approached more consistently. It is chosen to model the design without a drainage outlet at the centre of the bottom plate. Using a feeler gauge the gaps between the metal plates, both horizontally and vertically, are measured. Gaps ranging from 0.05 mm to 0.2 mm are found. At the boundary of the mesh, surfaces with dimensions according to the gaps, are created. The position of these surfaces are represented by the rectangular surfaces at the border between two plates in the 3D figure below.

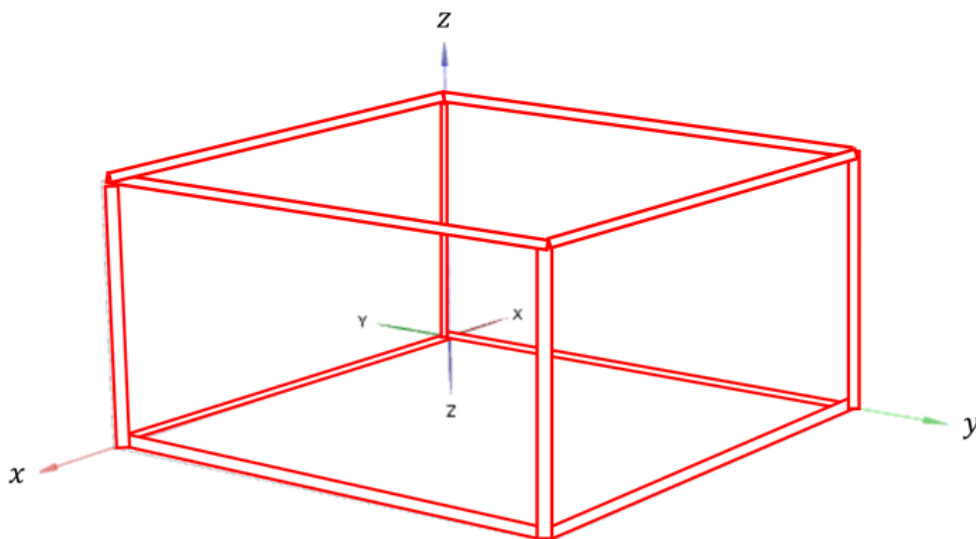


Figure 59: Gaps found in the test set up indicated for the PLAXIS3D mesh.

They are also shown for the top view and side view. Note that the dimensions shown are exaggerated. In the numerical model the width of the surface is taken according to the value applicable for the corresponding side from 0.05 mm to 0.2 mm.

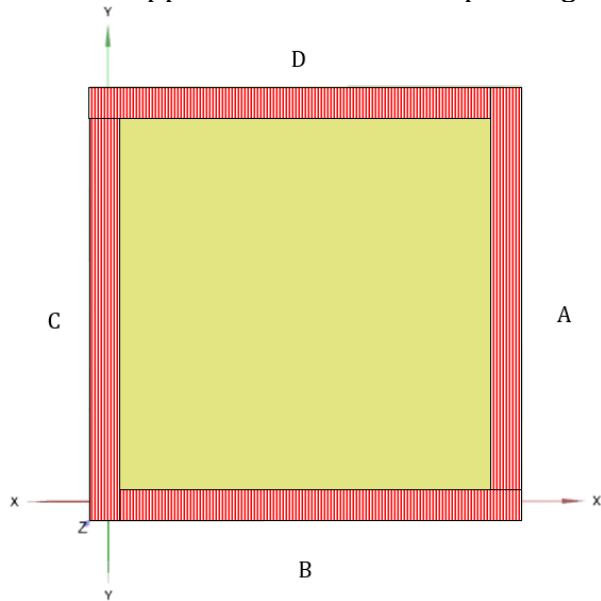


Figure 60: Top view drainage boundaries in PLAXIS3D.

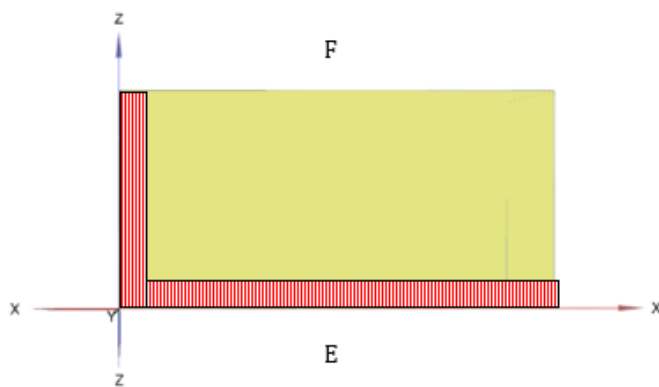


Figure 61: Side view drainage boundaries in PLAXIS3D.

This gives 12 small surfaces which are set to drainage as boundary flow conditions.

#### 4.4.2. Biaxial loading

Biaxial loading in PLAXIS3D is described in this paragraph using the Soft Soil Creep model. The same displacement used for presentation of PLAXIS2D is taken as an example for this phase.

Table 13 below provide an overview of the prescribed displacements and time corresponding to the biaxial loading phase introduced in this paragraph. Note that all four vertical sides are compressing but have opposite signs as they work in opposing direction of the axis.

Table 13: Prescribed displacements for biaxial loading in PLAXIS3D.

Phase	Line displacement side A [x,y,z]	Line displacement side B [x,y,z]	Line displacement side C [x,y,z]	Line displacement side D [x,y,z]	Line displacement side E [x,y,z]	Line displacement side F [x,y,z]	Time [days]	Calculation type
Biaxial loading	[-0.1 mm, free, fixed]	[free, 0.1 mm, fixed]	[0.1 mm, free, fixed]	[free, -0.1 mm, fixed]	[free, free, fixed]	[free, free, fixed]	0.006	Consolidation

The example provided for biaxial loading in PLAXIS2D is recreated for PLAXIS3D. The initial stresses are set to  $\sigma'_{xx} = -1 \text{ kPa}$ ,  $\sigma'_{yy} = -1 \text{ kPa}$  and  $\sigma'_{zz} = -1 \text{ kPa}$ . The drainage conditions are set corresponding the conditions described in the previous paragraph. This leads to the deformed mesh shown below.

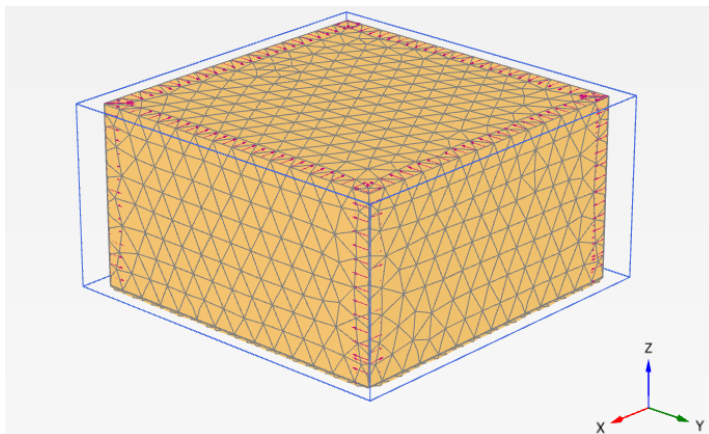


Figure 62: Deformed mesh for biaxial loading PLAXIS3D.

The time versus total stress plot is given. The total stresses are taken for the node corresponding to the position of the total stress measurement in the laboratory. Equivalent to the analysis in PLAXIS2D, the total stresses in three axial directions increase equivalently. A maximum value of -113.7 kPa is reached, giving a larger increase in total stress compared to the biaxial loading step analyzed in PLAXIS2D.

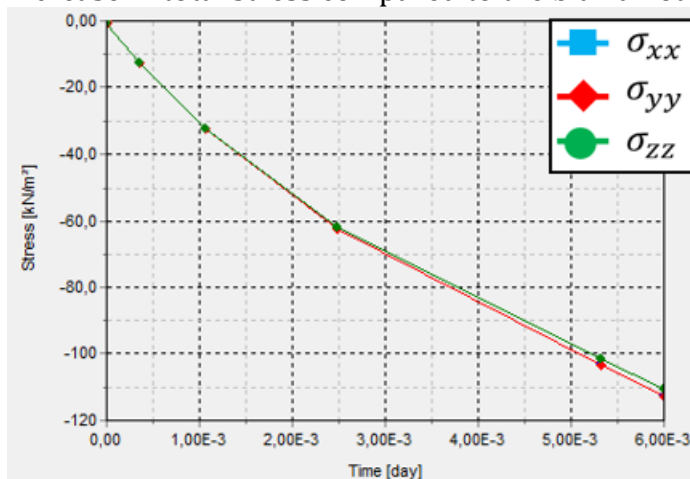


Figure 63: Time versus total stress plot in PLAXIS3D.

The 3D excess pore pressure mesh for biaxial loading is shown below halfway through the phase at  $t = 0.003 \text{ days}$ . At the position of the gaps the excess pore pressure value equals zero. Further away from these gaps, the excess pore pressure takes values of up to  $73.1 \text{ kPa}$ .

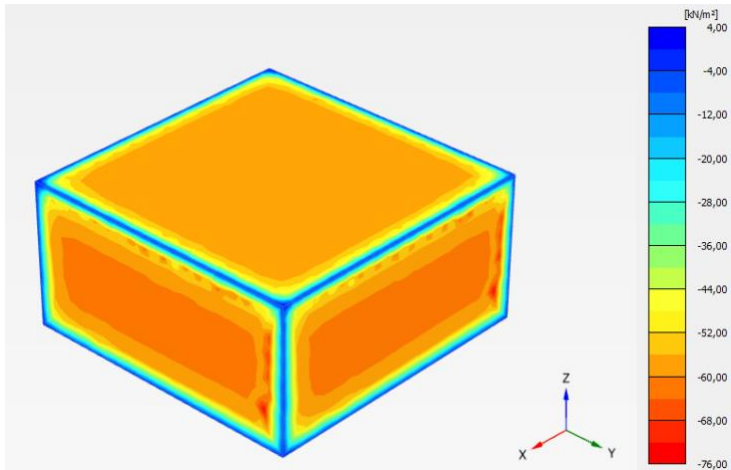


Figure 64: Excess pore pressure contour plot for biaxial loading in PLAXIS3D at  $t = 0.003 \text{ days}$ .

At the end of the phase the excess pore pressure increases to a maximum of  $-113.7 \text{ kPa}$ . The same distribution pattern of pore pressure is seen compared to contour plot for  $t = 0.003 \text{ days}$ .

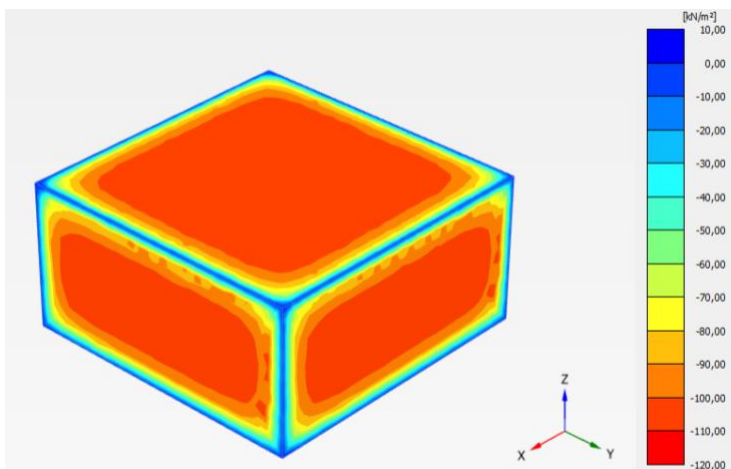


Figure 65: Excess pore pressure contour plot for biaxial loading in PLAXIS3D at  $t = 0.006 \text{ days}$ .

The meshes at  $t = 0.006 \text{ days}$  for effective stress,  $\sigma'_{xx}$ ,  $\sigma'_{yy}$  and  $\sigma'_{zz}$ , respectively, are given below. According to this numerical analysis, the value of  $\sigma'_{xx}$  equals zero at the position of total stress measurement. The value of  $\sigma_{xx}$  measured at the sensor consists majorly of pore pressure. This in contrast to the analysis in PLAXIS2D where effective stresses are given at the position of total stress measurement.

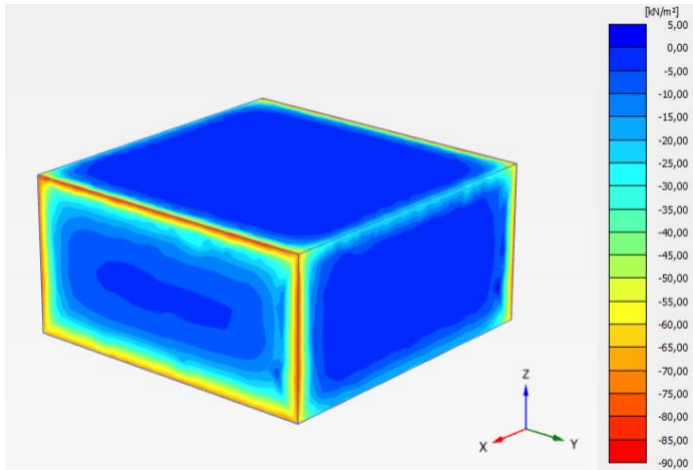


Figure 66:  $\sigma'_{xx}$  contour plot for biaxial loading of -0.1 mm at  $t = 0.006$  days in PLAXIS3D.

The same pattern is seen for the value of  $\sigma'_{yy}$ , which equals zero at the position of total stress measurement.

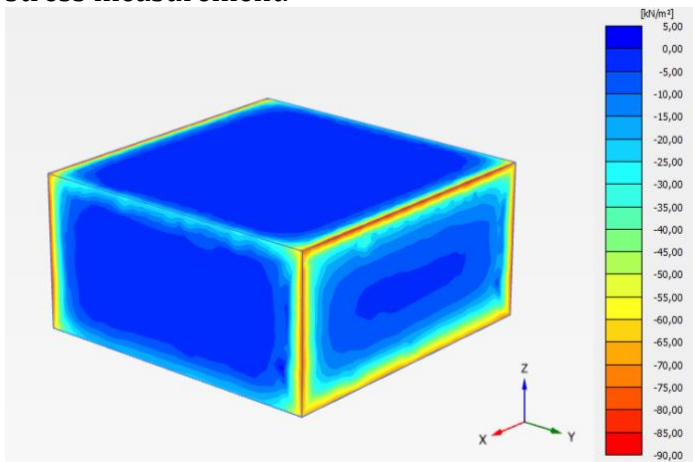


Figure 67:  $\sigma'_{yy}$  contour plot for biaxial loading of -0.1 mm at  $t = 0.006$  days in PLAXIS3D.

A bottom view of the mesh is given. It shows that the value of  $\sigma'_{zz}$  equals zero at the position of total stress measurement. Towards the gaps the value of  $\sigma'_{zz}$  increases. The highest values for effective stress are found near, but not exactly at the boundaries.

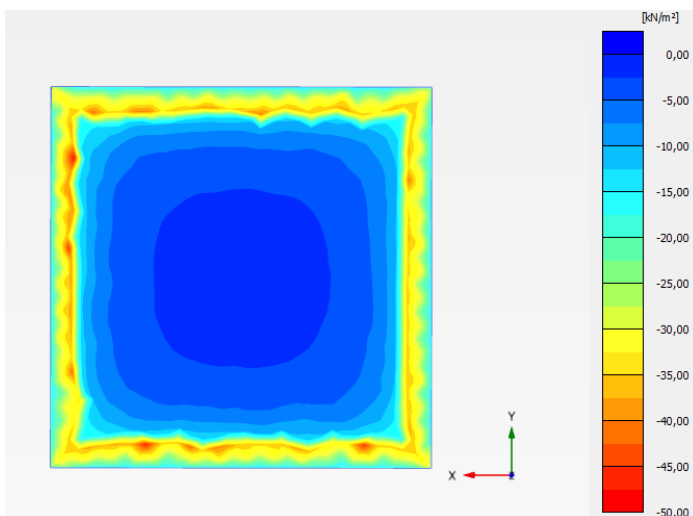


Figure 68:  $\sigma'_{zz}$  bottom view contour plot for biaxial loading of -0.1 mm at  $t = 0.006$  days in PLAXIS3D



### 4.4.3. Biaxial shearing

In biaxial shearing the sample is extended in one direction whilst in the other direction a compressional displacement is imposed. The following prescribed displacements are given in PLAXIS3D.

Table 14: Prescribed displacements for biaxial shearing in PLAXIS3D.

Phase	Line displacement side A [x,y,z]	Line displacement side B [x,y,z]	Line displacement side C [x,y,z]	Line displacement side D [x,y,z]	Line displacement side E [x,y,z]	Line displacement side F [x,y,z]	Time	Calculation type
Biaxial loading	[1 mm, free, fixed]	[free, 1 mm, fixed]	[-1 mm, free, fixed]	[free, -1 mm, fixed]	[free, free, fixed]	[free, free, fixed]	0.4	Consolidation

Displacements of  $-1\text{ mm}$  and  $1\text{ mm}$  are applied in y-direction and x-direction, respectively. This leads to compression in y-direction and extension in x-direction as shown by the deformed mesh in Figure 69.

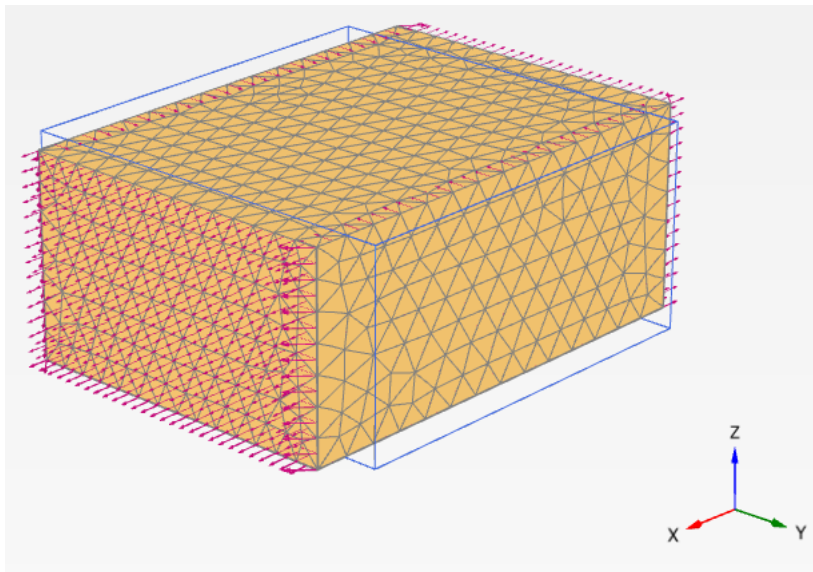


Figure 69: Deformed mesh for biaxial shearing PLAXIS3D.

# 5. Biaxial test results

In this chapter the biaxial test results are presented. They are analysed in Paragraph 5.1 and compared to the numerical simulation in PLAXIS in Paragraph 5.2. Hereafter, conclusions are given for the test results in Paragraph 5.3. Future tests are based on these conclusions.

## 5.1. Test results

The output obtained from the laboratory is discussed. Relevant tests are selected and presented in chronological order of testing.

### 5.1.1. Test 1

For test 1, T1, an OVP Clay sample is placed in the biaxial cell. This is shown below with the four vertical plates annotated with a letter. The laboratory set up is installed according to the design described by Appendix A.1. This implies drained conditions through the porous stone towards the water outlet.

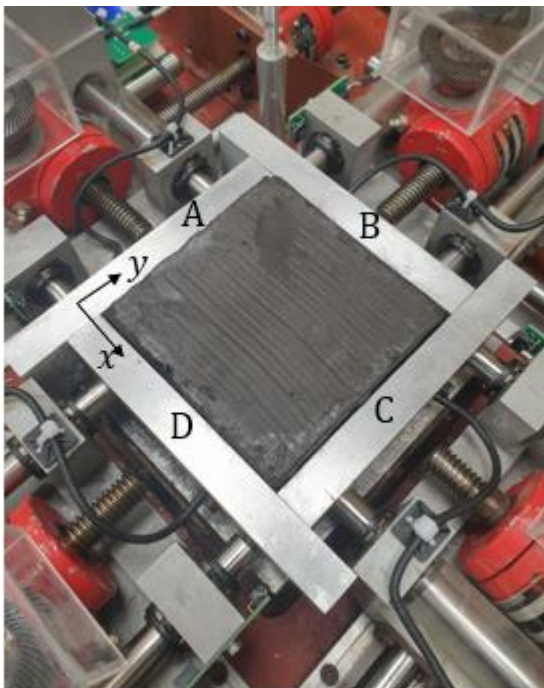


Figure 70: Placing of sample in biaxial cell for T1.

The test is characterized by two stages. First four phases of biaxial loading are altered by a phase of relaxation. Followed by a biaxial shearing phase. During the biaxial loading phases, a displacement of  $-0.1 \text{ mm}$  is applied to all four plates in x-direction and y-direction. This is done with the minimum displacement rate of  $0.00021 \frac{\text{mm}}{\text{s}}$ .

The test set up aims to preserve undrained conditions at the porous stone during biaxial shearing phase. This is done via the porous stone by closing the valves shown in Appendix A.1. The details of the phases for this test are shown in the table below.

Table 15: Details of phases for T1.

Phase	Phase type	$\Delta t$ [s]	$t_{begin}: t_{end}$	Displacement rate $\frac{[mm]}{s}$	Displacement [mm] Side A	Displacement [mm] Side B	Displacement [mm] Side C	Displacement [mm] Side D
1	Biaxial loading	476	0:476	-0.00021	-0.1	-0.1	-0.1	-0.1
2	Relaxation	994	476:1470	0	0	0	0	0
3	Biaxial loading	476	1470:1946	-0.00021	-0.1	-0.1	-0.1	-0.1
4	Relaxation	834	1946:2780	0	0	0	0	0
5	Biaxial loading	476	2780:3256	-0.00021	-0.1	-0.1	-0.1	-0.1
6	Relaxation	694	3256:3950	0	0	0	0	0
7	Biaxial loading	476	3950:4426	-0.00021	-0.1	-0.1	-0.1	-0.1
8	Relaxation	154	4426:4580	0	0	0	0	0
9	Biaxial loading	476	4580:5056	-0.00021	-0.1	-0.1	-0.1	-0.1
10	Relaxation	174	5056:5230	0	0	0	0	0
11	Biaxial loading	476	5230:5706	-0.00021	-0.1	-0.1	-0.1	-0.1
12	Relaxation	34	5706:5740	0	0	0	0	0
13	Biaxial shearing	4590	5740:10330	-0.00021	-1	1	-1	1
14	Relaxation	300	10330:10600	0	0	0	0	0

The measurements for total stress and excess pore pressure are shown below. Also, the relative displacements are given for the metal plates corresponding to the y-axis to the right of the graph.

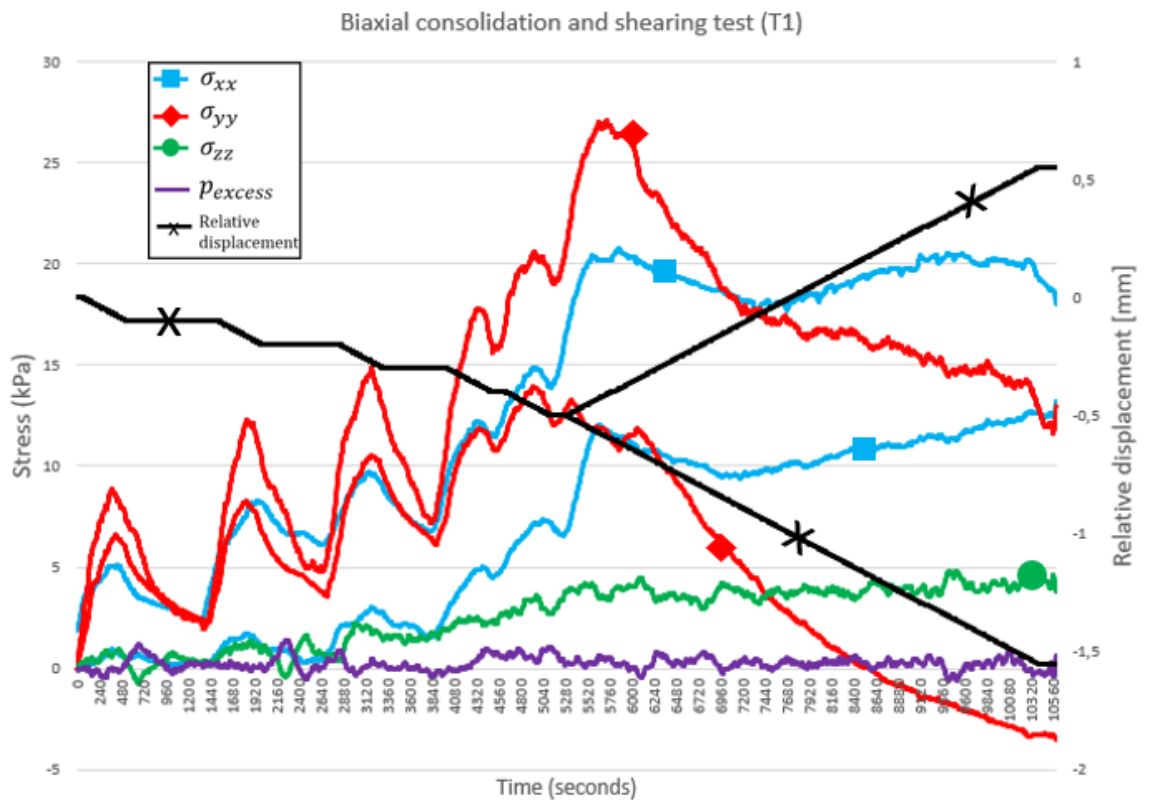


Figure 71: Time versus total stress and pore pressure, and time versus relative displacement for T1.

The stresses shown above are calibrated to start at zero. For the biaxial loading phase, measurement for opposing plate, acting in the same stress direction, should give identical measurements of stress. The stress measurements for x-direction do not show symmetrical stress increase for the opposing plates. The stress in y-direction shows more symmetrical behaviour for the opposing plates. The total stress in z-direction shows a weak and more distorted response compared to the total stresses in x- and y-direction measured during the test.

Values of  $\sigma_{yy}$  increase by approximately 10 kPa due to a single biaxial loading phase of 0.1 mm.  $\sigma_{xx}$  increases by 5 kPa during a phase of biaxial loading. The total stresses  $\sigma_{xx}$  and  $\sigma_{yy}$  decrease once a relaxation phase is executed. This is done by letting all boundary plates stationary. The total stress for one plate in x-direction record significantly lower total stresses compared to its opposing plate.

The biaxial loading phase is followed by biaxial shearing, in which an increase in  $\sigma_{xx}$  and a decrease in  $\sigma_{yy}$  are applied. The stress in z-direction does not change during the shearing phase. No significant changes are seen for the excess pore pressure during the entire test. Also, no water is seen flowing towards the water outlet.

### 5.1.2. Test 2

There were two points of concern related to the results T1. First, the excess pore pressure measured showed no signs of response. Secondly, the behaviour of  $\sigma_{zz}$  did not correspond to the expectation based on the numerical analysis. The goal for test 2, T2 was to find more reliable measurements for these two quantities.

Before this test the saturation of the pore pressure system was verified using the procedure described in Paragraph 2.7.2. The pore pressure measurement gave the desired increased response for an increase in water column. The water pressure measurement set up, described in Appendix A.3, is used for this test.

A 10 cm by 10 cm sample was trimmed using a metal casing of these dimensions. Hereafter, the excess height was cut off to match the dimensions of the biaxial cell, as shown below.



*Figure 72: Trimming of OVP clay used for T2.*

The sample was covered in latex, which is expected to decrease the pathways for excess pore pressure to drain out of the sample. At the bottom of the sample a cut was made through the latex at the position of the porous stone. The porous stone was mounted at 2 mm more elevation above the bottom plate. This resulted in the porous stone being slightly pressed into the sample. These measures were taken to improve contact between the sample and the porous stone.





Figure 73: Bottom side of OVP Clay sample covered in latex for T2.

The sample with latex is placed on top of the vertical plate towards the corner with the porous stone. To do this, the sample was laid gradually onto the bottom plate allowing air to escape between the bottom of the sample and the bottom plate. The position of the porous stone with respect to the sample is represented by the red dashed circle in Figure 74. The referential letters for each side are shown in the image. Contact between the upper plate and the sample is made by placing the horizontal glass plate and tightening the screws.

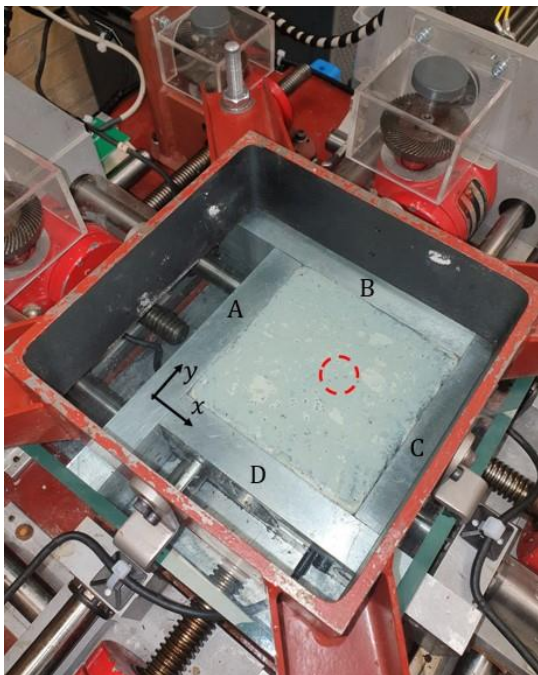


Figure 74: Placing of sample in biaxial cell for T2.

For the next step, contact is made between the sample and the vertical plates. The samples are cut of slightly asymmetrical due to imperfections in the sampling tools used. This requires differential displacement for the individual side platens during the contact procedure. This is done by moving all four vertical plates towards the sample with displacement rate of  $0.00021 \text{ mm/s}$ . Once contact is made between the sample and metal plates, total stresses increase, and displacement is stopped. Additional contact might

require individual vertical platens to be driven towards the sample leading to stress increase for that particular sample boundary. The sample is relaxed for approximately 30 minutes and the contact procedure is repeated. This is continued until all four vertical sensors show similar increase in total stress.

Once this is done, larger displacement steps are taken and the results, presented below, are documented. For this test several loading steps were taken, followed by a relaxation phase. The displacement for each side, with corresponding displacement rate, is given in the table below.

Table 16: Details of phases for T2.

Phase	Phase type	$\Delta t$ [s]	$t_{begin}: t_{end}$	Displacement rate $\frac{mm}{s}$	Displacement [mm] Side A	Displacement [mm] Side B	Displacement [mm] Side C	Displacement [mm] Side D
1	Biaxial loading	952	0:900	-0.00021	-0.2	0	0	-0.2
2	Relaxation	218	952:1170	0	0	0	0	0
3	Biaxial loading	952	1170:2122	-0.00021	-0.2	0	0	-0.2
4	Relaxation	92	2122:2214	0	0	0	0	0
5	Biaxial loading	952	2214:3166	-0.00021	-0.2	0	0	-0.2
6	Relaxation	100	3166:3266	0	0	0	0	0
7	Biaxial loading	247	3266:3513	-0.00084	-0.2	0	0	-0.2
8	Relaxation	493	3597:4090	0	0	0	0	0
9	Biaxial loading	247	4090:4337	-0.00084	-0.2	0	0	-0.2
10	Relaxation	563	4337:4900	0	0	0	0	0
11	Biaxial loading	476	4900:5376	-0.00021	-0.1	-0.1	-0.1	-0.1
12	Relaxation	500	5376:5876	0	0	0	0	0
13	Biaxial loading	476	5876:6352	-0.00021	-0.1	-0.1	-0.1	-0.1
14	Relaxation	300	6352:6652	0	0	0	0	0
15	Biaxial loading	238	6652:6890	-0.00021	-0.05	-0.05	-0.05	-0.05
16	Unloading	60	6890:6950	0.02	1	1	1	1

The corresponding time versus stress plot is presented below. The total stresses correspond to the y-axis on the left and the relative displacement corresponds to the y-axis on the right. The stress values are calibrated at zero for  $t = 0$ . Two shaded red blocks cover the graph, representing the time frames chosen to be analysed individually.



In general, compressional displacement leads to an increase in total stress in all three directions. For step 1, with  $[t_{begin}; t_{end}] = [0; 900]$ , the total stress measurement shows some noise. A possible explanation is insufficient and/or heterogeneous contact at this stage of the test.

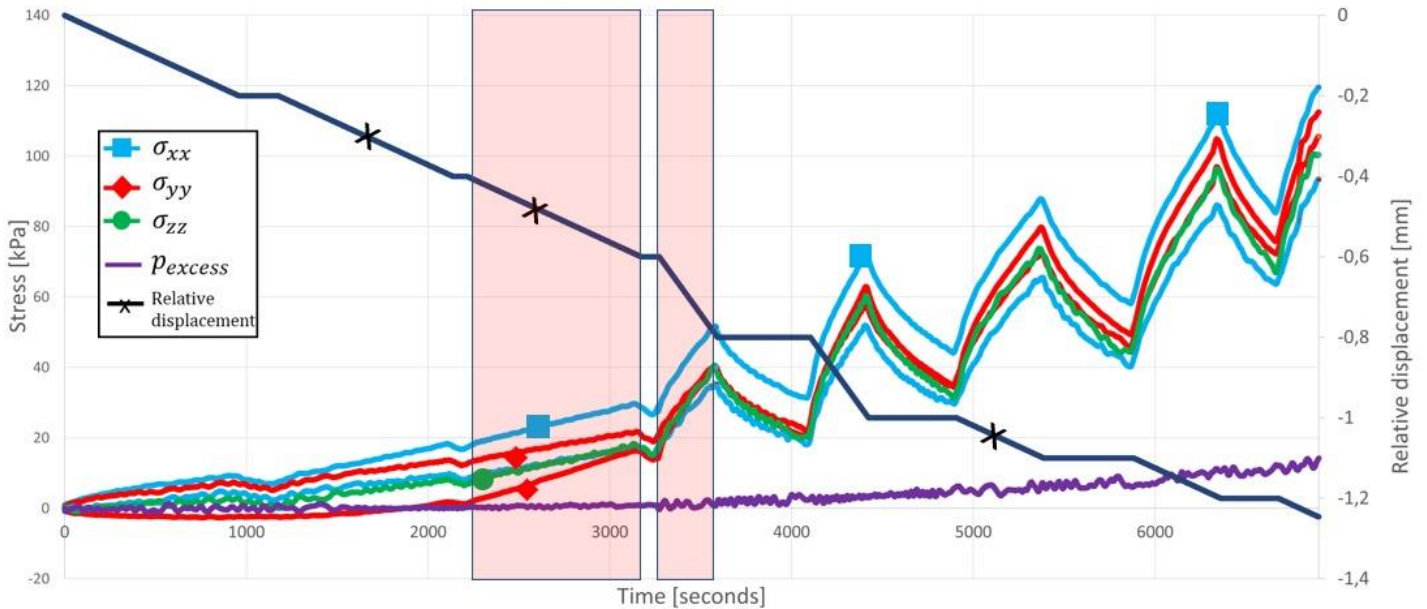


Figure 75: Time versus stress and time versus relative displacement for T2.

The output for the excess pore pressure is of particular interest due to the undesired results in previous tests. It is plotted below in Figure 76. There is some noise present, especially during phase 1 of the test. The pore pressure at the beginning of the test rests around 0 kPa. At the end of the test the excess pore pressure reaches a value of 14 kPa.

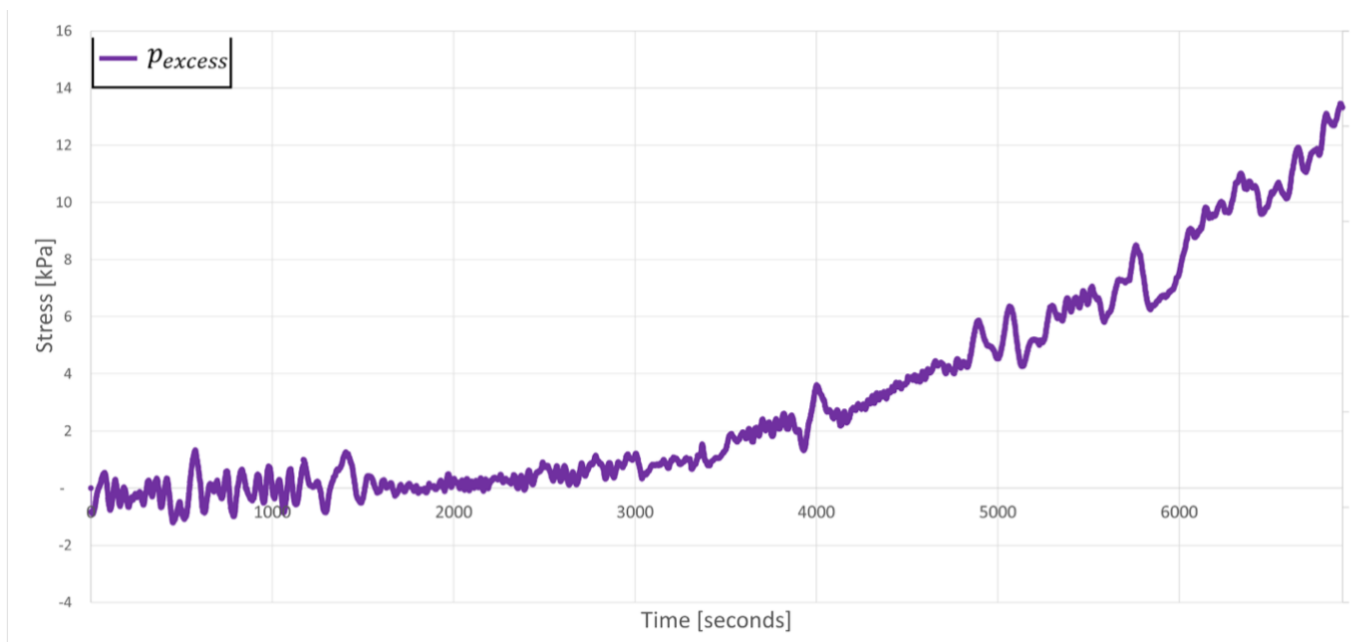


Figure 76: Excess pore pressure versus time for T2.

Phase 5 is plotted below and set at 0 kPa for  $t = 2214$  s. The values of stress are averaged over 4 seconds of measurement to reduce the noise seen in the curve. In this

step a displacement of  $-0,2$  mm is given on sides A and D with a displacement rate of  $-0.00021 \frac{mm}{s}$ . The total stresses increase from  $0$  kPa to values ranging between  $9$  kPa and  $15$  kPa. The total stress measured on the active plates, A and D, measure higher values of  $\sigma_{xx}$  and  $\sigma_{yy}$  compared to the stresses with same dimension on the opposing plates. No significant change in excess pore pressure is seen during this phase.

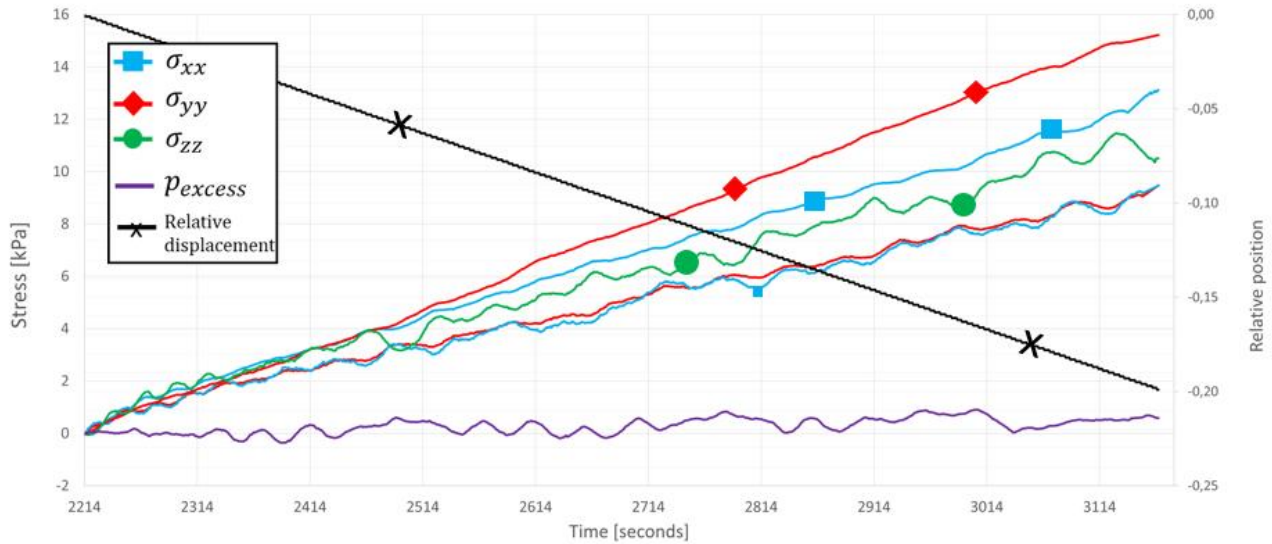


Figure 77: Time versus stress and time versus relative displacement for phase 5 of T2.

Next, phase 7 is given and set at  $0$  kPa for  $t = 3266$  s. Again, the values of stress are averaged over 4 seconds of measurement to reduce the noise seen in the curve. In this step a displacement of  $-0,2$  mm is given on sides A and D with a displacement rate of  $-0.00084 \frac{mm}{s}$ . The total stress increases by values between  $20$  kPa and  $25$  kPa during this step. For the active plates, the greatest change in total stress is recorded. Again, opposing plates differ approximately  $5$  kPa in total stresses also found in phase 5. No significant change in excess pore pressure is seen.

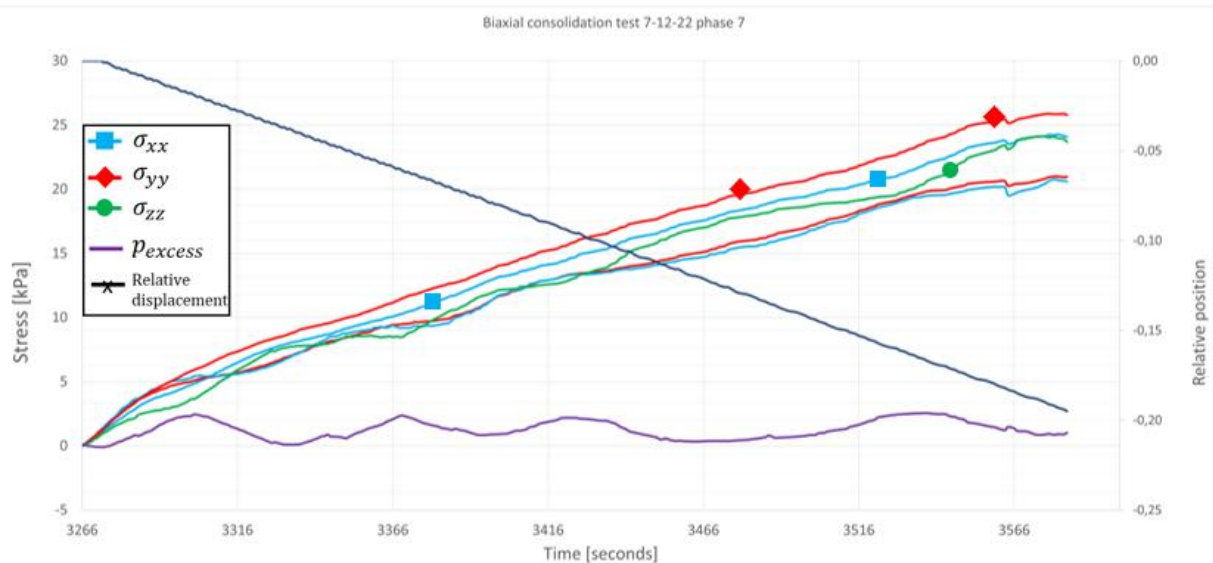


Figure 78: Time versus stress and time versus relative displacement for phase 7 of T2.

### 5.1.3. Test 3

Test 2 showed a more realistic increase in total stress in z-direction. The total stresses show a similar of change in stress. However, opposing plates show difference in total stress. Also, no significant increase in excess pore pressure is found.

Two measures are taken to find more realistic output. First, the displacement is given symmetrically for the opposing plates for all phases in the test. Secondly, refinements are made for the test procedure including the pore pressure measurement. The porous stone surface is mounted 3 mm above the bottom plate, 1 mm more compared to T2. The sample is trimmed of 3 mm greater than the height of the biaxial cell, giving 5.03 cm as z-dimension for the clay sample.

The sample is placed into the biaxial cell and the side plates are placed around the sample just ensuring no contact. The top plate is then placed and firmly connected. This ensures contact between the sample and the bottom plate. With intention to decrease the void space at the boundary of the sample and the bottom plate. This reduces the pathways for water to flow out of the sample.

A sketch illustrating the bottom plate – sample contact for T2 is given below in Figure 79.



Figure 79: Side view biaxial cell with contact sample and bottom plate discontinued by air voids.

A sketch of the sample being pressed down onto the bottom plate is given below. In comparison to Figure 79, the air void volume is expected to decrease due to a new test procedure, as shown below.

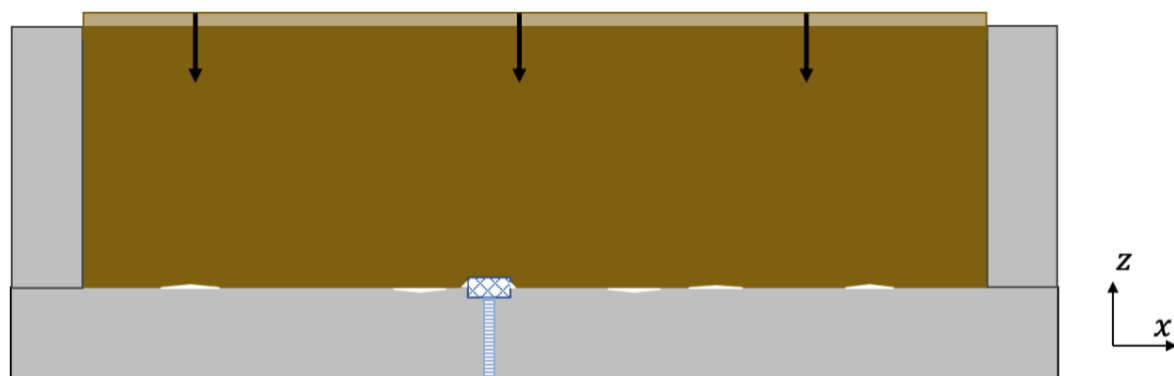


Figure 80: Side view biaxial cell with contact sample and bottom plate. Representation of pressing of the sample onto the bottom plate with reduced air voids for T3.

The sample, shown below, is squeezed in vertical direction, and slightly pressed out of the biaxial cell between the upper plate and the horizontal plates.

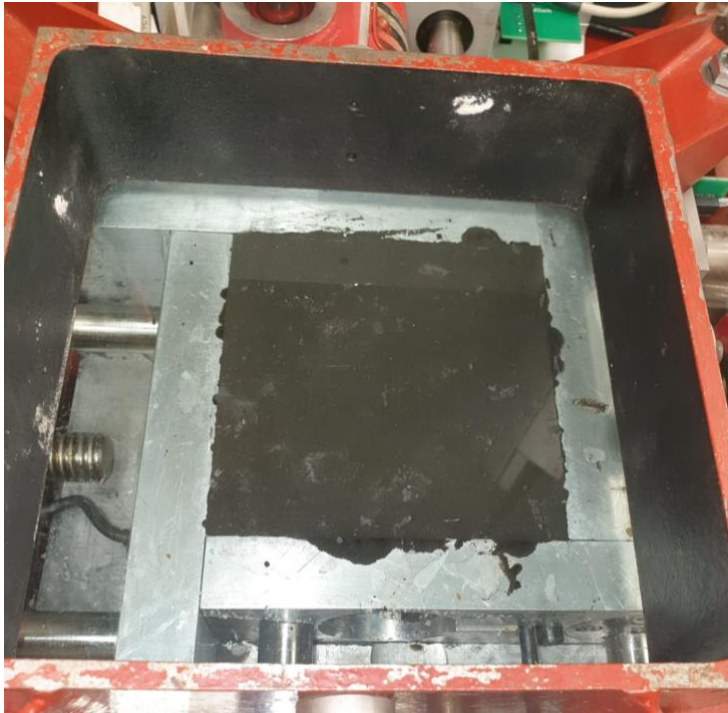


Figure 81: Sample enclosed by the biaxial cell during T3.

The phases with details for T3 are given below. Biaxial loading phases are performed followed by a relaxation phase. The displacement on all four sides is equal for all phases.

Table 17: Details of phases for T3.

Phase	Phase type	$\Delta t$ [s]	$t_{begin}:t_{end}$	Displacement rate $\frac{mm}{s}$	Displacement [mm] Side A	Displacement [mm] Side B	Displacement [mm] Side C	Displacement [mm] Side D
1	Biaxial loading	172	0:172	-0.00021	-0.037	-0.037	-0.037	-0.037
2	Relaxation	403	172:575	0	0	0	0	0
3	Biaxial loading	131	575:706	-0.00021	-0.028	-0.028	-0.028	-0.028
4	Relaxation	887	706:1593	0	0	0	0	0
5	Biaxial loading	476	1593:2069	-0.00021	-0.1	-0.1	-0.1	-0.1
6	Relaxation	817	2069:2886	0	0	0	0	0
7	Biaxial loading	476	2886:3362	-0.00021	-0.1	-0.1	-0.1	-0.1
8	Relaxation	1418	3362:4780	0	0	0	0	0

9	Biaxial loading	476	4780:5256	-0.00021	-0.1	-0.1	-0.1	-0.1
10	Relaxation	744	5256:6000	0	0	0	0	0
11	Biaxial loading	419	6000:6419	-0.00021	-0.088	-0.088	-0.088	-0.088
12	Relaxation	572	6419:6991	0	0	0	0	0
13	Biaxial shearing	976	6991:7967	-0.00021	0.205	-0.205	0.205	-0.205

Before these phases were executed there was an increase in total stress as the sample was compressed. The dimension of the sample in z-direction exceeded the height of the biaxial cell. This showed an increase of approximately 30 kPa in all three dimensions whilst enclosing the sample between the six plates. The time versus stress plot is shown below. It also includes the relative displacement marked by the axes on the right-hand side. The recorded values of stress are calibrated to start at 0 at the beginning of phase 1.

The rate of volumetric strain for T3 is higher than that of T2. This is because all four plates are displaced at once with the minimum displacement rate of 0.00021 mm/s, instead of two out of four plates for T2. This gives a stiffer response of the clay and greater increase of total stress for all three dimensions. The excess pore pressure shows response ranging from 0 to 20 kPa.

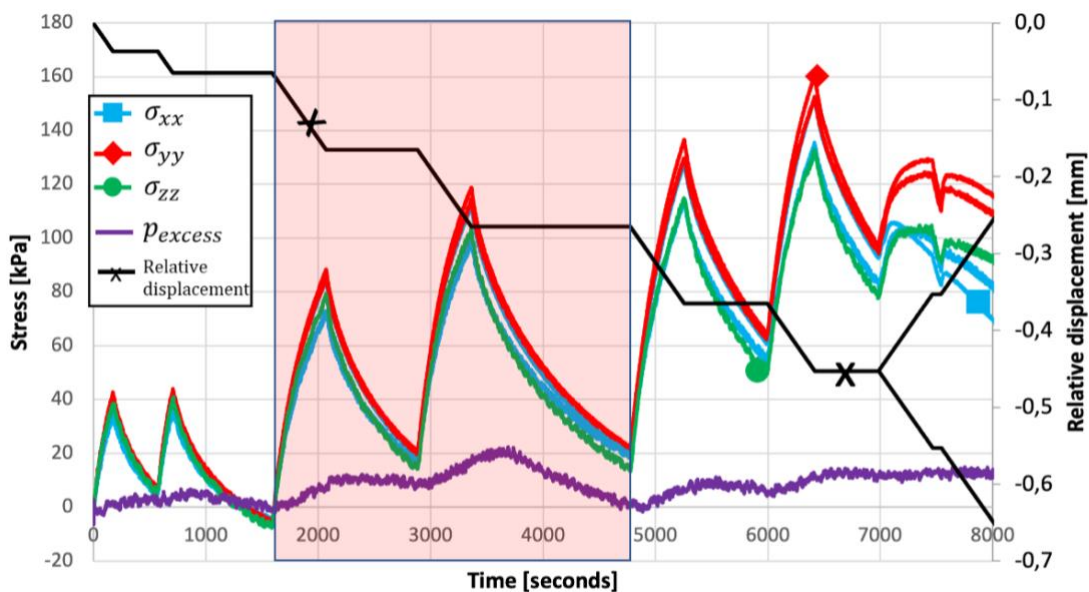


Figure 82: Time versus stress and time versus relative displacement for T3.

Phases 5 to 8, shaded in the figure above, are represented in the plot below. The total stresses in y-direction show similar response. The difference in total stress for the x-direction differs more. The excess pore pressure show response related to the phases of biaxial loading and relaxation. For compressional displacement, and increase in total stresses, the pore pressure increases. During relaxation there is a decrease in total stresses and a decreasing trend is seen for the excess pore pressure.



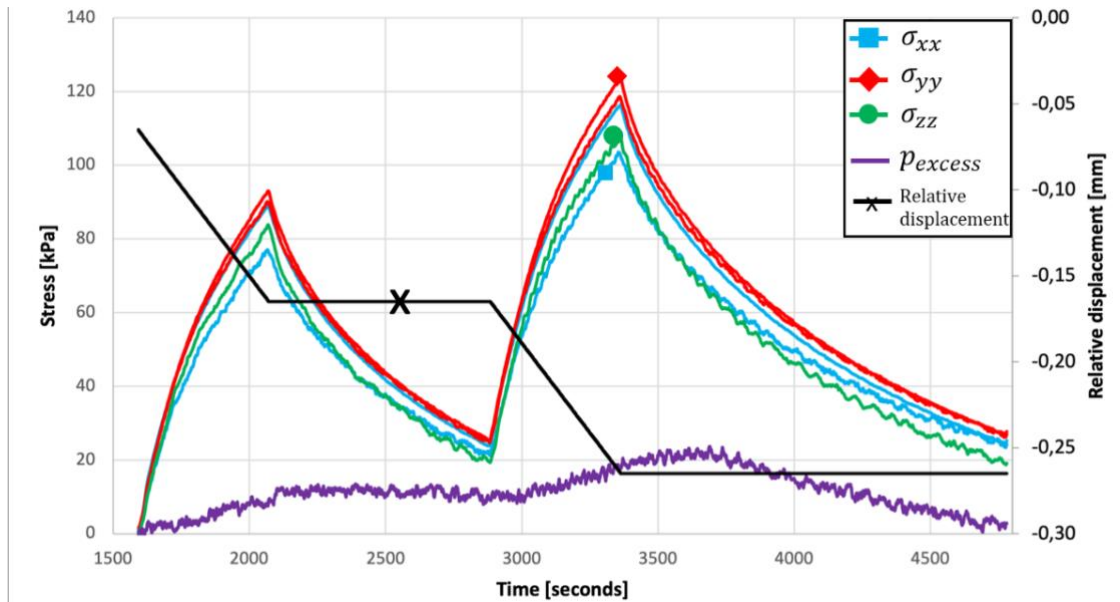


Figure 83: Time versus stress and time versus relative displacement, phases 5 to 8 for T3.

The measured values of total stress and excess pore pressure are given at the end of each phase. The four stresses corresponding to sides A, B, C and D are distinguished. In brackets their axial direction with annotation. The stress in z-direction and the excess pore pressure measured at the bottom plate are given as well.

Table 18: Measured stress values at the end of phases 5 to 8 for T3.

Phase	Side A (sensor x1)	Side B (sensor y1)	Side C (sensor x2)	Side D (sensor y2)	Bottom plate (sensor z)	Excess pore pressure
Unit	Stress [kPa]	Stress [kPa]	Stress [kPa]	Stress [kPa]	Stress [kPa]	Pore pressure [kPa]
Start	0	0	0	0	0	0
5	89.0	90.0	76.8	93.0	83.8	7.9
6	24.5	25.6	22.5	26.0	19.7	8.9
7	116.3	118.4	102.8	123.5	107.9	18.1
8	25.3	27.0	24.3	27.7	19.1	2.8

#### 5.1.4. Test 4

The excess pore pressure measured for T3 gave a signal showing correspondence to the numerical analysis. A downside of the procedure for T3 was that the sample was forced onto the bottom plate. Test 4, T4, indented on a refined contact procedure between sample and biaxial cell yet obtaining realistic values for excess pore pressure. Also, this refined contact procedure had as goal to obtain less stiff behaviour of the clay compared to T3.

To reach this goal further steps were taken to ensure homogeneous contact between plates and sample, decreasing the presence of air voids. For T4, the sample was trimmed of with a 1 mm greater dimension in the direction of z with respect to the

biaxial cell volume. The plates are driven with a displacement rate of  $0.00021 \text{ mm/s}$  towards the sample. Once contact is made, and the total stresses start to increase, the motors are stopped immediately. Following this contact, several phases of biaxial loading are executed, compressing the sample on all four sides with a displacement rate of  $0.00021 \text{ mm/s}$ . For an incremental increase of  $10 \text{ kPa}$  the displacement is stopped manually, and the sample is relaxed for 30 minutes. Eventually the sample makes homogeneous contact on all visible sides and edges as shown in the figure below. The sample is then relaxed for 12 hours.

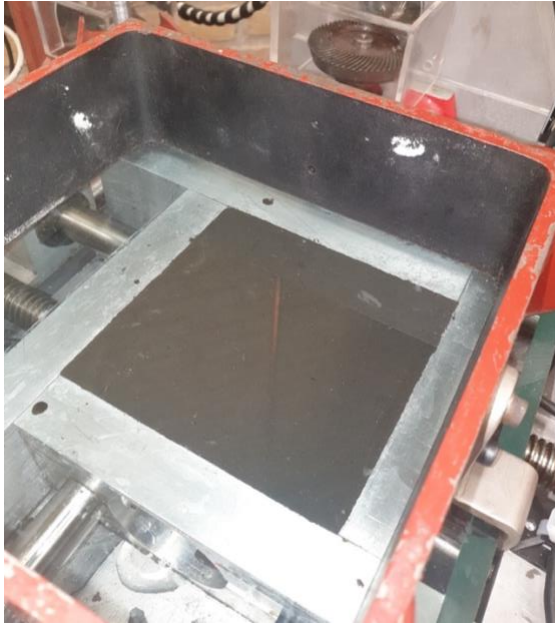


Figure 84: Top view of sample enclosed by biaxial cell after refined contact procedure.

After this 12-hour relaxation phase, six phases of alternately biaxial loading and relaxation are performed. The details of these six phases are given in the table below.

Table 19: Details of phases for T4.

Phase	Phase type	$\Delta t$ [s]	$t_{begin}: t_{end}$	Displacement rate $\left[\frac{\text{mm}}{\text{s}}\right]$	Displacement [mm] Side A	Displacement [mm] Side B	Displacement [mm] Side C	Displacement [mm] Side D
1	Biaxial loading	421	0:421	-0.00021	-0.088	-0.088	-0.088	-0.088
2	Relaxation	840	421:1261	0	0	0	0	0
3	Biaxial loading	476	1261:1737	-0.00021	-0.1	-0.1	-0.1	-0.1
4	Relaxation	756	1738:2494	0	0	0	0	0
5	Biaxial loading	476	2494:2970	-0.00021	-0.1	-0.1	-0.1	-0.1
6	Relaxation	230	2970:3200	0	0	0	0	0



The time versus stress plot is shown below. The recorded values of stress are calibrated to start at 0 at the beginning of phase 1. The total stresses show a coinciding pattern. However, two of the five total stress values show a smaller trend in total stress development. During biaxial loading the values of total stress show a distorted signal, varying in a range of 5 kPa. During relaxation this distortion is not recorded.

The value for excess pore pressure increases during biaxial loading and decreases during relaxation. A delay is seen in the pore pressure pattern compared to the total stress development.

At  $t \approx 1261$  the values of total stress presented reach negative values of stress. Calibrating the stresses to zero will not account for the stresses gained during the contact procedure resulting in negative stresses during relaxation.

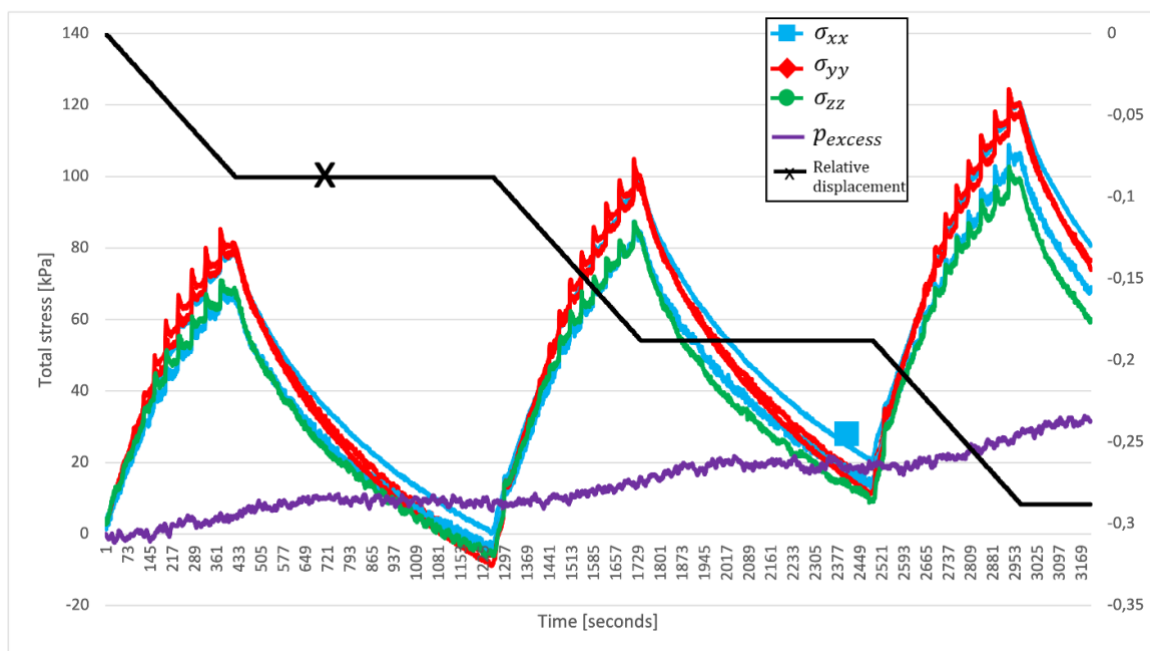


Figure 85: Time versus total stress and time versus relative displacement for T4.

The measured values of total stress and excess pore pressure are given in the table for the end of each phase. The total stresses relating to side C and the bottom plate show significantly smaller values of total stress. This is also seen for the measurements of total stress for T3. For this test, the stress measurements for these sensors were also lower compared to the stresses related to the other sensors.

Table 20: Measured stress values at the end of phases for T4.

Phase	Side A (sensor x1)	Side B (sensor y1)	Side C (sensor x2)	Side D (sensor y2)	Bottom plate (sensor z)	Excess pore pressure
Unit	Stress [kPa]	Stress [kPa]	Stress [kPa]	Stress [kPa]	Stress [kPa]	Pore pressure [kPa]
Start	0	0	0	0	0	0

1	77.7	78.2	65.8	80.2	67.3	5.0
2	2.5	-4.0	-2.3	-6.4	-5.0	9.1
3	97.2	96.0	83.0	98.5	82.4	15.5
4	22.8	16.2	15.5	14.1	10.7	19.4
5	119.1	116.2	104.6	118.9	97.9	28.2
6	80.8	76.5	68.2	74.3	59.5	31.6

At the end of T4, the OVP Clay sample is removed from the biaxial cell and shown below. At the boundaries of the clay slight damage can be seen. Due to instability of the clay the sample is not perfectly symmetric. This might cause distortion to the signal measured during the test.



Figure 86: OVP Clay sample at the end of T4.

### 5.1.4. Test 5

Excess pore pressure was measured in T3 and T4 using the design of Appendix A.3. A different design was installed introduced in Appendix A.5. A glass granule covered in tape is placed 2.5 cm into the biaxial cell. The glass granule is made up of very fine glass shards. A side and top view are shown below. Test 5, T5, is performed with this new design. The goal of this test is to obtain measurement of excess pore pressure. Preferentially showing rapid response at the start of a biaxial loading phase.



Figure 87: Side view (left) and top view (right) of glass granule placed in biaxial cell.

The average total stress and excess pore pressure are shown for T5. Alternating phases of biaxial loading and relaxation are performed during the test. This is done with the minimum displacement rate of  $0.00021 \text{ mm/s}$  and a symmetrical displacement for all four plates. The total stresses increase during biaxial loading and decrease during relaxation. The excess pore pressure increases over time up to a value of  $30 \text{ kPa}$ . No step response is seen for excess pore pressure during biaxial loading.

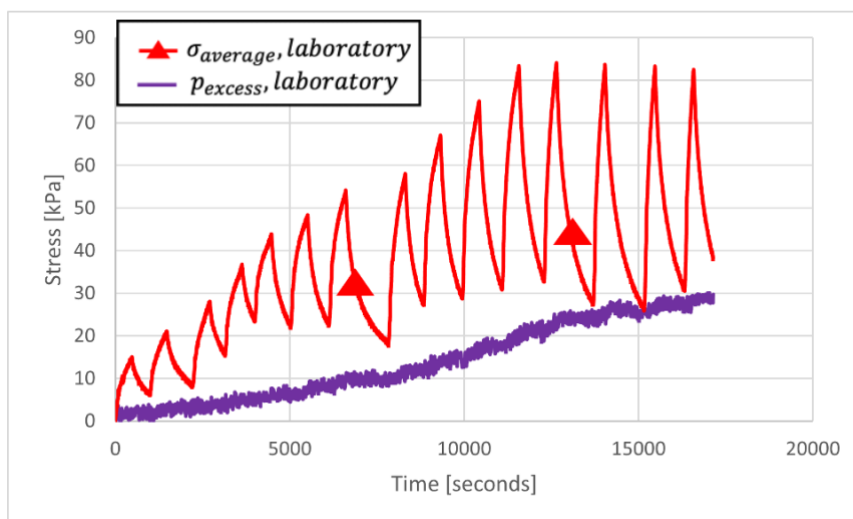


Figure 88: Time versus average total stress and excess pore pressure for T5.

## 5.2. Numerical simulation for laboratory tests

In this paragraph the tests which are performed in the laboratory are simulated PLAXIS2D and PLAXIS3D. These results from this numerical simulation aid in understanding the results found in the laboratory. For T1 and T2 PLAXIS2D is used as the numerical analysis in PLAXIS3D was not yet developed at the time of performance of these tests. For T3 and proceeding it is chosen to analyse the results using PLAXIS3D. To simplify comparing visualization between the laboratory test results and the numerical simulation the absolute values of stresses are presented in the time versus stress plots in the forthcoming paragraphs. The tests are simulated using the Soft Soil Creep model with input parameters introduced in Table 7.

### 5.2.1. Numerical analysis test 1

T1 consist of four biaxial loading phases altered relaxation phases. This is followed by a biaxial shearing phase.

Although drainage was intended via the porous stone this was not seen in practice. Therefore, it is chosen to set an undrained condition at the centre of the sample in this numerical analysis.

The test is simulated integrally starting with the four alternations of biaxial loading and relaxation. The biaxial loading stage have a displacement of  $-0.1\text{ mm}$  in x-direction and a displacement of  $-0.1\text{ mm}$  in y-direction. Hereafter, the sample is sheared by applying a compressional displacement of  $-1\text{ mm}$  in x-direction and an extension of  $1\text{ mm}$  in y-direction.

The total stress development over time is below. The mesh node for the total stresses is taken at the position of the related sensor. The total stresses for  $x$ ,  $y$  and  $z$  show similar behaviour during the phase of loading and relaxation. During the four stages of loading the total stress increases up to  $58\text{ kPa}$ . During biaxial shearing the total stresses decrease.  $\sigma_{xx}$ , corresponding to the active plate being the major stress,  $\sigma_{yy}$ , in the direction of the passive plate, the minor stress.

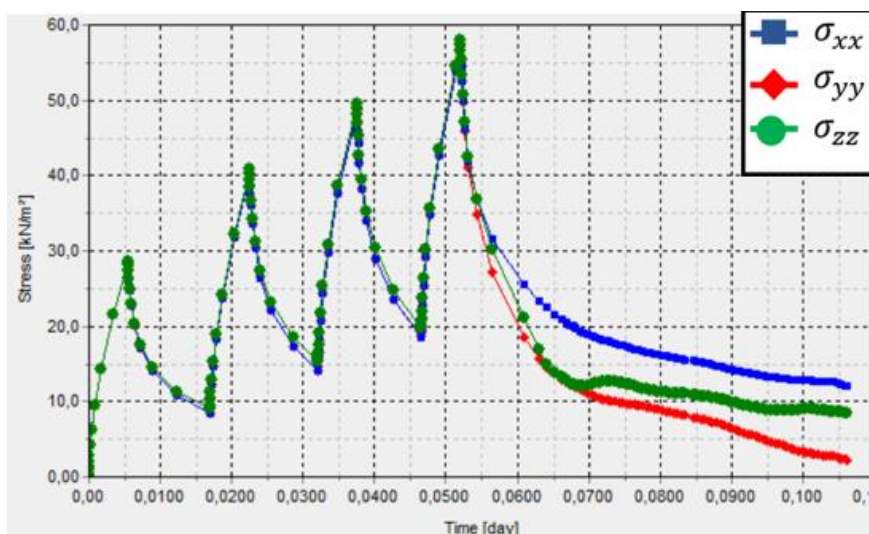


Figure 89: Total stress development for PLAXIS2D simulation T1.

### 5.2.2. Numerical analysis test 2

T2 is numerically analysed in this paragraph. It is chosen to analyse phase 5 and phase 7 individually as these were highlighted in the results chapter. The analysis is done in PLAXIS2D. During this test undrained conditions were intended. For a volume decrease the excess pore pressure is expected to increase. However, for T2 no significant excess pore pressure increase is measured in the laboratory. Also, water is seen seeping out at the border of the biaxial cell between the gaps of the plates. Therefore, the main objective is to understand the drainage behaviour in the sample as no excess pore pressure is measured.

For phase 5 the contour plot with prescribed displacements and corresponding displacement rate is illustrated below. The time span of this phase is matched accordingly to 0.012 *days*. In reality a displacement of -0.2 mm is given on two sides only. As a quarter of the sample is taken in the numerical simulation, this translates to -0.1 mm per side. This approach assumes a homogeneous sample with symmetrical behaviour. The time span of this phase is matched accordingly to 0.012 *days*. The mesh is allowed to drain on sides A and D, simulating leakage between these plates. At the centre, the porous stone maintains undrained conditions.

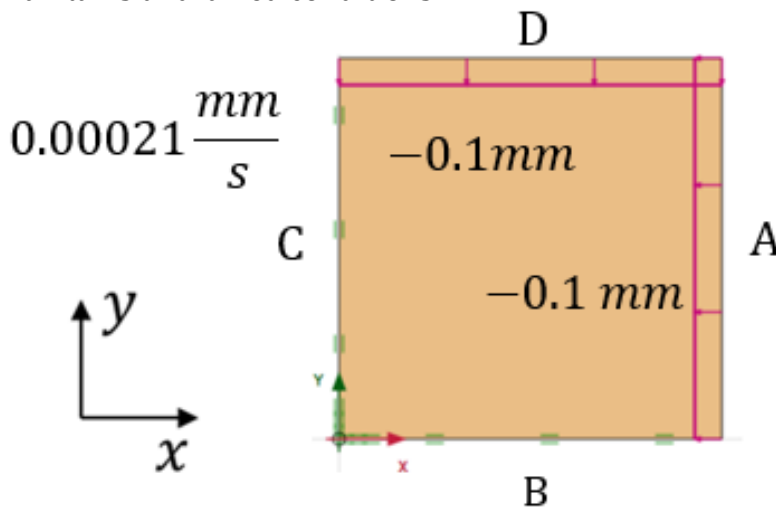


Figure 90: Prescribed displacements and displacement rate for phase 5 of T2.

Preceding phase 5, an initial stress is created,  $\sigma'_{xx} = -1.00 \text{ kPa}$ ,  $\sigma'_{yy} = -1.00 \text{ kPa}$  and  $\sigma'_{zz} = -1.00 \text{ kPa}$ . Next the quarter of sample is displaced in by  $-0.1 \text{ mm}$ . The development of the total stresses  $\sigma_{xx}$ ,  $\sigma_{yy}$  and  $\sigma_{zz}$  during this phase are given below. The total stresses increase identically up to  $-18.6 \text{ kPa}$  at the end of the phase at their position of measurement.

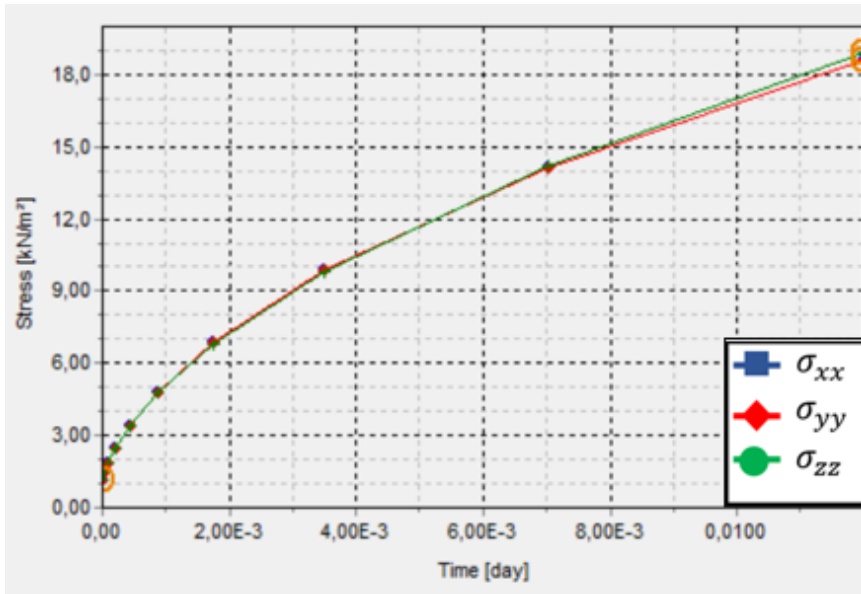


Figure 91: Total stress development for PLAXIS2D simulation T2 phase 5.

The excess pore pressure is shown, with the black circle indicating the position of the porous stone. On the boundaries of the sample the excess pore pressure equals 0 kPa. The pore pressure increases towards the centre of the sample with at maximum – 18.4 kPa.

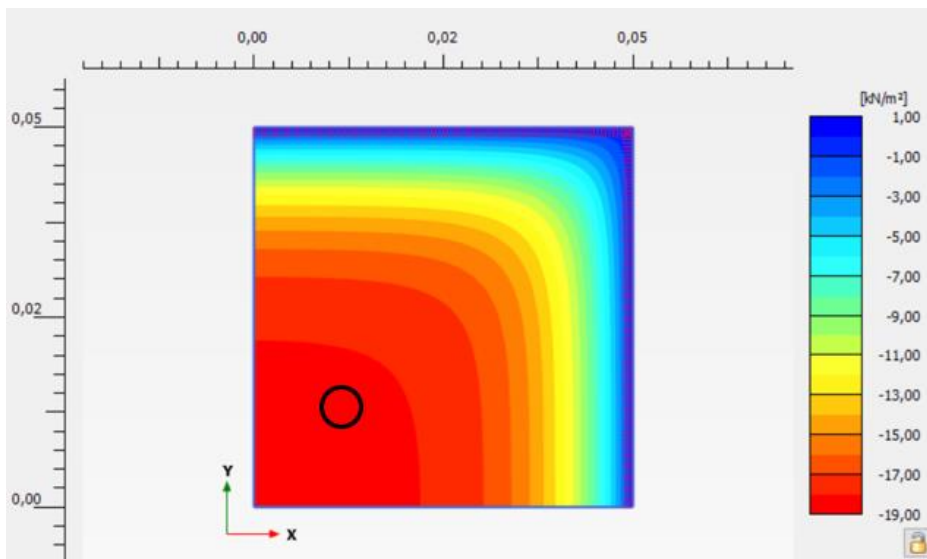


Figure 92: Contour plot of excess pore pressure for PLAXIS2D simulation T2 phase 5.

In the table below the value for total stresses and pore pressure are given for three moments during phase 5. They are given for the position of the sensor corresponding to the measured stress value.

Table 21: Stress values for numerical simulation phase 5 of T2.

Time in test [s]	$\sigma_{xx}$ [kPa]	$\sigma_{yy}$ [kPa]	$\sigma_{zz}$ [kPa]	$p_{excess}$ [kPa]
1170	-1.0	-1.0	-1.0	0
1646	-13.2	-13.2	-13.1	-12.9
2122	-19.1	-19.1	-18.9	-18.4



Next, for phase 7 the mesh with prescribed displacements and corresponding displacement rate illustrated below. The time of the phase is set accordingly to 0.0035 days.

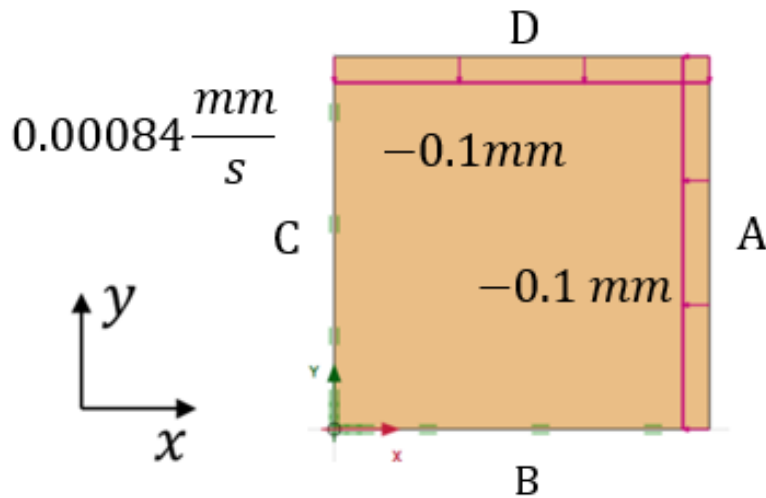


Figure 93: Prescribed displacements and displacement rate for phase 7 of T2.

The values of total stress and pore pressure throughout the mesh are higher due to the greater displacement rate. The excess pore pressure mesh at the end of the phase is shown below. The excess pore pressure increases with greater increment towards the centre of the sample compared to phase 5.

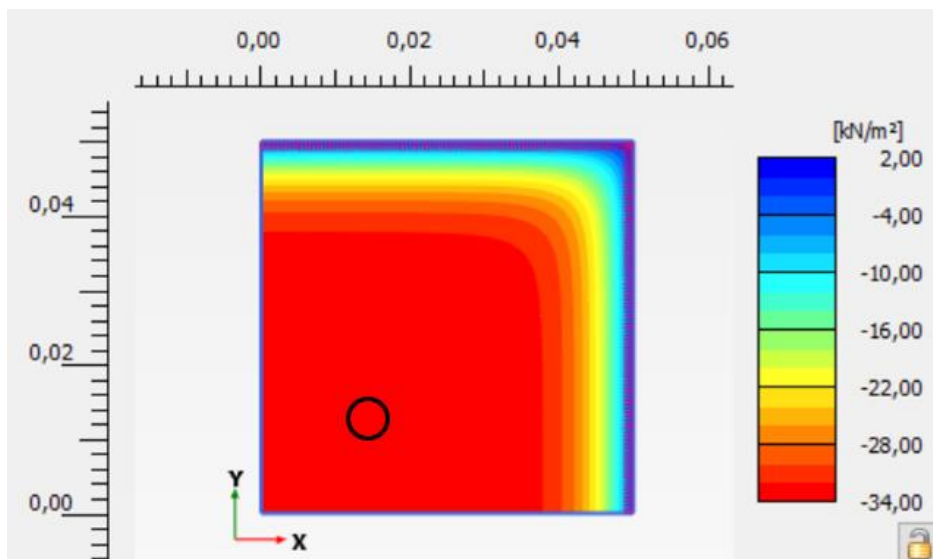


Figure 94: Mesh of excess pore pressure for PLAXIS2D simulation T2 phase 7.

In the table below the value for total stresses and pore pressure are given for three stages of phase 7.

Table 22: Stress values for numerical simulation phase 7 of T2.

Time in test [s]	$\sigma_{xx}$ [kPa]	$\sigma_{yy}$ [kPa]	$\sigma_{zz}$ [kPa]	$p_{excess}$ [kPa]
3266	-1.0	-1.0	-1.0	0
3389	-23.0	-23.0	-22.7	-21.7
3513	-35.4	-35.4	-35.0	-34.0



### 5.2.3. Numerical analysis test 3

Test 3 is numerically analysed in this paragraph using PLAXIS3D. It is chosen to analyse phase 5 to phase 8. The total stresses taken at the node of according to their measurement, increase simultaneously. For the first loading step an increase of 100 kPa is seen, after relaxation, the second biaxial loading step generates stiffer response.

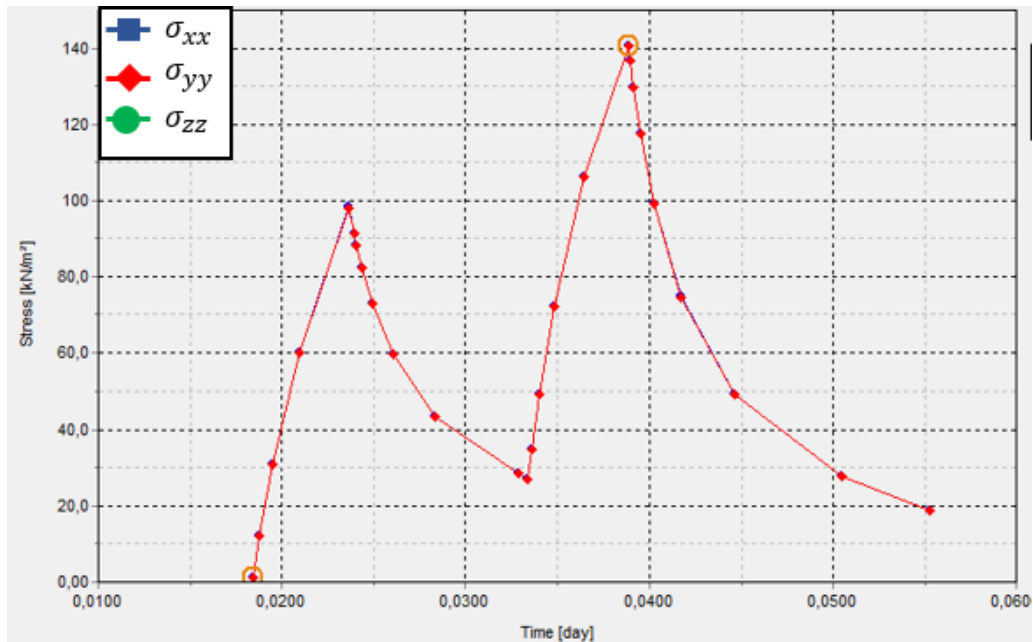


Figure 95: total stress development for PLAXIS3D simulation of T3.

A view of the bottom of the mesh, corresponding to the position of recording  $\sigma_{zz}$  and  $p_{excess}$  is shown below. It is given at the end of phase 7. The excess pore pressure reaches slightly lower values compared to  $\sigma_{zz}$ . According to the numerical analysis, the excess pore pressure has almost the same magnitude as the corresponding total stress increment.

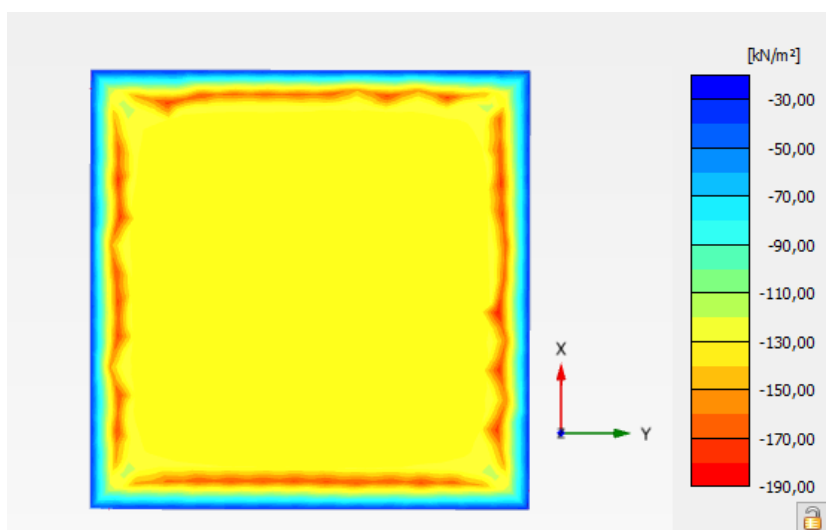


Figure 96: Bottom view total stress in z-direction for PLAXIS3D simulation of T3.

As the excess pore pressure almost has the same magnitude as the corresponding total stress increment, the excess pore pressure reaches slightly lower values compared to  $\sigma_{zz}$ .

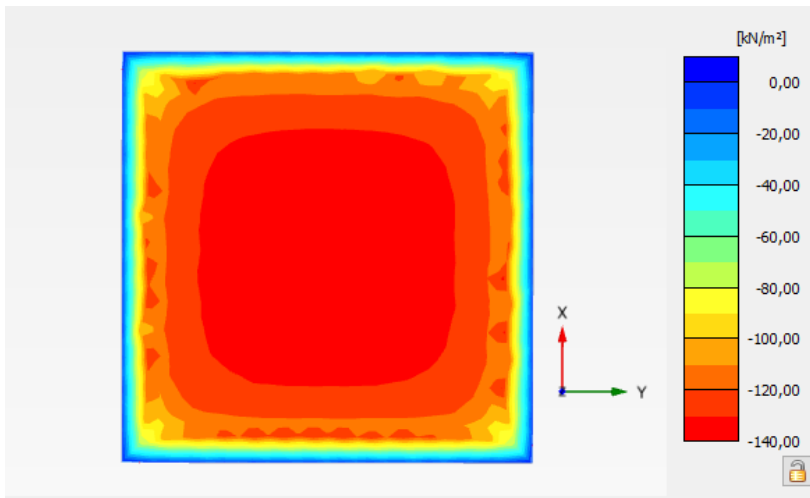


Figure 97: Bottom view excess pore pressure for PLAXIS3D simulation of T3.

The contour plot for effective stress in z-direction is given below. This gives high values of effective stress near the boundaries.

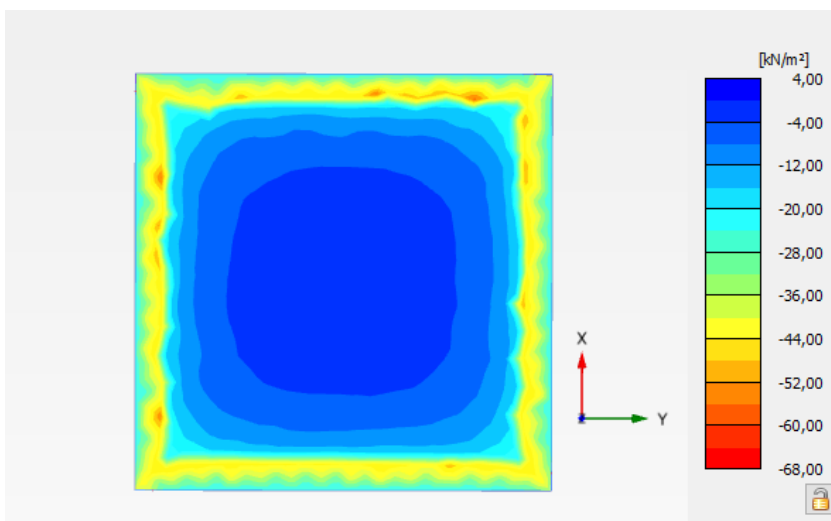


Figure 98: Bottom view effective stress in z-direction for PLAXIS3D simulation of T3.

#### 5.2.4. Numerical analysis test 4.

For the T4 the test is analysed in PLAXIS3D. The total stress plot is given below which shows the development of total stress  $\sigma_{xx}$ ,  $\sigma_{yy}$  and  $\sigma_{zz}$  during T4. They coincide and slight deviation might be to asymmetrical selection of the stress nodes in the mesh.

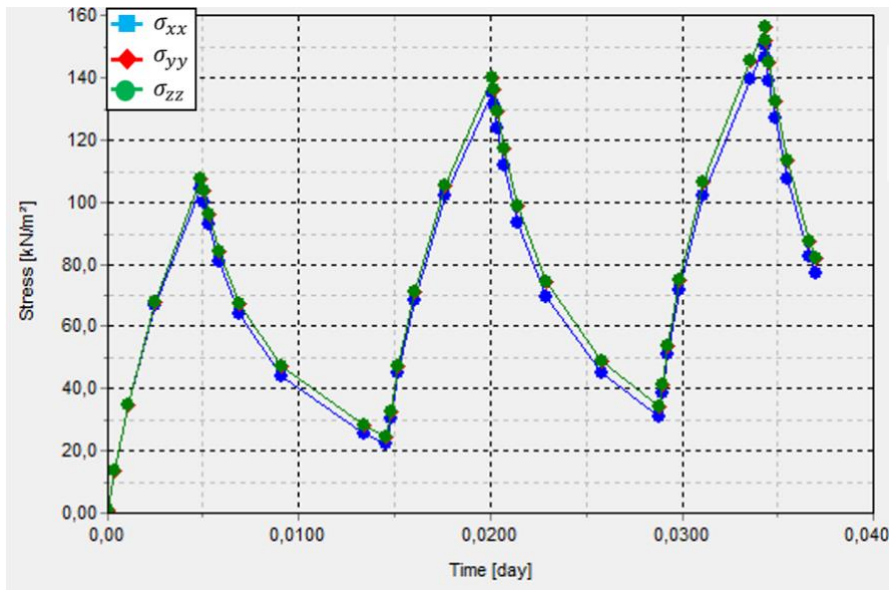


Figure 99: Total stress development for PLAXIS3D simulation of T4.

A bottom view for the excess pore pressure is given below for the end of phase 1. According to this numerical simulation an excess pore pressure of  $-115.3 \text{ kPa}$  should be found at the position of the porous stone.

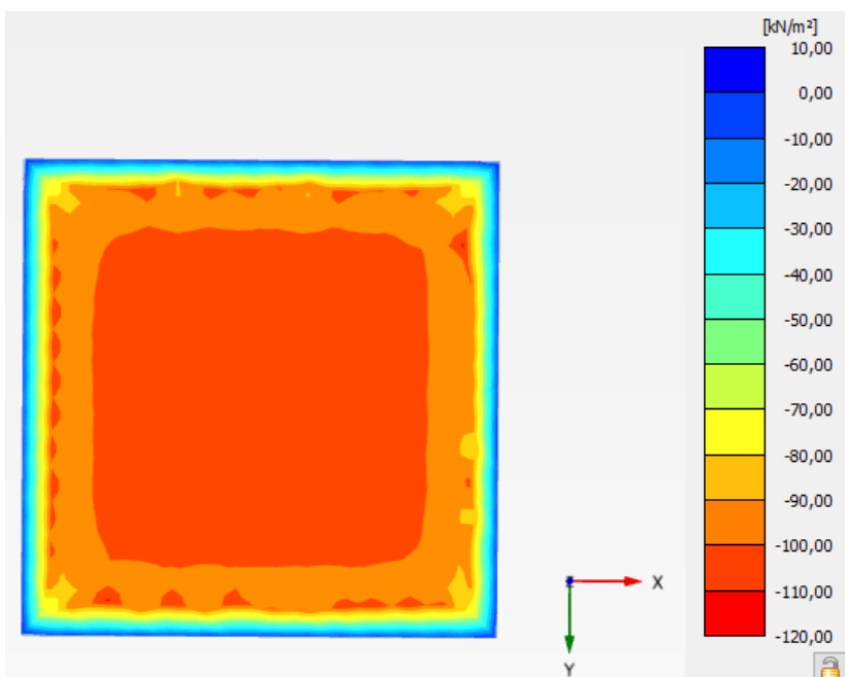


Figure 100: Bottom view of excess pore pressure at the end of phase 1 for PLAXIS3D simulation T4.

To evaluate the sensitivity of this finding, a PLAXIS3D simulation for T4 is made with a factor 5 greater hydraulic conductivity value,  $k = 2.42 \times 10^{-4} \text{ m/day}$ . A bottom view of the contour plot with excess pore pressures is shown below. Smaller values of excess pore pressure are reached compared to the lower hydraulic conductivity. A value of  $-39.1 \text{ kPa}$  is expected at the position of the porous stone at the end of phase 1.

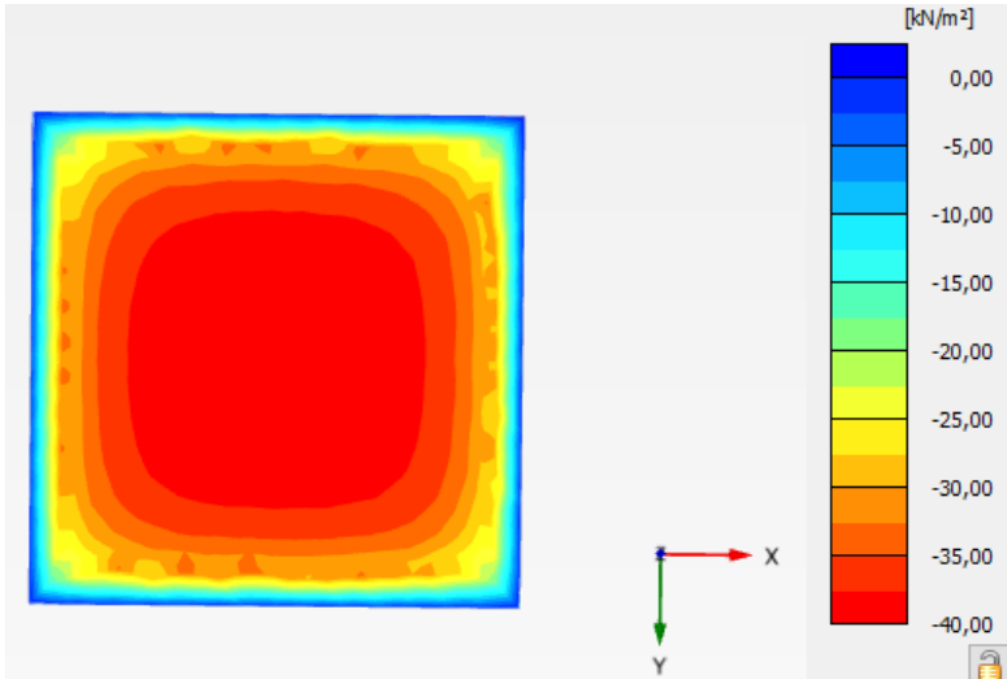


Figure 101: Bottom view of excess pore pressure at the end of phase 1 for PLAXIS3D simulation T4 with high hydraulic conductivity.

The excess pore pressures are plotted for both hydraulic conductivities for position of the porous stone. They show a similar pattern in excess pore pressure. A higher hydraulic conductivity leads to more dissipation of excess pore pressure through the gaps. This results in lower values of excess pore pressure for a higher hydraulic conductivity.

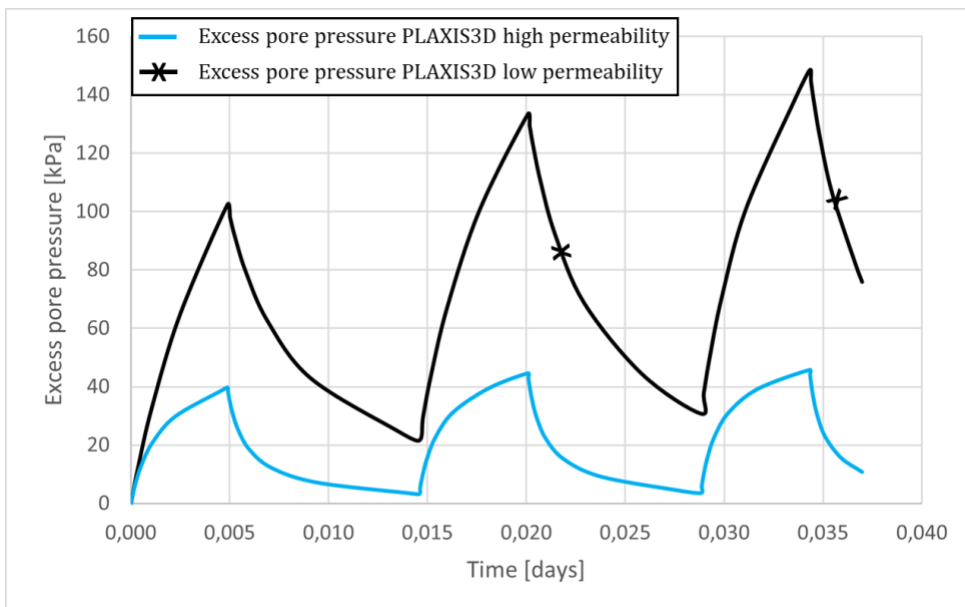


Figure 102: Excess pore pressure with high and low hydraulic conductivity for PLAXIS3D simulation T4.

### 5.3. Conclusions test results

The biaxial laboratory results are evaluated. This is done by analysing the output from the laboratory, comparing this output to the numerical analyses and by observations in the laboratory. This evaluation is used to set up new suitable laboratory tests and to verify the tests performed.

#### 5.3.1. Conclusion test 1

Based on the PLAXIS2D numerical analysis in Paragraph 5.2.1, the total stresses measured in the laboratory should have similar values during biaxial loading. This is not recorded during T1 as the total stresses do not coincide. Also, the values for total stress are lower than that of the numerical analysis.  $\sigma_{zz}$  deviates the most and shows a weak signal of increase during biaxial loading and decrease during relaxation compared to the signals of  $\sigma_{xx}$  and  $\sigma_{yy}$ . Ensuring better contact between the upper plate and sample could result in realistic measurement of  $\sigma_{zz}$ .

For a homogeneous sample the opposing plates are expected to have similar values of total stress. This was not seen, especially for the total stress measured for the opposing plates in the x-direction. Therefore, the contact between the plates and the sample should be made homogeneously at the start of the test.

The pore pressure shows no signs of increase from the laboratory measurement. This does not correspond to behaviour expected during biaxial loading seen in the numerical analysis. This indicates that the pore pressure measurement system should be improved. Also, no water is seen flowing through the tubes towards the water outlet. The design of Appendix A.1. is omitted.

#### 5.3.2. Conclusion test 2

For direction x- y and z- the value of total stress is expected to increase similarly based on the numerical analysis in PLAXIS2D. Phases 5 and 7 of laboratory T2 show differences of at maximum 6 kPa for the incremental total stress between the x- y and z-direction.

A larger displacement rate leads to a larger increase in total stresses for both laboratory and numerical analysis. The total stress increase from numerical analysis and laboratory for phases 5 and 7 are comparable. For phase 5 an increase of 15 kPa is observed with an increase of 19 kPa for the numerical analysis. For phase 7 an increase of 25 kPa is observed compared to the 35 kPa found for the numerical analysis.

As mentioned, total stresses measured for the opposing plates are expected to have similar values of total stress. For phase 5,  $\sigma_{xx}$  differentiates by 6 kPa for the measurement at opposing plates. A possible explanation is that for this phase two plates are displaced. Symmetrical displacement for opposing plates might reduce the effect of dissimilar values of total stress.

No excess pore pressure was measured in both phases 5 and 7. This does not coincide with the results from the numerical analysis in which a significant increase in excess pore

pressure is found for these phases. Towards the end of the test the excess pore pressure gives a general increasing trend. No match can be found between the start of a biaxial loading phase and an increase in excess pore pressure. In contrast to what is predicted by the numerical analysis in PLAXIS2D.

A possible explanation for the lack of pore pressure measurement is that there is not enough build-up of excess pore pressure near the porous stone. The porous stone sticks out by 2 mm and air voids could form around the cylinder around the porous stone whilst pressing into the clay. Enclosing the sample with latex increases the occurrence of air voids at contact between sample and bottom plate. Using latex might even oppose its indented effect of decreasing the preferential pathways for water.

Apart from the presentation of T3 other tests without latex were performed during this stage. Although the results are not presented in this thesis, the excess pore pressure measured showed similar output to that of T3. Another relevant factor is the preparation of the samples. They are not perfectly trimmed as the metal casing used might have become slightly asymmetrical. Also, The OVP Clay crumbles when preparing the sample before the laboratory test. This creates air voids in the biaxial cell and preferential pathways for the water. Scratches on the bottom plate due to extensive testing do not aid in this process. This leaves the water to follow the path out of the biaxial cell boundary via these air voids. This reasoning was illustrated in Figure 79 marking contact between sample and bottom plate. Air voids are shown by the white triangles at the porous stone and at contact between sample and the bottom plate. Refinements should be made for the pore pressure measurement to obtain more realistic output. The air voids in the biaxial cell should be decreased to a minimum, creating conditions for excess pore pressure build up.

Also, the total stresses measured in laboratory should coincide mutually according to the numerical analysis. It can be realised by changing the test procedure. A first theory is increasing the symmetry in contact made at the beginning of the test. The sampling mold is slightly asymmetric. To increase symmetry in contact, the plates should be driven individually towards the sample. This consumes multiple phases. Goal is to record equal cumulative total stress increment for all four x- and y- sensors during these contact drives. A second theory is that displacing opposite plates simultaneously will result in measurements of total stress agreeing more to one another.

### **5.3.3. Conclusion test 3**

In the z-dimension the sample was trimmed of slightly larger than the biaxial cell. Stiffer stress behaviour is expected due to the larger sample volume being confined. The average of the five measured total stresses from the laboratory and the PLAXIS3D analysis are plotted together below for phases 5 to 8. The total stress increments in the numerical analysis and in the laboratory coincide. The numerical simulation overestimates the increase in total stress compared to the laboratory. During relaxation, the numerical analysis shows greater decrease in total stress compared to the laboratory.

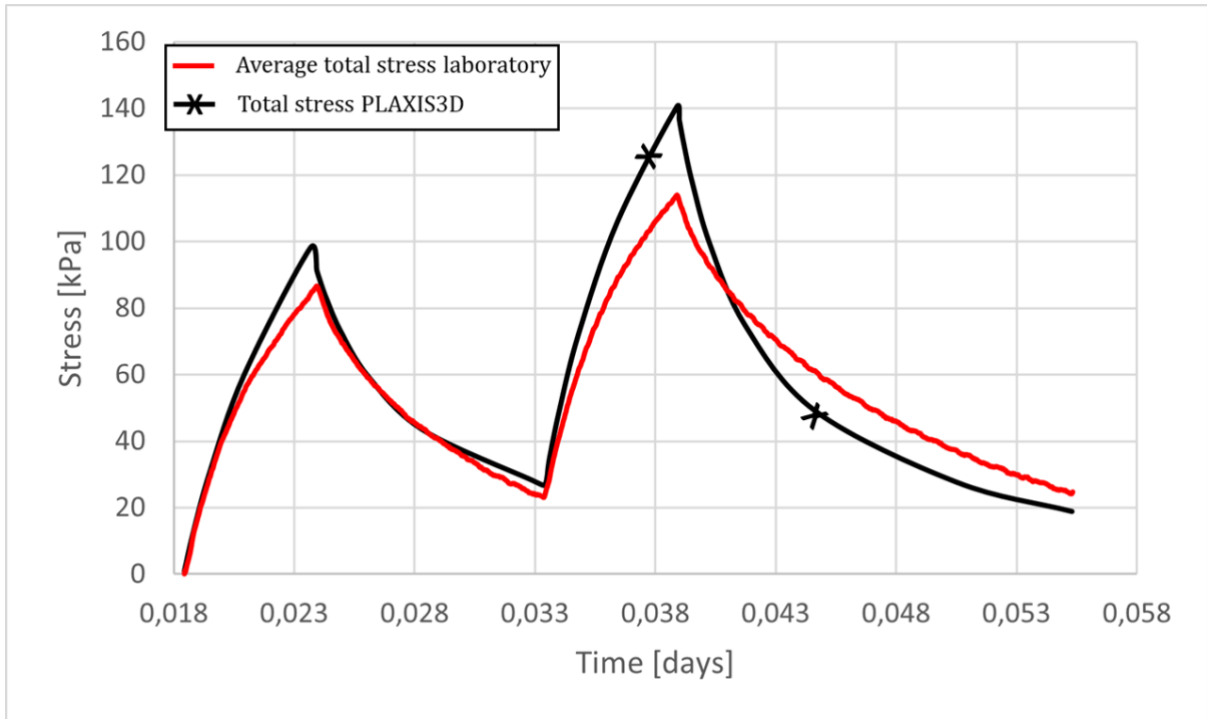


Figure 103: Time versus total stress from laboratory and PLAXIS3D for T3.

The recorded excess pore pressure shows correspondence to the displacements applied. During biaxial loading the excess pore pressure increases whilst it decreases during relaxation. The test procedure followed for T3 leads to a more realistic recording of the pore pressure.

In the plot below the pore pressure recorded is compared to the pore pressure expected from the numerical simulation. This is done for phases 5 to 8 of T3. The recorded pore pressure gives lower values but shows more correspondence to the numerical analysis than for previous tests.



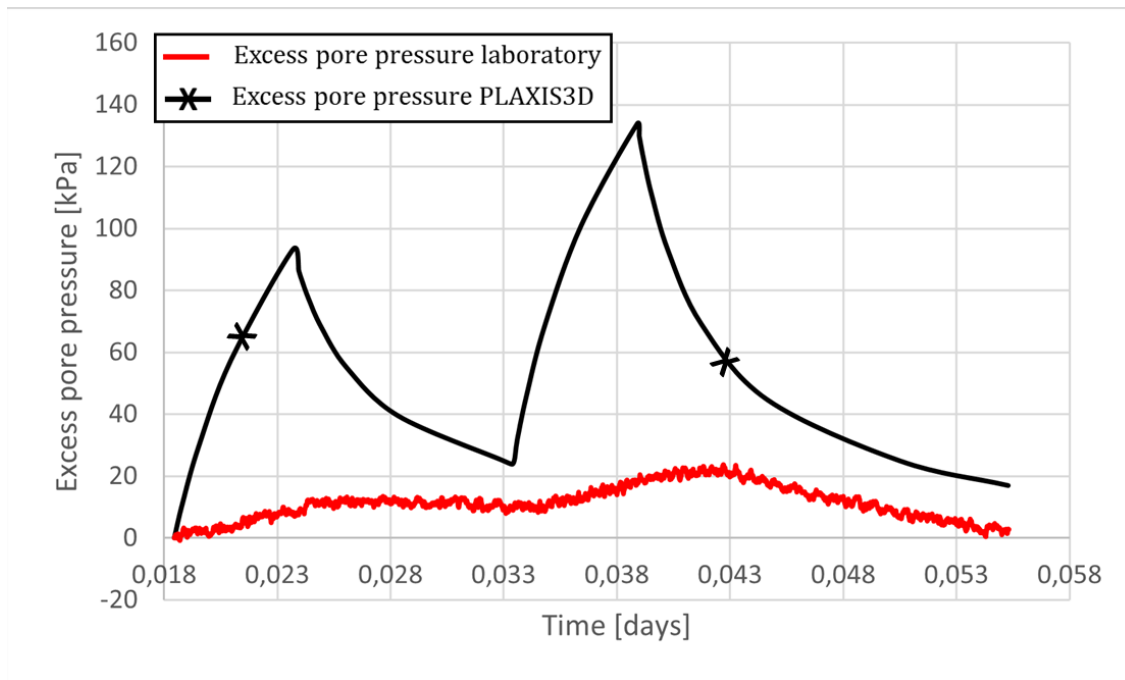


Figure 104: Comparison excess pore pressure in laboratory and PLAXIS3D.

In the table below the ratio of pore pressure with respect to the average total stress for the 5 sensors recorded is given. According to the numerical analysis the excess pore pressure at the end of the biaxial loading phase should be around 95% of the total stress value. The higher the ratio the more verifiable the result. For T3 percentages of 9.1% and 15.9% are found at the end of the biaxial loading phase.

Also given is the ratio of minor stress with respect to its opposing major stress in the same axial direction. According to the numerical analysis the values of total stress measured in the laboratory should be identical. The opposing total stresses measured in x-direction differ more as the stress for 'sensor x2' is, on average, 90.5% of 'sensor x1'. The sensors in y-direction correspond more with 'sensor y1' having a total stress value of 97% compared to 'sensor y2'.

The total stress sensor 'sensor x2' deviates from the other total stress sensors. The stress sensors in y-direction show more resemblance to one another. After this test, 'sensor x2' is calibrated again.

Table 23: Ratio of measurements for T3.

Phase	Ratio pore pressure of average total stress	Ratio minor and major total stress in x-direction	Ratio minor and major total stress in y-direction
Unit	Percentage [%]	Percentage [%]	Percentage [%]
Start	-	-	-
5	9.1	86.3	96.7
6	37.9	91.6	98.1
7	15.9	88.4	95.9
8	11.4	96.0	97.2

### 5.3.4 Conclusion test 4

The total stress development for T4 in PLAXIS3D was previously shown. The numerical simulation in PLAXIS2D and the average total stress measurement, consisting of all five total stress sensors in the laboratory, are added to the plot. The numerical simulation in PLAXIS2D underestimates the total stress development during the test. Also, the numerical simulation in PLAXIS2D gives smaller values of stress compared to the analysis in PLAXIS3D.

Numerically simulating the test for undrained conditions in PLAXIS2D and PLAXIS3D results in the same outcome. It is due to the difference in drainage boundaries for these two models that differences in stress occur. The model created in PLAXIS2D is set with drained conditions for the entire boundary between sample and vertical plates. The model created in PLAXIS3D re-creates the gaps between the plates. In this numerical model, only at the position of these gaps, drainage is allowed at the boundary between sample and biaxial cell. The other boundary areas are set to undrained conditions. This limits the area via which water can diffuse away from regions of high pressure. As a result, high pore pressures are generated in the three-dimensional model.

The total stress development in PLAXIS3D has a similar pattern compared to the laboratory total stress development. Smaller peaks of total stress are reached in the laboratory. This can be reasoned by the stress developed during the contact procedure prior to recording of the stresses.

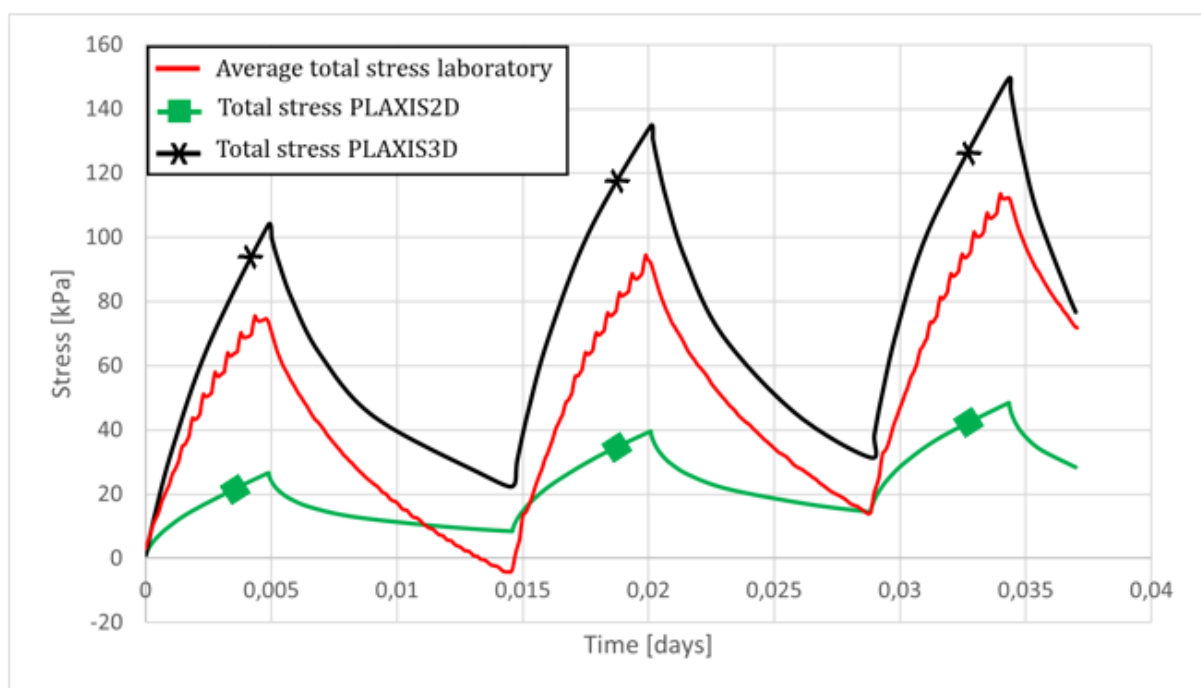


Figure 105: Time versus total stress from laboratory, PLAXIS2D and PLAXIS3D for T4.

Next, the values for total stress from the laboratory are given an offset of 30 kPa. This represents a reasonable total stress value gained prior to recording. It is plotted below together with the total stress development in PLAXIS3D. The two plots show a coinciding pattern and similar increments of total stress.

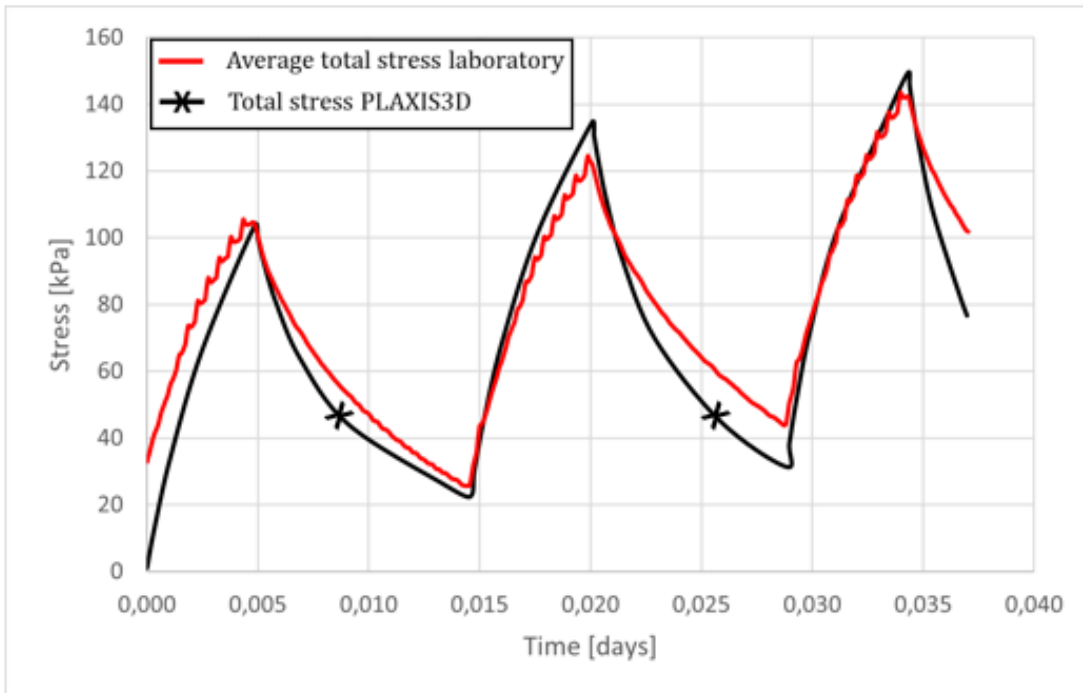


Figure 106: Time versus total stress for laboratory and PLAXIS3D for T4. Total stress values from laboratory given offset of 30 kPa.

The excess pore pressure from the laboratory and the PLAXIS3D analysis are compared below. Both increase simultaneously. During the decrease of pore pressure for the PLAXIS3D model, the pore pressure remains the same in the laboratory. The signal from the laboratory is weak and delayed compared to the simulated pore pressure. The recorded value in the laboratory does not suffice. This considering that the total stresses sensors do show a reasonable response compared to the numerical simulation. At the position of the porous stone excess pore pressure is expected to occur with similar magnitude of these recorded total stresses.

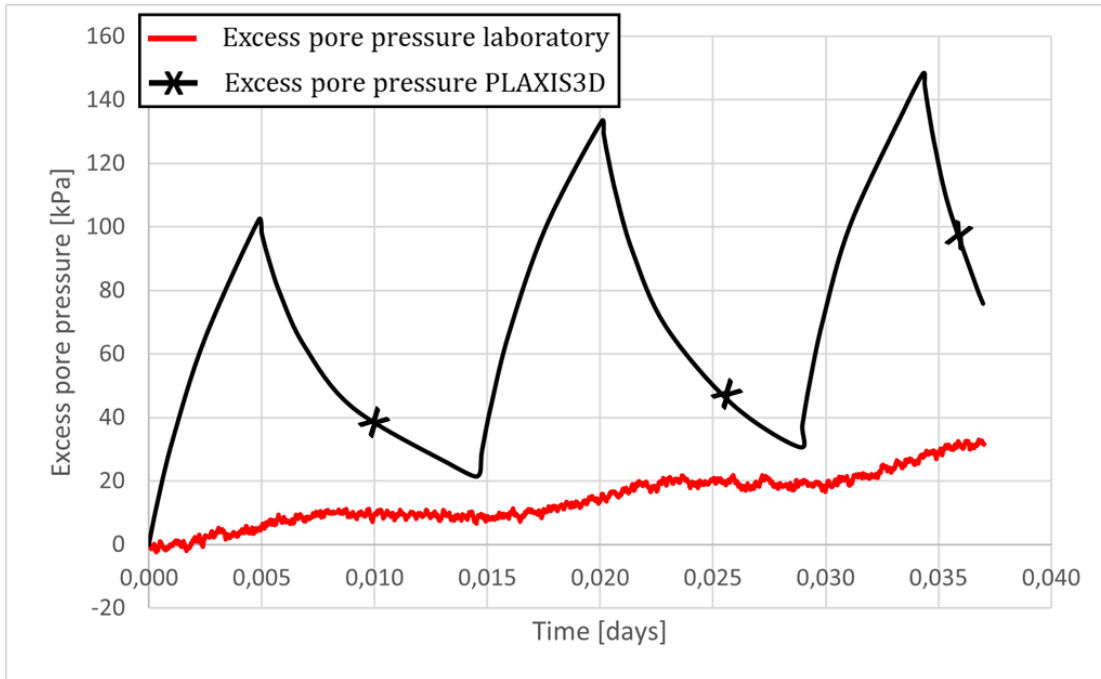


Figure 107: Time versus excess pore pressure for laboratory and PLAXIS3D for T4.

In the table below the ratio of pore pressure with respect to the average total stress measured is given. For T4, percentages of 17% and 25.3% are found at the end of the biaxial loading phase. These are improved values compared to the percentages of 9.1% and 15.9% for T3. Moreover, a milder contact procedure was followed for T4. At the end of phase 4 a ratio of 122.3% is found. Reasoning for this is the delay in pore pressure recording. The total stress decreases during relaxation, the pore pressure is delayed in this response and remains of high magnitude compared to the total stress measurement.

The ratio of minor stress and major stress in the same axial direction are evaluated in the table below. Again, the opposing total stresses measured in x-direction differ more compared to the opposing sensors in y-direction.

Table 24: Ratio of measurement for T4.

Phase	Ratio pore pressure of average total stress	Ratio minor and major total stress in x-direction	Ratio minor and major total stress in y-direction
Unit	Percentage [%]	Percentage [%]	Percentage [%]
Start	-	-	-
1	6.7	84.7	97.5
2	-	92.0	62.5
3	17.0	85.4	97.5
4	122.3	68.0	87.1
5	25.3	87.8	97.7
6	44.0	84.4	97.1

The excess pore pressure obtained from laboratory does not meet the expected value based on the numerical analysis. T4 has more reasonable values of excess pore pressure compared to T3. On top of that, during T4 a more cautious contact procedure was followed.

Despite these results, the excess pore pressure measured is not reliable. Alternative pore pressure measurements systems should be considered.

### **5.3.5. Conclusion test 5**

The goal for T5 was to obtain excess pore pressure measurement with a new design using a glass granule. Excess pore pressure is measured. However, this does not show the rapid response in excess pore pressure expected. The numerical analysis is not presented individually for T5. The numerical analysis previously presented for T3 and T4 is applicable to T5. An instantaneous response in excess pore pressure is expected for a biaxial loading phase. Especially, at the midpoint of the sample corresponding to pore pressure measurement position for T5.

The delay in excess pore pressure measurement obtained can be explained by the occurrence of air void around the glass granule during the test. This delays the signal of pore pressure.

## 6. Yield Surface Representation

A yield surface can be used to represent the strength of the soil. The background behind a yield surface is discussed in this chapter.

As mentioned, the measured stresses in the laboratory and in the numerical analysis are equal to the principal stresses. Previously, the normal stresses in x- and y- and z- direction were presented by  $\sigma_{xx}$ ,  $\sigma_{yy}$ ,  $\sigma_{zz}$ , respectively. In Chapter 6 and 7 it is chosen to represent them as major, intermediate, and minor principal stresses,  $\sigma_1$ ,  $\sigma_2$  and  $\sigma_3$ , respectively.

### 6.1. Yield criterion

Yielding is the transition from stiff elastic response to less stiff plastic response. It occurs whilst reloading a soil to a point where it exceeds the past maximum load. The current point of load then becomes a *yield point* with a stress state corresponding to the *yield stress* or *yield strength*. To further evaluate this division between elastic and plastic response a yield function,  $f$ , is used. The yield function is a product of stress invariants and optionally other parameters such as strain.

If  $f$  is less than zero, the soil behaves purely elastic. If  $f$  is equal to zero and its increment equals zero, the soil behaves elasto-plastic. This behaviour corresponds to the yield stress and can be represented as a border in stress space, shown in Figure 108. The border made by the yield function is often referred to as the *yield surface* or *yield contour*. Stress states that would lead to  $f$  larger than zero are impossible. This yield surface can be represented in several ways which will be evaluated next.

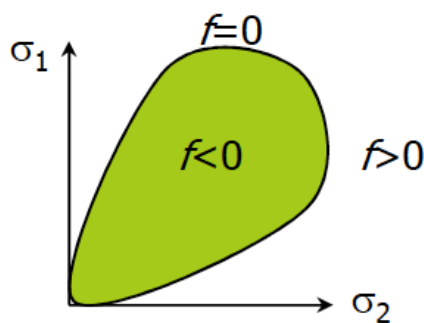


Figure 108:  $f = 0$  represented as a boundary in 2D stress space. (Brinkgreve, 2019)

One of the goals of this thesis is to represent the yield strength in plane strain conditions. It is therefore useful to elaborate the possibilities to visualise various yield criteria and the yield points. Clear representation of make it possible to compare the yield strength for different types of tests.

## 6.2. Strength criterion representation

If the values of principal stresses within a deforming body are known, the values can be plotted in Cartesian space with axes having dimensions of principal stress. This is referred to as principal stress space. It is shown in Figure 109, with the stress point representing an arbitrary state of stress.

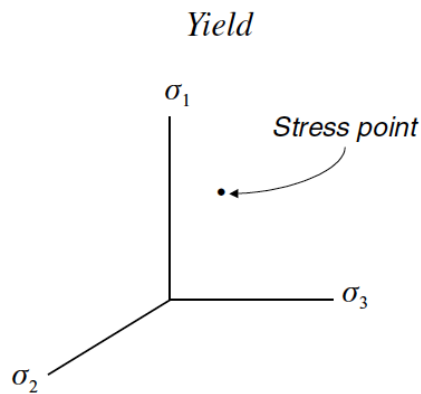


Figure 109: Principal stress space (Davis et al., 2002).

Changing the stress in the soil body will change the position of the stress point. Different positions correspond to either an elastic or a plastic response. If the soil starts behaving plastically it has reached the yield surface. As an example, the yield surface for the Mohr-Coulomb model is shown in Figure 110.

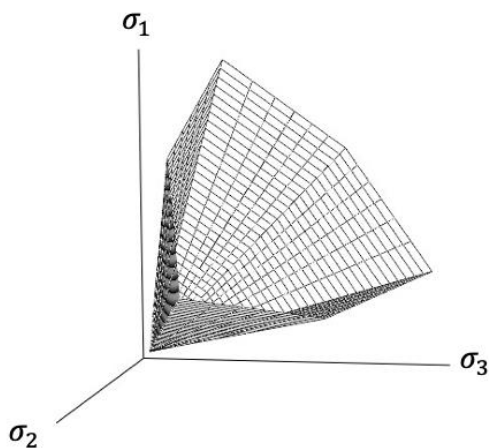


Figure 110: Yield function (Mohr-Coulomb) in principal stress space (Brinkgreve, 2019).

The space diagonal is a line on which a stress point has the same value for all three principal stresses. The *deviatoric plane* or  $\pi$ -plane is plotted perpendicular to the space diagonal (line of isotropic stress). This gives a different representation of the strength criterion in the deviatoric plane. In Figure 111 this is represented in principal stress space which gives the space diagonal a view towards the origin of the stress space.



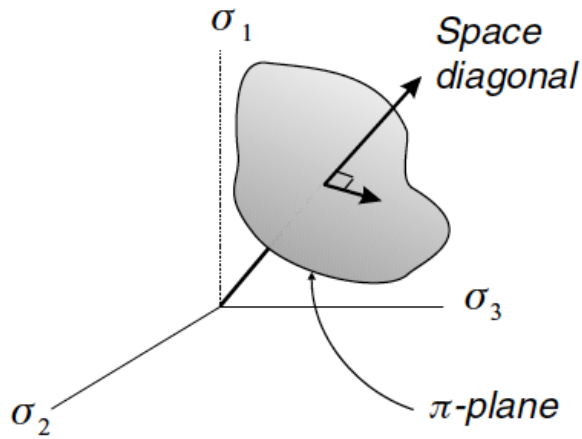


Figure 111: Deviatoric plane represented in principal stress space (Davis et al., 2002).

For the Mohr-Coulomb yield function, the deviatoric plane is shown in Figure 112.

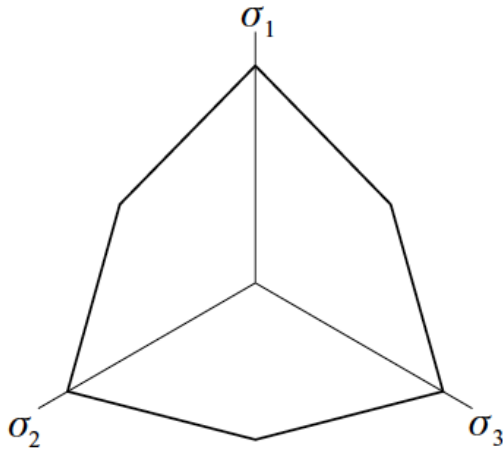


Figure 112: Deviatoric plane surface for Mohr-Coulomb with view along the space diagonal (Davis et al., 2002).

Next, the three principal stresses are again taken as axes, but the stress values are defined in a different orthogonal coordinate system. The stresses can be projected on the deviatoric plane by three orthogonal unit vectors in 'D', 'E' and 'F' direction (Davis et al., 2002). One of these vectors lays on the space diagonal whilst the other two lay on deviatoric plane. The stresses in these directions are related to the principal stresses by Formulas 8, 9 and 10.

$$\sigma_D = \frac{1}{\sqrt{3}}(\sigma_1 + \sigma_2 + \sigma_3) = \sqrt{3}p \quad (8)$$

$$\sigma_E = \frac{1}{\sqrt{2}}(-\sigma_2 + \sigma_3) \quad (9)$$

$$\sigma_F = \frac{1}{\sqrt{6}}(2\sigma_1 - \sigma_2 - \sigma_3) \quad (10)$$

Zwanenburg et al. (2019) presented LDSS test results in the deviatoric plane using the orthogonal unit vectors, shown below in Figure 113. To support the construction of the

yield surface, triaxial compression and extension tests were conducted and added to the plot.

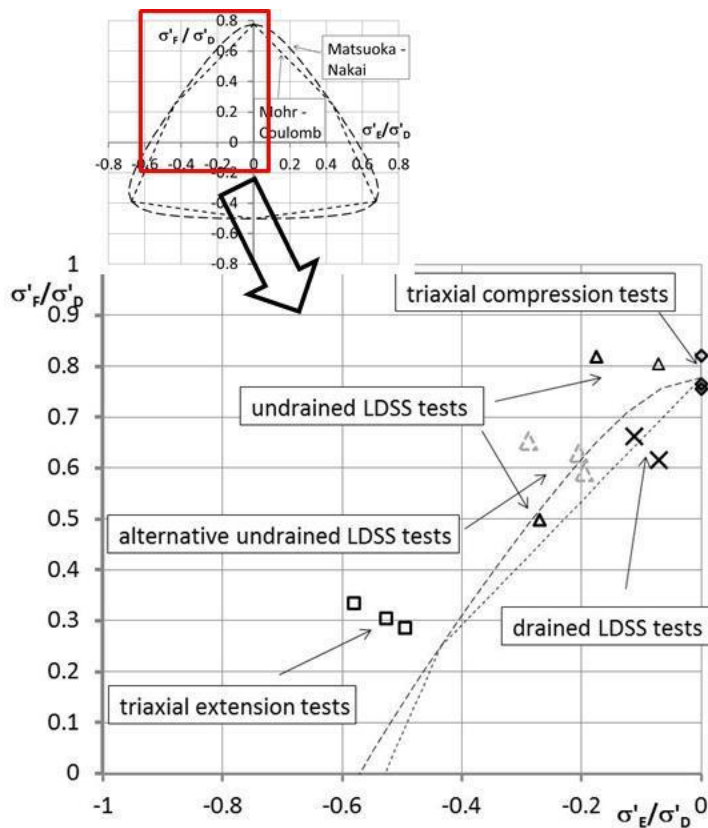


Figure 113: LDSS, triaxial compression and triaxial extension results plotted in the deviator-plane (Zwanenburg et al. 2019).

To summarise, in principal stress space, the stress point may be described in any of three ways: by the principal stresses  $\sigma_1, \sigma_2, \sigma_3$  by the stress components  $\sigma_D, \sigma_E, \sigma_F$ , or even by stress invariants such as  $p, q, \theta$  that virtually create a separate polar coordinate system. The stress invariants  $p, q, \theta$  are evaluated in Paragraph 6.3. In some cases, one description may be preferable to another, but all three describe exactly the same state of stress in the body. (Davis et al., 2002)

### 6.3. Stress invariants

The state of stress can be defined by either the stress matrix, Formula 1, or by specifying the magnitude of the principal stresses and the three directions of the planes on which they act. For a certain soil configuration, the principal stresses always act on the same planes and have the same magnitude. Therefore, they are invariant of the choice of axes (Potts et al., 1999). In geotechnical engineering it can be convenient to work with alternative invariant quantities which are combinations of the principal stresses and act according to the general relation of invariants described in Appendix B.

A relation is found between the principal stresses and stress invariants. The mean effective stress,  $p$  and deviatoric stress,  $q'$  are given in Formulas 11 and 12 for plane strain conditions (Wanatowski et al., 2006; Kumruzzaman et al. 2011). The Lode's angle,  $\theta$ , presented by Potts et al. (1999) is given in formula 13. These parameters can be used to extend the stress conditions to three dimensional models. These invariants merely

represent a coordinate change from principal stresses (which are Cartesian coordinates for stress space) to the natural cylindrical coordinates ( $q, \theta, p'$ ) for which the  $p'$ -axis points along the hydrostatic axis (Brannon, 2007).

$$q = [(\sigma_1 - \sigma_2)^2 + (\sigma_2 - \sigma_3)^2 + (\sigma_3 - \sigma_1)^2]^{1/2} / \sqrt{2} \quad (11)$$

$$p' = (\sigma_1' + \sigma_2' + \sigma_3') / 3 \quad (12)$$

$$\theta = \tan^{-1} \left[ \frac{1}{\sqrt{3}} \left( 2 \frac{(\sigma_2' - \sigma_3')}{(\sigma_1' - \sigma_3')} - 1 \right) \right] \quad (13)$$

The geometric significance of the invariants in principal effective stress space is shown in Figure 114. The value for deviatoric stress gives a measure of the distance of the stress state from the space diagonal. The value of mean effective stress is a measure of the distance along the space diagonal. The Lode's angle determines the angular position of a stress state (marked with A') with respect to the failure surface.

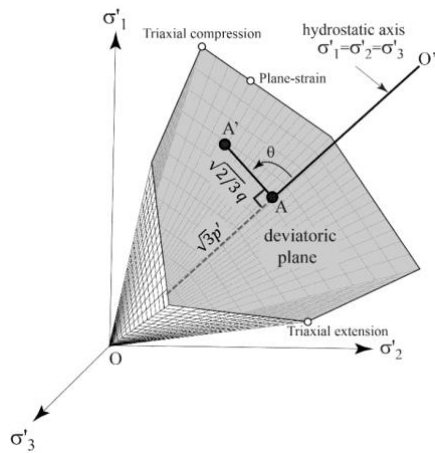


Figure 114: 3D strength criterion with the Mohr-Coulomb failure surface plotted in principal stress space. (Abed et al, 2018).

For different types of tests, e.g. triaxial compression, triaxial extension or plane-strain, the Lode's angle corresponds to a different orientation of the stress state within the criterion. The exemplary stress state found in Figure 114, point A', meets the following requirement  $\sigma_1'^{A'} \geq \sigma_2'^{A'} \geq \sigma_3'^{A'}$ . Therefore, A' is constrained to lie between the lines with Lode's angles,  $\theta = -30^\circ$  and  $\theta = +30^\circ$ , found in Formula 13. Triaxial compression with condition,  $\sigma_1'^{A'} \geq \sigma_2'^{A'} = \sigma_3'^{A'}$ , occurs at  $\theta = -30^\circ$ . Triaxial extension  $\sigma_1'^{A'} = \sigma_2'^{A'} \geq \sigma_3'^{A'}$  corresponds to  $\theta = +30^\circ$ . For plane strain conditions the Lode's angle will take a value in the range from  $\theta = 0$  to  $\theta = -30^\circ$ . Most soils fail with  $\theta$  ranging from  $\theta = -10^\circ$  and  $\theta = -25^\circ$  (Potts et al, 1999). An illustrative stress path arrow for a biaxial test, indicated with 'b' and a triaxial compression test stress path arrow indicated with 'a' are shown below in figure 115.

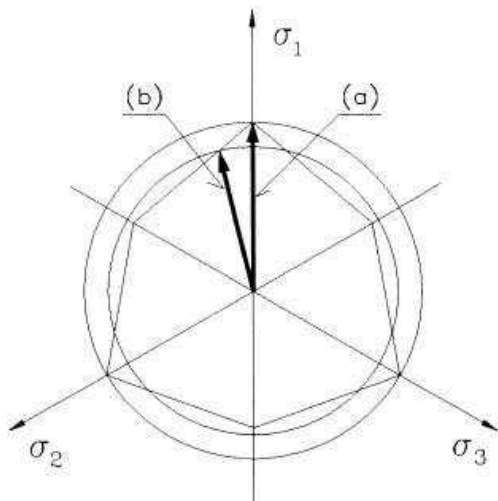


Figure 115: Stress path for biaxial test (b) and triaxial compression test (a) plotted in the  $\pi$ -plane (Sterpi, 2000).

## 7. Yield surfaces and criteria

Traditionally the yield stresses of soils have been represented by the Mohr-Coulomb criterion. More recently, other yield criteria have been proposed to predict the failure of soil such as the Matsuoka-Nakai criterion, the Lagioia and Panteghini formulation and the criterion presented by Teunissen. These yield surfaces will be elaborated in the following sections.

### 7.1. Mohr-Coulomb failure criterion

All together the behaviour of the soil depends on the strain level, stress level and the stress path. These features are incorporated in the advanced soil models found in PLAXIS (Material Models Manual, 2021). A relatively simple model to perform a first analysis with is the Mohr-Coulomb model. The Mohr-Coulomb is a general shear strength criterion for soils (Brinkgreve, 2019). This is 'linear elastic perfectly plastic' model, with as primary and general principle that strain can be decomposed in an elastic part and a plastic part. This principle also holds for other constitutive model where the elastic part behaves according to Hooke's law described in Appendix C. The plastic part is based on the Mohr-Coulomb failure criterion described below.

The starting point of the model is the Coulomb friction law. A normal stress,  $\sigma'_n$ , and shear stress,  $\tau$ , act on a failure plane. This failure plane is situated at an arbitrary angle with respect to the principal stress components. The Mohr's circle can be used to reformulate the stresses into principal stresses. This leads to the Mohr-Coulomb failure criterion given in principle effective stress components with  $c'$  as cohesion and  $\varphi'$  the friction angle.

$$\frac{1}{2}(\sigma'_3 - \sigma'_1) \leq c' \cos \varphi' - \frac{1}{2}(\sigma'_3 + \sigma'_1) \sin \varphi' \quad (14)$$

There are three principal stresses which can all make a combination with one another. Hence, the full Mohr-Coulomb failure criterion consists of the following three yield functions:

$$f_1 = \frac{1}{2}|\sigma'_3 - \sigma'_2| - \frac{1}{2}(\sigma'_3 + \sigma'_2) \sin \phi - c \cos \phi \quad (15)$$

$$f_2 = \frac{1}{2}|\sigma'_1 - \sigma'_3| - \frac{1}{2}(\sigma'_1 + \sigma'_3) \sin \phi - c \cos \phi \quad (16)$$

$$f_3 = \frac{1}{2}|\sigma'_2 - \sigma'_1| - \frac{1}{2}(\sigma'_2 + \sigma'_1) \sin \phi - c \cos \phi \quad (17)$$

In most cases only one of these yield functions will be active during the same time (Sitters, 2006). These functions can be plotted in principal stress space and deliver a yield function. This 3D representation is shown in Figure 110 in Chapter 6.

The Mohr-Coulomb yield function  $f$  can also be written in terms of stress invariants given by Formula 18 (Sitters, 2006).

$$f = p' \sin \varphi' + q \left( \frac{\cos \theta}{\sqrt{3}} - \frac{\sin \theta \sin \varphi'}{3} \right) - c \cos \varphi' \quad (18)$$

Lode's angle is defined here as:

$$\theta = \frac{1}{3} \sin^{-1} \left[ \frac{(\sigma'_1 - p')(\sigma'_2 - p')(\sigma'_3 - p')}{q^3} \right] \quad (19)$$

It is also possible to use the Mohr-Coulomb failure criterion in combination with the Modified Cam-Clay yield function defined in Appendix C. The parameter  $M$  represents the angle of failure in the  $p'$ - $q$  plane and should depend on the lode angle by Formula 20 (Zwanenburg et al., 2018).

The formula describes the shape of the yield curve in the  $\pi$ -plane.  $M_c$  and  $M_e$  represent the angle of the failure line in the  $p$ - $q$  plane for triaxial compression and triaxial extension, respectively.

$$M(\theta) = \frac{3\sqrt{3}M_c}{(6 + M_c)\cos(\theta) + \sqrt{3}M_c \sin(\theta)} \quad (20)$$

## 7.2. Drucker Prager

Drucker and Prager (1951) suggested the Drucker Prager criterion which forms a cone surface around the hydrostatic axis in principal stress space. The expression for the yield criterion can be expressed with the second deviatoric invariant,  $J_2^{\sigma^d}$  and the first invariant,  $J_1^\sigma$ . These two parameters are described in Appendix C.  $\alpha$  and  $\beta$  are material parameters which can be chosen to fit the Mohr-Coulomb criterion by expressing them by cohesion,  $c'$ , and the friction angle,  $\varphi'$ .

$$f = \sqrt{3J_2^{\sigma^d} + \alpha J_1^\sigma} - \beta \quad (21)$$

The following setting of these material parameters can be chosen to equal to Mohr-Coulomb in plane strain or circumscribe the Mohr-Coulomb surface (Nielsen et al., 2019)

Drucker Prager equals Mohr-Coulomb in plane strain condition:

$$\alpha = \frac{\sin \varphi'}{\sqrt{3 + \sin^2 \varphi'}} \quad (22)$$

$$\beta = \frac{3c' \cos \varphi'}{\sqrt{3 + \sin^2 \varphi'}} \quad (23)$$

Drucker Prager circumscribes Mohr-Coulomb:

$$\alpha = \frac{2 \sin \varphi'}{3 - \sin \varphi'} \quad (24)$$

$$\beta = \frac{6 c' \cos \varphi'}{3 - \sin \varphi'} \quad (25)$$

This can be represented in the deviatoric plane by the figure below (Nielsen et al., 2019). The Drucker-Prager criterion is independent on the Lode Angle, as the angular position of the cone does not give different relation of the stress state.

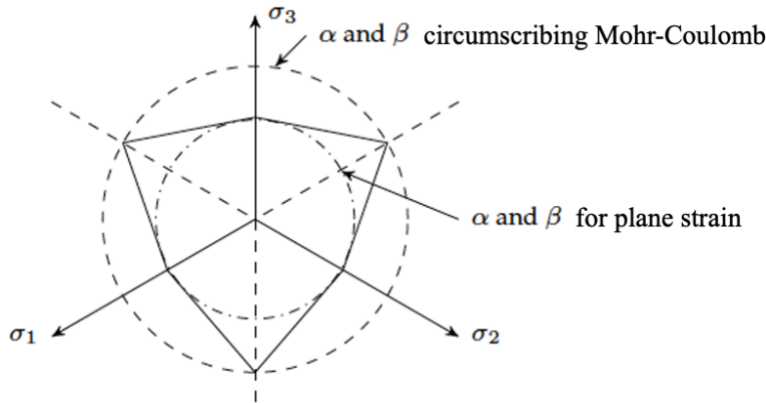


Figure 116: Drucker Prager relationship to Mohr-Coulomb for different material parameters chosen.

### 7.3. Matsuoka-Nakai failure criterion

A downside of the Mohr-Coulomb criterion is its neglect of the intermediate principal stress,  $\sigma_2'$  (Griffiths et al., 2009). The Matsuoka-Nakai failure criterion was proposed by Matsuoka and Nakai (Matsuoka et al., 1974) and includes this intermediate principal stress. Matsuoka-Nakai is considered a slightly better criterion for shear failure in soils than Mohr-Coulomb, although the latter is used the most (Brinkgreve., R. 2019). The two criteria are very similar, and the curves have the subtle property that the shape varies with the friction angle; as  $\phi$  decreases the shape becomes more circular, and as  $\phi$  increases the shape becomes more triangular (Wroth, 1984).

The Matsuoka Nakai criterion has the concept of averaging the Mohr-Coulomb criterion under three principal stresses. The following relationship between the stress invariants should remain constant (Matsuoka et al., 1974):

$$\frac{J_1^\sigma J_2^\sigma}{J_3^\sigma} = constant \quad (26)$$

The yield function is given by Griffiths et al. (2009) and shown below.

$$f = K_{MN} \frac{J_1^\sigma}{J_1^\sigma} - J_1^\sigma \quad (27)$$

$K_{MN}$  being a material constant given by Formula 28 with  $\varphi_c'$  the friction angle.



$$K_{MN} = \frac{9 - \sin^2 \phi'_c}{1 - \sin^2 \phi'_c} \quad (28)$$

The Matsuoka-Nakai criterion matches the Mohr-Coulomb criterion in compression as well as extension points, but it is smooth and goes outside Mohr-Coulomb in other than compression and extension points (Brinkgreve., R. 2019). These two failure criteria are plotted in the deviatoric plane (Matsuoka et al., 1985).

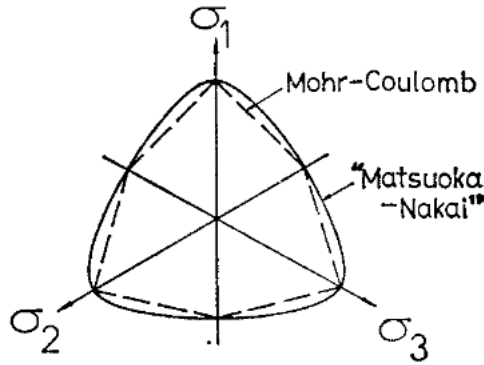


Figure 117: Mohr-Coulomb and Matsuoka-Nakai plotted in the deviatoric plane (Matsuoka et al., 1985).

These findings are illustrated in Figure 118 where P indicates the point on the failure surface corresponding to plane strain conditions. The line CD is a line of constant  $\phi$  and matches the Mohr Coulomb surface (Wroth, 1984). The parameter b gives the relative value of the intermediate principal effective stress and was introduced by Bishop (1966) and is given by Equation 29.

$$b = \frac{\sigma'_2 - \sigma'_3}{\sigma'_1 - \sigma'_3} \quad (29)$$

The value of b varies from unity for triaxial extension to zero for triaxial compression. The value of b for plane strain conditions holds for the relation given by Formula 30 (Wroth, 1984). The friction angle is given for plane strain conditions.

$$2b_{ps} \approx \frac{\sin \phi_{ps} + \cos \phi_{ps} - 1}{2 \sin \phi_{ps}} \quad (30)$$

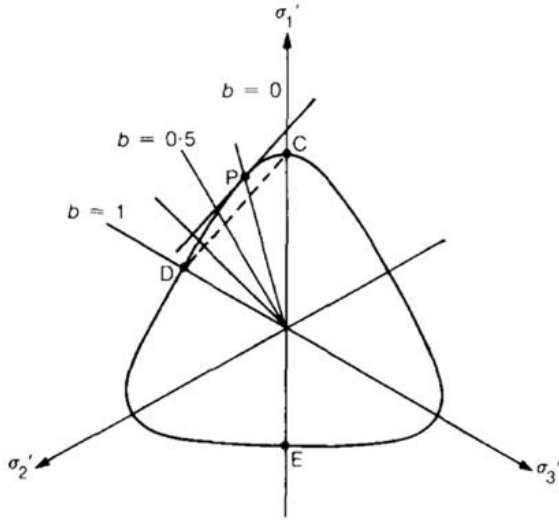


Figure 118: Plane strain conditions for the Matsuoka-Nakai criterion plotted in the deviator-plane (Wroth, 1984).

It is desirable to relate the friction angle for triaxial conditions to that for plane strain conditions. Satake (1982) shows that if an associated flow rule is applied to the Matsuoka failure criterion, then for plane strain conditions,  $\phi_{ps}$  is the maximum value that  $\phi$  can have.

Again, for the Matsuoka-Nakai failure criterion it also possible to combine it with the Cam-Clay yield function. The parameter  $M$  should then depend on the Lode angle by relations 34 and 35 (Zwanenburg et al., 2018).  $M_e$  is the critical state line for the Cam-Clay model in triaxial extension.  $M_c$  is the critical state line for the Cam-Clay model in triaxial compression.

$$M(\theta) = \frac{\sqrt{3}}{2} \frac{M_c \beta}{\sqrt{\beta^2 - \beta + 1}} \frac{1}{\cos \left\{ \frac{1}{6} \cos^{-1} \left[ -1 + \frac{27}{2} \frac{\beta^2 (1 - \beta)^2}{(\beta^2 - \beta + 1)^3} \sin^2(3\theta) \right] \right\}} : \theta \geq 0^\circ$$

$$M(\theta) = \frac{\sqrt{3}}{2} \frac{M_c \beta}{\sqrt{\beta^2 - \beta + 1}} \frac{1}{\cos \left\{ \frac{\pi}{3} - \frac{1}{6} \cos^{-1} \left[ -1 + \frac{27}{2} \frac{\beta^2 (1 - \beta)^2}{(\beta^2 - \beta + 1)^3} \sin^2(3\theta) \right] \right\}} : \theta < 0^\circ$$

(31, 32)

With parameter  $\beta = \frac{M_e}{M_c}$

### 7.3. Lagioia and Panteghini

Classical yield criteria, such as the Mohr-Coulomb and Matsuoka and Nakai criteria are affected by limitations creating numerical difficulties (Lagioia, 2016). The lack of smoothness and the non-convex yield surfaces being the most notorious for the Mohr-Coulomb and Matsuoka-Nakai criterion, respectively. Lagioia et al., (2016) have created a method to derive a general yield criterion for a constitutive model. The equation makes use of classical yield criteria for soils namely the Matsuoka Naki, Lade-Duncan,

Tresca, Drucker-Prager, von Mises and Mohr-Coulomb criteria. The general yield surface formulation is given below:

$$f(\sigma) = -(K + Mp) + J\alpha \cos \left[ \frac{\cos^{-1}(\beta - \sin 3\theta)}{3} - \gamma \frac{\pi}{6} \right] = 0 \quad (33)$$

The parameters  $\alpha, \beta$  and  $\gamma$  define the shape for the specific yield criteria and are given by Lagioia et al. (2016).  $M$  is the slope of the critical state line in triaxial conditions.  $K$  depends on the Mohr-Coulomb values  $c'$  and  $\phi$  with the relation  $K = c' \cot \phi$ .

The Matsuoka-Nakai criterion parameters can be used for Formula 33. The resulting expression can be plotted in 3D principal stress space. In Figure 119, only the compressive octant of the principal stress space is retrieved from Formula 33. This is the same branch originating of the multi-branch surfaces of the original criterion shown in Figure 120 (Panteghini et al., 2013).

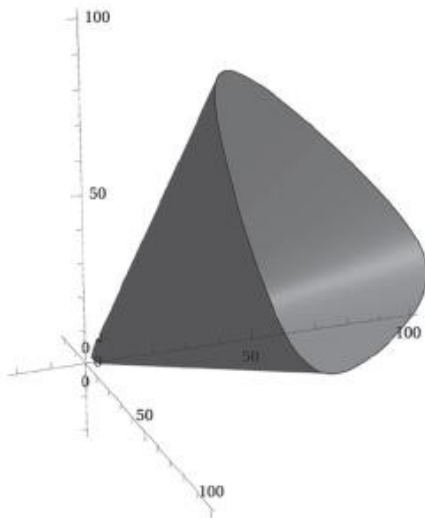


Figure 119: Plot of the reformulated Matsuoka-Nakai yield surface in the positive octant in principal stress space (Panteghini et al., 2013).

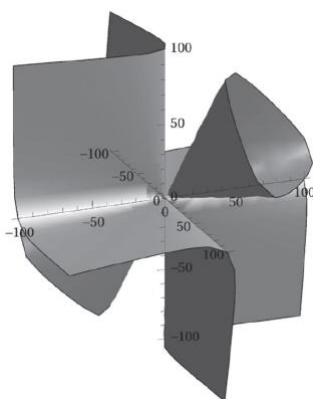


Figure 120: Plot of the original Matsuoka-Nakai yield surface in principal stress space (Panteghini et al., 2013).

Its structure is found to be efficient in numerical analyses and is suitable for shaping the yield surface in the deviatoric plane for complex constitutive models.

## 7.4. Teunissen (2022)

Teunissen (2022) gives a general expression for strength in the deviatoric plane. The influence of the intermediate principal stress is emphasized, relevant for plane strain conditions and relevant for modelling stresses in 3D space.

A general function of the yield function,  $f$ , is given below:

$$f = q\Gamma(\theta) - \frac{6}{3 - \sin \phi_{tc}} (p \sin \phi_{tc} + c_{tc} \cos \phi_{tc}) = 0 \quad (34)$$

The strength parameters, cohesion  $c_{tc}$  and friction angle  $\phi_{tc}$ , are for triaxial compression condition.  $\Gamma(\theta)$ , defines the shape of the yield function in the deviatoric plane. For triaxial compression  $\Gamma(\theta) = 1$  and for triaxial extension  $\Gamma(\theta) = \frac{1}{r}$ . Extension ratio  $r$  can be altered to convert to other models. To obtain the Matsuoka-Nakai criterion,  $r$  should be taken as  $r = \frac{3 - \sin(\phi'_{tc})}{3 + \sin(\phi'_{tc})}$ .

Hence, triaxial compression tests are used to obtain most of the parameters for the strength criterion. Using this as a reference will only define the strength criterion based on a single point on the deviatoric stress plane. Other points, retrieved from for instance triaxial extension or plane strain tests, are desired to determine the full shape of the yield function.

The general model is reformulated to describe the yield function in terms of three principal stresses:

$$f = \left( \frac{\sigma'_1 - \sigma'_3}{2} \right) - \left( \frac{(3 - \sin \phi_{tc}) \Gamma(\theta)}{2\sqrt{3} \cos \theta} - \frac{\tan \theta}{\sqrt{3}} \sin \phi_{tc} \right) - \left( \left( \frac{\sigma'_1 + \sigma'_3}{2} \right) \sin \phi_{tc} + c_{tc} \cos \phi_{tc} \right) = 0 \quad (35)$$

This 3D model is matched with the Mohr-Coulomb yield function for maximum stress in plane strain conditions:

$$f = \left( \frac{\sigma'_1 - \sigma'_3}{2} \right) - \left( \left( \frac{\sigma'_1 + \sigma'_3}{2} \right) \sin \phi_{ps}^m + c_{tc} \cos \phi_{ps}^m \right) = 0 \quad (36)$$

## 7.5. Plane strain parameters versus axial symmetric parameters

Our comprehension of the stress-strain behaviour of soils under plane strain conditions is relatively underdeveloped (Wanatowski et al., 2006). The friction angle under plane-strain conditions is measured to be higher than under triaxial conditions. According to Mohr-Coulomb the friction angle only depends on  $\sigma_1$  and  $\sigma_3$ . For this reason, Kumruzzaman et al. (2011) only made use of these two stresses to calculate the friction angle under plane strain condition:

$$\varphi' = \sin^{-1} \left[ \frac{\sigma_1' - \sigma_3'}{\sigma_1' + \sigma_3'} \right] \quad (37)$$

According to Wroth (1984) the relation between the friction angle for plane strain conditions,  $\varphi'_{ps}$  and the friction angle for triaxial compression,  $\varphi'_{txc}$  is given by  $\varphi'_{ps} = \frac{9}{8} \varphi'_{txc}$ .

All the above, are examples of the difference in parameter determination for triaxial and plane strain conditions. Obtaining results with the biaxial device could prove the difference in parameters for triaxial conditions and plane strain conditions.

## 8. Conclusion

To get results with the biaxial device the biaxial apparatus by Allersma (1993) was refurbished. Step motors are reinstalled, and an input panel is developed. This made it possible to control the apparatus again. The confining plates can be driven in a strain-controlled manner. Driving the apparatus gave insights on the possibilities of the control. For instance, the minimum possible displacement rate is found to be  $0.00021 \frac{mm}{s}$ . Also, a few displacement increments should be taken before reaching the intended incremental displacement as the motors need to shift into the correct gear.

Preliminary laboratory tests gave realistic output of total stresses in x and y-direction. Still, challenges were encountered during these tests. Improvements on safety and stability are made. This increased the chance of performing a stable laboratory test. The apparatus is made working and can be precisely controlled.

Next, the second challenge is to obtain reliable results with the biaxial apparatus. A new bottom plate is installed including a total stress sensor. This made it possible to measure the total stress in the vertical z-direction. The upper plate should be tightened up accordingly. Also, great care should be taken to make contact between the upper plate and the sample. This gives more realistic output for total stress in this z-direction.

In the bottom plate a hole is made allowing the instalment of a pore pressure measurement system. A porous stone is placed which is connected to an excess pore pressure sensor. Several designs are made for measurement of the excess pore pressure. Using the porous stone as a drainage outlet did not lead to the intended performance. Water did not drain out of the water outlet and subsequent tests are performed with undrained conditions at the centre of the sample.

The total stresses found in the laboratory give comparable increments of total stress to one another in x-y and z-direction for biaxial loading. Giving symmetrical displacement for all four sides increases the correspondence of the total stress measurement. Also, for a higher displacement rate an increased consistency in the total stress readings is found. Variation in total stress measurement, particularly for opposing plates, remain. This gives an insufficient accuracy of the total stress measurement for the intended scope of this research. Water is seen seeping out of the gaps between the wall at the biaxial cell boundary. This entails uncontrolled drained conditions during the laboratory test. Using a latex cover does not restrict water seeping out.

The laboratory tests are translated to a model in PLAXIS2D and PLAXIS3D. The OVP clay soil parameters retrieved from Deltares are used in the numerical analysis. Displacement schemes performed in the laboratory are re-created and analysed using these programmes. It is found that for a phase of biaxial loading the total stresses should increase equally considering their position of measurement. The increase in total stress found in the laboratory compares to the results from the numerical analysis in PLAXIS3D.

The uncontrolled drainage conditions are implemented in the numerical models in PLAXIS2D and PLAXIS3D. In the laboratory, the drainage conditions vary along the boundary between sample and biaxial cell. The gaps between the plates are measured and vary in size between the different metal plates. These gaps can be accounted for in PLAXIS3D. As the soil is subjected to an increase in pressure, the water diffuses away to the gaps. These gaps make up only a fraction of the side boundaries of the three-dimensional model. Relatively high pore pressures develop. The PLAXIS2D model does not specify the area of these borders and allows drainage over the entire boundary of the two-dimensional plane. The relative pathways for water to diffuse away from are large. As water dissipates away, relatively low pore pressures are generated. This difference in ratio between sample area and boundaries set to drainage leads to the difference in outcome between PLAXIS2D and PLAXIS3D. Also, the position of total stress measurement varies along the three axes. This corresponds to a three-dimensional solution. The numerical analysis in PLAXIS3D is believed to be the most suitable for this lab test set up. The PLAXIS2D analysis overestimates the laboratory seepage behaviour resulting in lower total stresses.

Placing a water column, instead of a soil sample, above the pore pressure measurement system results in expected recordings. When placing a soil sample, the measurement of excess pore pressure in the laboratory test set up does not give useful recordings. Improving the quality of the test procedure gives more justifiable recording. For biaxial loading it increases whilst relaxation gives a decreasing trend. However, the magnitude still proves the insufficient and the response is delayed. The values measured for the excess pore pressure are of small magnitude compared to the value of excess pore pressure expected from the numerical analysis. The numerical analysis shows an instantaneous increase in excess pore pressure for the intended biaxial loading step. This sharp response is not seen from the laboratory. Setting a hydraulic conductivity factor 5 times higher than the known hydraulic conductivity, gives lower values of excess pore pressure in sample during the test in the numerical analysis. Still, these values of excess pore pressure remain higher than those recorded in the laboratory.

The alternative designs presented for excess pore pressure measurement do not show improvement in instantaneous excess pore pressure recording. Improving the contact procedure and retrieves more reliable values for the total stresses and excess pore pressure. However, fully verifiable results are not obtained using the biaxial apparatus in this research.

To obtain the failure criterion using the biaxial apparatus the phase of biaxial loading should be understood firmly. Biaxial loading will give consolidation behaviour as water seeps out of the side wall. Repetitive phases of biaxial loading and relaxation will give a consolidated sample with sufficient values of effective stress. The recording of the excess pore pressure was found to be insufficient to prove this behaviour. This behaviour should be recorded first before proceeding to the shearing phase.

This goal is not reached in this thesis. In this final stage, the sample would be sheared eventually leading to failure. In the numerical analysis it is found that, for a constant volume and no external load applied, the excess pore pressure does not increase during this phase. Another challenge arises as a controlled undrained condition cannot be maintained during the tests with the biaxial apparatus.



## 9. Discussion and recommendations

In this chapter the challenges tackled with the biaxial apparatus are discussed. This is combined with future recommendations for research with the biaxial apparatus.

### 9.1 Technical specifications.

The first part of this discussion concerns the technical specifications of the apparatus. During the tests presented in this thesis the minimum displacement rate of 0.00021 mm/s was a limiting factor. Stresses increased rapidly for this displacement rate. During a biaxial loading phase, the total stresses increased to such an extent that a relaxation phase was required.

A smaller minimum displacement rate is also convenient regarding the contact procedure. Despite caution, the total stresses increase rapidly with the minimum displacement rate. A motor with a lower range of displacement rate broadens the applicability of the device, enabling performance of different type of laboratory tests.

The total stresses were measured with the original sensors by Allersma (1993). They gave realistic output; however, the signal is found to be distorted and inaccurate. The range of the sensors is large compared to the stresses intended for the scope of this thesis. Also, throughout the process of this thesis, these sensors had to be calibrated and/or replaced several times. It is therefore advised to consider the applicability of these sensors in future studies. Using a total stress sensor with a smaller range will be beneficial. If another type of total stress is considered the possibility to install them in the metal plates should be considered. These metal plates are cut for this type of sensors and new plates may be required.

Measurement of stress occurs at varying axial positions in the biaxial cell. Proving the effective stress for the entire sample, require positioning of more total stress and/or pore pressure sensors at the biaxial cell boundaries.

Two water pressure meters were installed during this thesis. One with low measuring range and another with a high measuring range. The high range pore pressure transducer was inaccurate for the stress range intended. The low measuring range meter was connected to long tubes making it difficult to fully saturate the system with water. Future design should ensure that the cables are short to reduce the chance of an unsaturated system. Also, a high-accurate pore pressure transducer should be considered in future designs. The KPE-200PB miniature pore pressure gauge is a recommended option and is shown below (TML, 2021). It has a range up to 200 kPa and is not affected by outer lateral pressure. The filter is directly connected to a transducer which avoids the placement of metal tubes. The filters are replaceable, and a suitable density of the filter mesh is available on request.

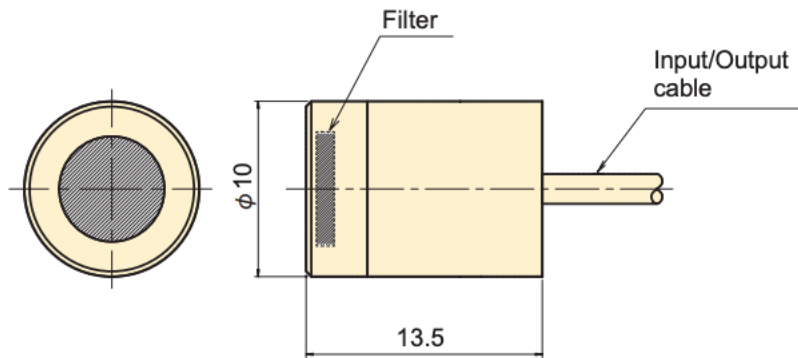


Figure 121: Sketch of KPE-200PB miniature pore pressure gauge (TML, 2021). Values given in mm.

## 9.2 Biaxial test set up

Before performance of a test, it was found that greasing the plates reduced the friction. A latex cover was also used enclosing the sample; however, no benefit was found for the use of this measure.

Apart from the high displacement rate, the contact procedure was complicated by a slightly asymmetrical sample. This was due to the design of the mold. Robust soil sampling tools should be considered to reach perfectly symmetrical samples.

The displacements are carried out using strain control mode. This limits the possibilities to reach desired states of stress. Especially with the minimum displacement rate possible. Stress control mode is welcome feature to broaden the possibility of stress configurations imposed on the sample. This control mode would require advanced effort to implement this via the system control.

During the laboratory test water is seen seeping out of the biaxial cell at the boundaries between two plates. Drainage conditions cannot be maintained. The gaps between the plates are at most 0.2 mm. This is believed to be due to the slightly skewed plates. Making better connection between the plates, possibly by installing new plates, would increase the chance of maintaining the drainage conditions.

Measuring the excess pore pressure proved a challenge. The uncontrolled drainage conditions contribute to this issue. The water cannot build up pressure at the porous stone and flows out via the gaps at the boundaries of the biaxial cell. A slightly asymmetrical sample will also contribute to this effect. The bottom of the sample might not be exactly flat, leading to preferential water pathways between the bottom plate and the sample. Resolving the issue of the gaps will improve the excess pore pressure measurement. Also, using a more robust sampling technique will give more precise samples and decrease the chance of void space in the biaxial cell.

The design using the glass granule creates a boundary between sample and filter material inside the sample. The intended design did not give viable reading of excess pore pressure yet. However, placing the contact point deeper inside the sample could prove to increase the chance of viable measurements. The KPE-200PB pore pressure gauge is 1 cm in diameter and has a perfectly cylindrical shape. This could prevent

distortion of the sample to a minimum whilst placing it a few millimetres into the sample. Another benefit is that the filter is placed deeper into the casing. The soil being pressed onto the filter will be confined by the casing. This prevents occurrence of air voids at the soil-filter interface.

Tightening up the upper plate firmly and trimming the sample with an extra 1 mm in z-direction ensures good contact between the porous stone and the sample. This gave the most realistic output for excess pore pressure. However, it is not an ideal situation as the sample may be distorted during this operation.

### **9.3. Numerical analysis**

The drainage conditions found in the laboratory are implemented in PLAXIS. PLAXIS2D gives an unrealistic representation of the drainage paths in the biaxial cell. The boundaries in the mesh are set to drained conditions. In reality, it is only at the gaps between the plate that seepage occurs and not the entire boundary. It is a three-dimensional problem as the measurement of stress occurs at different position of  $x$ ,  $y$  and  $z$ . The laboratory measurements obtained do not coincide with the numerical analysis. It is not advised to translate this test set up into PLAXIS2D.

PLAXIS3D showed more potential to reproduce the biaxial test set up. Using this numerical analysis helps understanding the results found in the laboratory. The exact, displacement rate, dimensions, test time and seepage boundaries are implemented in the analysis. The main uncertainty lies in the soil model as the OVP Clay hydraulic conductivity parameters obtained from Deltares are used for the numerical analysis. The OVP Clay used for the tests presented may have differing parameters.

### **9.4. Future recommendations**

The biaxial apparatus has been upgraded compared to its state after 18 years of inactivity. It is possible to control the device and obtain stress values. However, these are inaccurate and do not contribute to further theoretical research at this moment. The unique design of this apparatus gives possibilities to perform a plane strain test. It is questionable if future research on the intended subject for this thesis is justifiable using this device.

Various improvements should be made. To ensure a fully controlled test this gives a following summation of recommended improvements:

- Instalment of new total stress sensors with a more applicable range.
- Instalment of a new pore pressure transducer with a more applicable range.
- Design of a new excess pore pressure measurement system. Ideally requiring advanced, accurate and system-controlled tubing.
- Placing of new motors to provide a lower displacement rate of the metal plates.
- Replacement of the plates to ensure a more confined biaxial cell and securing undrained conditions.

- A new challenge arises with a fully confined biaxial cell. During consolidation drained conditions are desired. This requires a new design to control drained conditions. A proposition was made in Appendix A.1.
- Development of more robust soil sampling tools, tailor made for this biaxial apparatus.
- A new feature in the system control to apply stress control mode apart from strain control mode.

One of the major drawbacks of the biaxial device are the uncontrolled drainage conditions. These require thorough improvements to ensure a controlled testing facility proving undrained conditions. Test not bounded by this requirement might shift the applicability of this biaxial testing facility. Plane strain biaxial tests with sand are executed for drained conditions. Investigating the possibility to perform drained tests could show potential for future studies with sand using the biaxial apparatus.

A trade off should be made to find the admissibility of improving the device. Alternatively commercial biaxial devices available might prove to be a more viable option to perform the intended research work. Commercial biaxial devices allow for plane strain testing of soils with different type constructions and sample cell sizes. The possibility to accurately assess shear banding phenomena and strength parameters is found for one of such devices. A cubical sample is placed and loaded uniaxially from the top. The sample is restricted to deform laterally by two plates.

Conclusively, it is recommended to discontinue further work with the device. Particularly considering the financial obligation and time commitment required to overcome the list of recommended improvements. It is considered to be too challenging to continue work on the device for future soil test studies.

# 10. References

- Abed, A., Korkiala-Tanttu, L. (2018). Stability analysis for road-cutting. Review, recommendations, and examples. 10.13140/RG.2.2.10562.02244.
- Allersma, H.G.B. (1993). New design of a biaxial apparatus for soft soils. Report no. 354, Delft University of Technology.
- Bishop, A. W. (1966). The strength of soils as engineering materials. *Giotechnique* 16, 91-128.
- Bizzarri, A., Allersma, H.G.B., Koehorst, B.A.N. (1995). Preliminary tests on soft clay with a biaxial apparatus. *Proc. Int. Symp. on Compression and Consolidation of Clayey Soils, Hiroshima, Vol I*, pp. 27-32.
- Bizzarri, A., Allersma, H.G.B. (1998). Creep tests on reconstructed soft clay, by means of a biaxial device. *Problematic soils, Yanagisawa, Moroto, Mitachi (eds)*, pp. 645-648
- Bizzarri, A. (2002). Creep tests on reconstituted soft clay, performed by means of a biaxial device. *Learned and Applied Soil Mechanics: A tribute to Dr Arnold Verruijt*. DOI: 10.1201/NOE9058093578-11.
- Brannon, R. (2007). *Elements of Phenomenological Plasticity: Geometrical Insight, Computational Algorithms, and Topics in Shock Physics*. 10.1007/978-3-540-68408-4\_6.
- Brinkgreve, R. (2019). *Plasticity theory, Mohr-Coulomb model. Lecture 11 Behaviour of Soils & Rocks*, Technical University Delft.
- Cheng, X., Allersma, H.G.B. (2004). Strain rate dependent behaviour, material instability and localization of organic soft clay. *Engineering Practice and Performance of Soft Deposit*, pp. 75-80.
- Cheng, X., Janssen, H., Barends, F.B.J., den Haan, E.J. (2003). A combination of ESEM, EDX and XRD studies on the fabric of Dutch organic clay from Oostvaardersplassen (Netherlands) and its geotechnical implications. DOI: 10.1016/j.clay.2003.11.002
- Cruz José, A., Hoyos, L.R., Lizcano, A. (2012). Unsaturated soils: research and applications : volume 1. In *Unsaturated soil response under plane strain conditions using a servo/suction-controlled biaxial apparatus* (pp. 31–38). essay, Berlin, Heidelberg : Springer Berlin Heidelberg : Springer. [https://doi.org/10.1007/978-3-642-31116-1\\_5](https://doi.org/10.1007/978-3-642-31116-1_5)
- Davis, R.O., Selvadurai, A. P. S. (2002). *Plasticity and Geomechanics*. Cambridge University Press.

Den Haan, E.J. (1995). Veen (en organische klei), een grondmechanisch probleem. KIVI open sprekersdag 20 juni 1995.

Den Haan, E.J., (1999). Dutch Cell Test or Triaxial Test. *Geotechniek* 3, No.1. pp. 5-11

Den Haan E.J., Grognet M. (2014). A large direct simple shear device for the testing of peat at low stresses. *Géotechnique Letters* 4 no 4 p. 283 – 288.

Drucker D.C., Prager, W. (1951). *Soil Mechanics and Plastic Analysis or Limit Design*. Brown University. 1 ed.

Fauziah, M., Nikraz, H. R. (2008). The behaviour of unsaturated compacted clay under plane strain condition, 3rd International Conference on Evaluation, Monitoring, Simulation, Management and Remediation of the Geological Environment and Landscape, The New Forest, Ashurst Lodge, UK., pp. 77-86.

Griffiths, D., Huang, J. (2009). Observations on the extended Matsuoka–Nakai failure criterion. *International Journal for Numerical and Analytical Methods in Geomechanics*. 33. pp. 1889 - 1905. 10.1002/nag.810.

Hambly, E.C., Roscoe, K.H. (1969). Observations and predictions of stresses and strains during plane strain of 'wet' clays. *Proc. 7<sup>th</sup> Int. Conf. Soil Mech.* 1, pp. 173-181.

Han, C., Vardoulakis, I. G. (1991). Plane-strain compression experiments on water-saturated fine grained sand. *Geotechnique* V41, N1, March 1991, P49-78

Kelly, P. (2013). *Solid Mechanics Lecture Notes - An Introduction to Solid Mechanics*. Auckland: The University of Auckland.

Kumruzzaman, M., Yin, J. (2011). Stress-strain behaviour of completely decomposed granite in both triaxial and plane strain conditions. *Malaysian Journal of Civil Engineering*, 23(1). <https://doi.org/10.11113/mjce.v23.15810>

Lagioia, R., Panteghini, A. (2016). On the existence of a unique class of yield and failure criteria comprising Tresca, von Mises, Drucker-Prager, Mohr-Coulomb, Galileo- Rankine, Matsuoka-Nakai and Lade-Duncan. *Proc. R. Soc. A* 472, 1–21.

Matsuoka, H., Nakai, T. (1974). Stress-deformation and strength characteristics of soil under three different principal stresses. *Proc. JSCE*, No. 232, pp. 59-70.

Matsuoka, H., Nakai, T. (1985). Relationship among Tresca, Mises, Mohr-Coulomb and Matsuoka-Nakai failure criteria. *SOILS AND FOUNDATIONS*. Vo1.25, No.4, 123-128, Dec. 1985 Japanese Society of Soil Mechanics and Foundation Engineering

Matsuoka, H., Yao, Y-P., Sun, D.A. (1999). The Cam-Clay models revised by the SMP criterion. *SOILS AND FOUNDATIONS*. 39. 81-95. 10.3208/sandf.39.81.

Muir Wood, D. (1990). *Soil Behaviour and Critical State Soil Mechanics*. Cambridge University Press.1. <https://doi.org/10.1017/CBO9781139878272.004>

Nielsen J., Sixhøj Jepsen K. (2019). Elasto-Plastic Constitutive Modelling of Geotechnical Material. Aalborg University.

Panteghini, A., Lagioia, R. (2013). A fully convex reformulation of the original Matsuoka-Nakai failure criterion and its implicit numerically efficient integration algorithm. *Int. J. Numer. Anal. Meth. Geomech.* 2014; 38:593–614.

PLAXIS 2D Material Models Manual. (2021). PLAXIS CONNECT edition V22.00.

Potts, D. M. & Zdravkovic, L. (1999). *Finite element analysis in geotechnical engineering: theory.* London, UK: Thomas Telford. pp. 440

Ramamurthy, T., Tokhi, V.K. (1989). Plane strain strength from triaxial test. 12th International Conference on Soil Mechanics and Foundation Engineering (Rio De Janeiro)

Roscoe, K.H. & Burland, John. (1968). *On the Generalized Stress-Strain Behavior of Wet Clays.* Engineering plasticity, Cambridge University Press. pp. 535 – 689.

Satake, M. (1982). Fabric tensor in granular materials. *Proceedings of IUTAM Symposium on Deformation and Failure of Granular Materials, Delft, Balkema*, pp. 63-68.

Sitters, C. (2006). *Material Models for Soil and Rock.* TU Delft Course: CT4360 (2) – 90

Sterpi, D. (2000). Influence of the kinematic testing conditions on the mechanical response of a sand. *Computers and Géotechnique*, 26, pp. 23-41.

Teunissen, J.A.M. (2022). The influence of the intermediate stress on the plane strain strength. *Computers and Geotechnics*, Volume 152, 104983, ISSN 0266-352X, <https://doi.org/10.1016/j.compgeo.2022.104983>.

Tigchelaar, J. (2001). Eindrapportage Experimenteel onderzoek van het gedrag van organische klei. *Grondmechanica Delft*; CO-710203/28.

TML. (2021). TML Pam E-2020D Transducers 2021. Retrieved from: [https://www.tml.jp/eng/documents/transducers/KPE-PB\\_KPG-PA.pdf](https://www.tml.jp/eng/documents/transducers/KPE-PB_KPG-PA.pdf)

Topolnicki, M. (1990). Observed stress-strain behaviour of remoulded saturated clay and examination of two constitutive models. *Publications of the Institute of Soil and Rock Mechanics in Karlsruhe*, no. 107.

Van Duinen, A. (2014). Handreiking voor het bepalen van schuifsterkte parameters. WTI 2017 Toetsregels Stabiliteit. Deltares rapport 1209434-003-GEO-0002, 18 december 2014, definitief.

Van Loon, A.J., Wiggers, A.J. (1975). Holocene lagoonal silts (formerly called “sloef”) from the Zuiderzee. *Sedimentary Geology* 13. pp. 47–55.



Vardoulakis, I. G. (1977). Scherfugenbildung in Sandkörpern als Verzweigungsproblem. PhD thesis. Institutes für Bodenmechanik und Felsmechanik der Universität Fridericiana in Karlsruhe, Germany.

Vardoulakis, I. G., Goldscheider, M. (1981). Biaxial apparatus for testing shear bands in soils. Proc. 10<sup>th</sup> Int. Conf. Soil Mech. Fndn. Engng, Stockholm, 4. pp. 819-824.

Wanatowski, D., Chu, J. (2006). Stress-Strain Behavior of a Granular Fill Measured by a New Plane-Strain Apparatus. Geotechnical Testing Journal. 29. pp. 149-157. 10.1520/GTJ12621.

Wille Geotechnik. (2023). Biaxial systems. Retrieved from: [https://www.wille-geotechnik.com/ru/Biaxial\\_Systems.html](https://www.wille-geotechnik.com/ru/Biaxial_Systems.html)

Wood, C. C. (1958). Shear strength and volume change characteristics of compacted soil under conditions of plane strain, PhD Thesis, University of London.

Wroth, C.P. (1984). The interpretation of in situ soil tests. Geotechnique 34. no 4. pp. 449-489.

Zwanenburg, C., Lange, D. A., Konstantinou, M. (2018). Povm validatie, uitgangspunten en lange termijnontwikkeling. Report 11200999-004-GEO-0002.

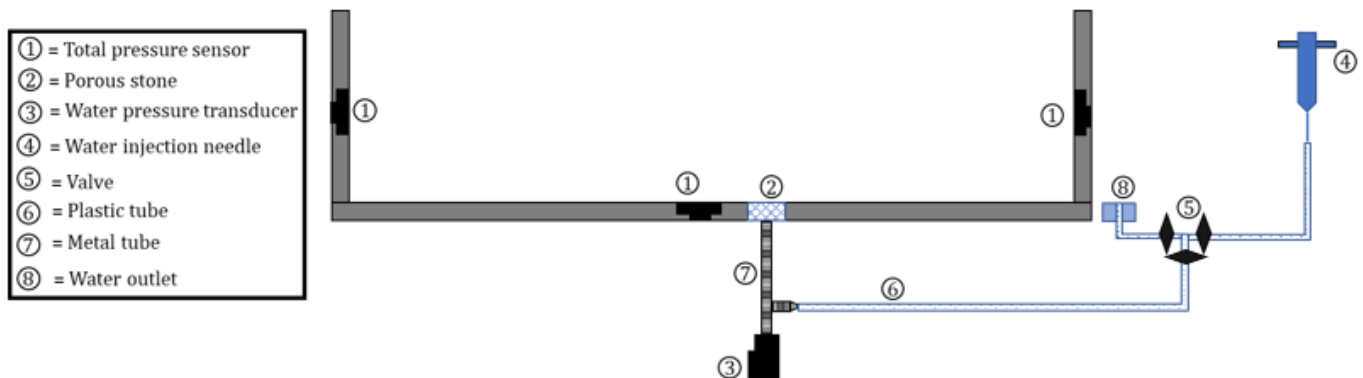
Zwanenburg, C., de Lange, D.A., Teunissen, J.A.M. (2019). Lateral stress measurements in DSS testing. Proc. 17<sup>th</sup> ECSMGE Reykjavik. 10.32075/17ECSMGE-2019-0162.

# Appendix A. Pore pressure measurement.

## A.1 – Preliminary design drainage control.

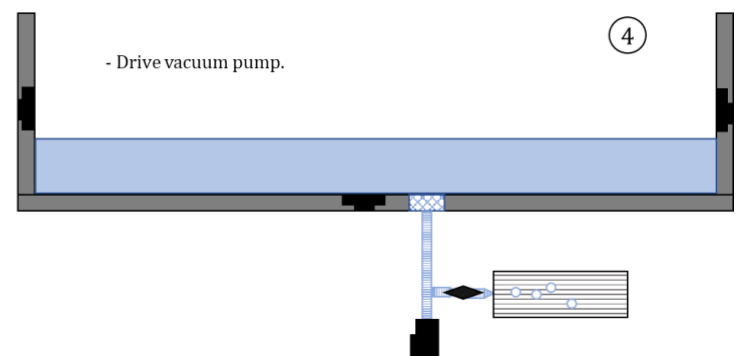
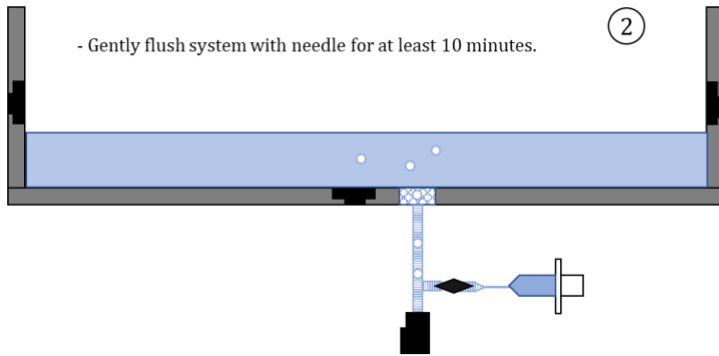
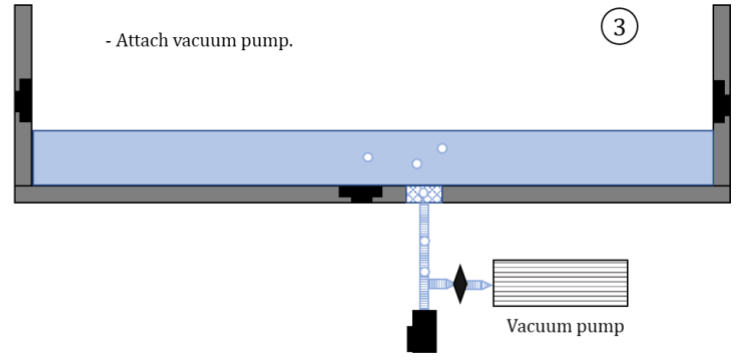
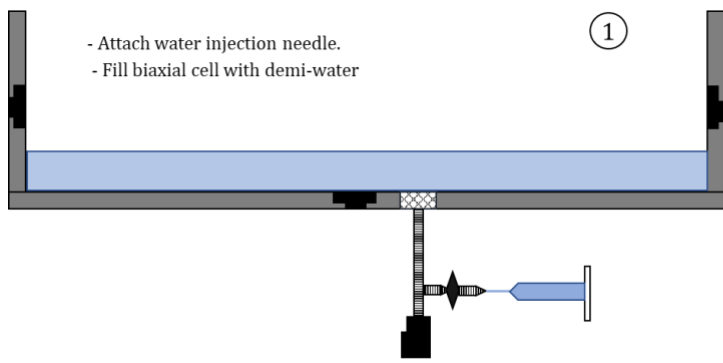
For the preliminary design to control the drainage the design below is made. Dimensions presented are not up to scale. To saturate the system the water injection needle marked with 4, is filled with demi-water. The valve towards the water outlet, marked with 8, is closed and the valve towards the needle is opened. Water coming from the needle is flushed through the system (plastic tubes and metal tube). The plastic tube towards the water outlet is flushed in the same manner. This leads to a saturated system of metal and plastic tubes.

By setting the valves at mark 5 open or closed the soil can be displaced in either drained or undrained conditions. During drained conditions the valve towards the water outlet are opened. The valve towards the needle closed. The water outlet is placed at exact the same height as the porous stone/clay contact interface. Any excess pore pressure developed during displacement of the soil is intended to flow out of the system through this water outlet.



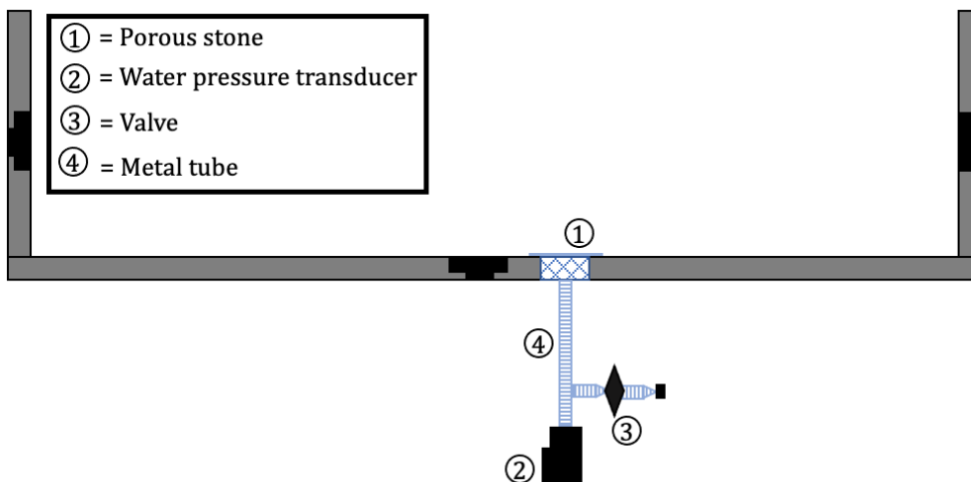
## A.2 – Steps for saturating system.

Below are the steps shown to saturate the metal tubes and porous stone before a test. This is done to increase the chance of measuring excess pore pressure at the water pressure transducer at the bottom of the metal tube. The four steps taken are shown with the chronological sequence corresponding to the ascending order of the numbers in the top right corner.



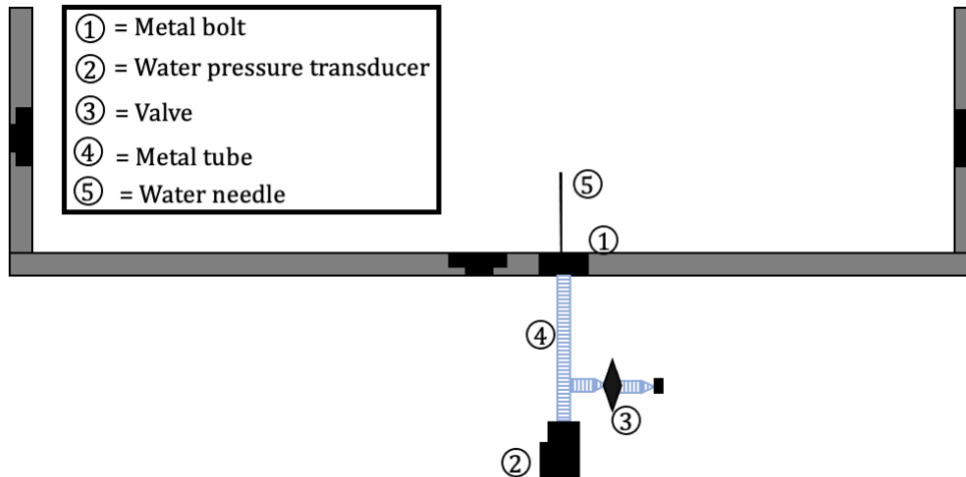
### A.3 – Design pore pressure measurement with porous stone

This design intends to measure the excess pore pressure at the water pressure transducer using a porous stone. The valve is closed giving undrained conditions. The system is saturated according to the steps of figure 2.2. After this procedure, the system is kept out of contact with air by resting a small layer of water above the porous stone.



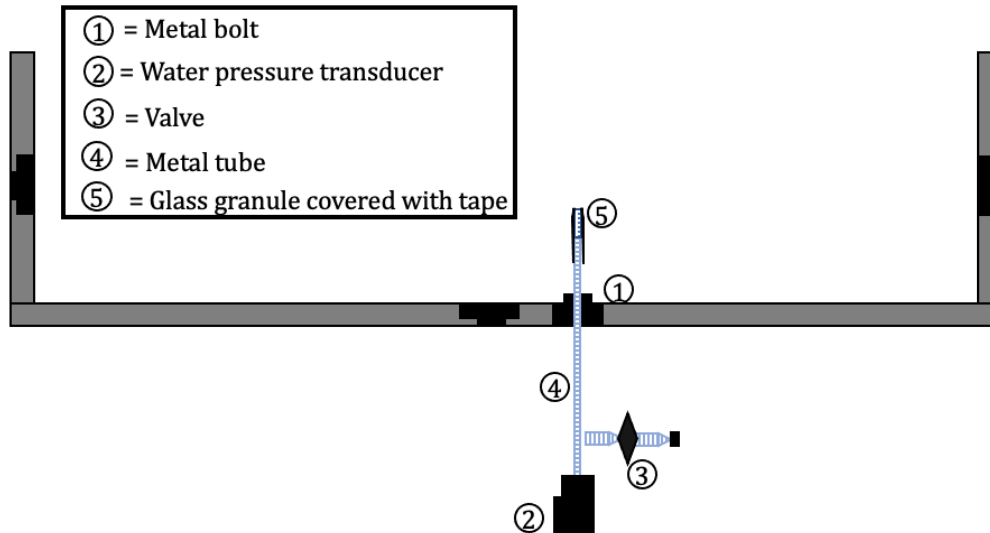
#### A.4 – Design pore pressure measurement with water needle

A proposed design, intended to measure the excess pore pressure at the water pressure transducer, uses a water needle. A water needle is installed instead of the porous stone. The water needle is pushed into the soil sample. The valve is closed giving undrained conditions. To prevent soil clogging the needle, a fine string is driven through the needle.



#### A.5 – Design pore pressure measurement with glass granule

This design intends to measure the excess pore pressure at the water pressure transducer using a water needle pushed into the soil sample. The valve is closed giving undrained conditions. A glass granule is installed instead of the porous stone. Tape is used to connect the glass granule to the metal tube. The glass granule makes contact at approximately 2.5 cm into the sample.



### A.6 - Graphical interface input panel

The input panel used to control the biaxial apparatus is shown below with annotation. Two parts of the panel are distinguished. A part to control the apparatus and a part giving the recorded output.

Apart from the highlighted parts, a 2D figure shows the position of the horizontal plates. The four circumferences show the current position, home position, intended position related to relative displacement and intended position related to absolute displacement.

COM PORT

physical channels 0  
Dev1/Ai0:3

physical channels 1  
Dev0/Ai0:3

Baudrate  
38400

2D Picture 2

Relative Move

Absolute Move

Home Home Button

STOP

Velocity (VE)  
0,00021

Distance A: -10

Distance B: -10

Distance C: -10

Distance D: -10

Pressure> Max

MaxPressure Treshold: 1

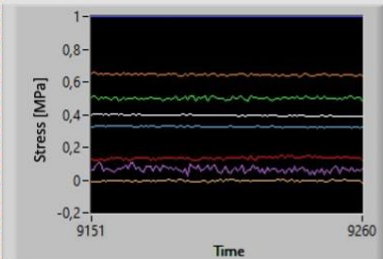
-43,577	Current pos 0	-5	Set Pos 0	Enabled 0	Home 0	Status code 0
-43,477	Current pos 1	-10	Set Pos 1	Enabled 1	Home 1	Status code 1
-5,8	Current pos 2	-5	Set Pos 2	Enabled 2	Home 2	Status code 2
-43,577	Current pos 3	-5	Set Pos 3	Enabled 3	Home 3	Status code 3
-5,8	Current pos 4	-5	Set Pos 4	Enabled 4	Home 4	Status code 4
-5,8	Current pos 5	-5	Set Pos 5	Enabled 5	Home 5	Status code 5
-43,477	Current pos 6	-10	Set Pos 6	Enabled 6	Home 6	Status code 6
-5,8	Current pos 7	-5	Set Pos 7	Enabled 7	Home 7	Status code 7

Legend:

- 1 = Channel to data acquisition devices
- 2 = Maximum pressure settings
- 3 = Current and set position
- 4 = Absolute or relative displacement A, B, C or D
- 5 = Home and stop control buttons
- 6 = Status of step motor
- 7 = Displacement in mm/s

The panel related to the output is shown below. Two figures give the calculated stress and displacements over time. The raw sensors data corresponds to the values directly measured by the sensor. By calibrating the sensors, the offset and gain are retrieved. These result in the calculated data.

**Pressure Sensors**



P 1

P 2

P 3

P 4

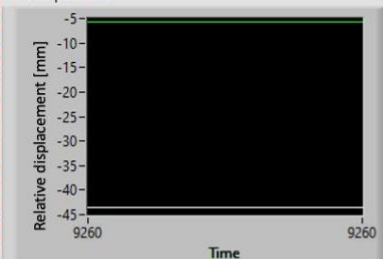
P 5

P Porie

MaxPressure

calc data	sensor data	Gain	Offset
0,391871	0,204279	5,646	-0,7615
0,63284	0,168904	5,575	-0,3088
0,487089	0,0974607	6,148	-0,1121
0,326362	0,0641137	6,739	-0,1057
0,123156	0,216107	5,771	-1,124
0,0681117	0,0408787	62,04	-2,468
-0,0164196	0,110273	6,866	-0,77357
0	-0,00116944	0	0
-43,577	-43,577	1	0
-43,477	-43,477	1	0
-5,8	-5,8	1	0
-43,577	-43,577	1	0
-5,8	-5,8	1	0
-5,8	-5,8	1	0

**Motor positions**



Pos 1

Pos 2

Pos 3

Pos 4

Pos 5

Pos 6

Pos 7

Time [s] **6129**

file path (dialog if empty) **C:\jkampf\7-2.txt**

Record time [s] **1**

Save to file?

- ❶ = Stress and relative displacement output graphs
- ❷ = Calculated data
- ❸ = Raw data with sensor gain and offset
- ❹ = Recording of data

124



## Appendix B. General relation stress invariants

A general relation of stress invariants is shown below in Formula B.1.  $J_1^\sigma$ ,  $J_2^\sigma$  and  $J_3^\sigma$  are the invariants of the Cauchy stress tensor (Sitters, 2006). The solution of this equation yields three real eigenvalues  $\sigma_i$ , previously introduced as the principal stresses.

$$\sigma^3 - J_1^\sigma \sigma^2 + J_2^\sigma \sigma - J_3^\sigma = 0 \quad (B.1)$$

The normal invariants can be expressed by the principal stresses as:

$$J_1^\sigma = \sigma'_1 + \sigma'_2 + \sigma'_3 \quad (B.2)$$

$$J_2^\sigma = \sigma'_1 \sigma'_2 + \sigma'_2 \sigma'_3 + \sigma'_3 \sigma'_1 \quad (B.4)$$

$$J_3^\sigma = \sigma'_1 \sigma'_2 \sigma'_3 \quad (B.5)$$

According to Sitters (2006), the deviatoric invariants are related to the normal invariants by:

$$J_2^{\sigma^d} = J_2^\sigma - \frac{1}{3}(J_1^\sigma)^2$$

$$J_3^{\sigma^d} = J_3^\sigma - \frac{1}{3}J_1^\sigma J_2^\sigma + \frac{2}{27}(J_1^\sigma)^3 \quad (B.6)$$

The third deviatoric invariant can also be written as:

$$J_3^{\sigma^d} = (\sigma'_1 - p') \times (\sigma'_2 - p') \times (\sigma'_3 - p') \quad (B.7)$$

Lastly, the Lode's angle can be related to the deviatoric stress and the third deviatoric invariant with the following combination:

$$\sin 3\theta = \frac{27 J_3^{\sigma^d}}{2 q^3} \quad (B.8)$$

# Appendix C. Constitutive models

One of the goals for this thesis is to understand, analyse and predict the way the soil in the biaxial device behaves. It is difficult to perform an analysis in which full understanding of the soil and the biaxial device is known, permitting a complete and accurate description of soil and device in an analysis. In general, this is true for geotechnical engineering where it is rarely possible to perform such an end-to-end analysis (Muir Wood, 1990).

This does not rule out the possibility to understand the behaviour of our experiment. Intelligent simplifications of reality make it possible to analyse reality with simplified models (Muir Wood, 1990). There are various models which enable to analyse the mechanical behaviour of soils. All these models may contain different features, complexity, or degree of accuracy.

The most applicable model may be found by analysing the behaviour of the soil in the biaxial device with its behaviour using a certain constitutive model. This can be numerically analysed using Soil Test module PLAXIS. There are several models standard available in this programme. The most applicable models, for the scope of this thesis, found in PLAXIS are clarified below.

## C.1 Elasticity

The least complex soil behaviour to describe is elastic behaviour. For an elastic material there is a one-to-one relationship between stress and strain. If a stress is applied and subsequently removed the material returns to its pristine condition. The behaviour is described according to Hooke's law. The elastic strains related to the x, y and z direction are given in formulas C.3, C.4 and C5, respectively, according to Hooke's Law. The shear stress and shear strains are not defined below as these elements do not play a part in the test setup presented in this thesis. Hooke's law of elasticity has two independent parameters: Young's modulus  $E$ , defined in equation C.1, and Poisson's ratio  $\nu$ , defined in equation C.2.

$$E = \frac{d\sigma_1}{d\varepsilon_1} \quad (C.1)$$

$$\nu = -\frac{d\varepsilon_3}{d\varepsilon_1} \quad (C.2)$$

$$\varepsilon_{xx} = \frac{1}{E}\sigma'_{xx} - \frac{\nu}{E}\sigma'_{yy} - \frac{\nu}{E}\sigma'_{zz} \quad (C.3)$$

$$\varepsilon_{yy} = -\frac{\nu}{E}\sigma'_{xx} + \frac{1}{E}\sigma'_{yy} - \frac{\nu}{E}\sigma'_{zz} \quad (C.4)$$

$$\varepsilon_{zz} = -\frac{\nu}{E}\sigma'_{xx} - \frac{\nu}{E}\sigma'_{yy} + \frac{1}{E}\sigma'_{zz} \quad (C.5)$$

To illustrate the effect for plane strain conditions, a strain increment in z-direction, the out of plane direction, is set to be zero, see formula C.6. Consequently, the stress increment in the z-direction can be calculated using the two other stresses, shown in formula C.7.

$$d\varepsilon_{zz} = -\frac{\nu}{E}d\sigma'_{xx} - \frac{\nu}{E}d\sigma'_{yy} + \frac{1}{E}d\sigma'_{zz} = 0 \quad (C.6)$$

With:

$$d\sigma'_{zz} = \nu(d\sigma'_{xx} + d\sigma'_{yy}) \quad (C.7)$$

The stress increment in the out of plane direction depends on the strain increments applied in the x- and y- direction. This is given by the following formula:

$$d\sigma'_{zz} = \frac{\nu E}{(1-2\nu)(1+\nu)}[\varepsilon_{xx} + \varepsilon_{yy}] \quad (C.8)$$

## C.2 Elastoplastic model

The elastic behaviour is not suitable to fully model soil behaviour. For soils there can be multiple states of strain related to one state of stress and vice versa (Muir Wood, 1990). It occurs that the previous maximum load conditions are exceeded. Subsequently, a loaded soil following a deformation path might not follow the reverse path when the load is removed. Hence, permanent strain is found. This type of behaviour can be described with aid of an elasto-plastic model where strain can be decomposed in an elastic part and a plastic part. Plasticity involves irrecoverable, permanent strains which remain on the sample as stress is removed. Two parts can be distinguished for plasticity in a constitutive model. The first part is yielding described in Chapter 6.

Another part of the soil response which is implemented in a constitutive model is the plastic potential, given by  $g$ . This represents the deformation of the soil occurring once yielding has been reached.

The yield surface and the plastic potential surface can be chosen to be identical. If so, they obey the so-called law of associated flow. The plastic strain can be shown as vectors in the direction of the outward, normal to the yield surface (PLAXIS 2D Material Models Manual, 2021).

For certain models the yield function differs from the plastic potential function. The Mohr Coulomb yield function, introduced in Chapter 7, overestimates dilatancy when using the law of associated plasticity. Therefore, separately a yield function and a plastic potential function, annotated by  $g$ , are given. Non-associated plasticity is the term used when  $f \neq g$ .

The last aspect of an elastoplastic model is a description of how the yield locus expands. For some models the yield surface is not fixed and expands due to plastic deformation. The *hardening rule* describes the expansion of the yield surface (Muir Wood, 1990).

### C.3 Cam-clay model

A particular elastic-plastic model widely used for numerical soil analysis is the Cam-clay type model. The modified Cam-clay model was described by Roscoe et al (1968). It was based on the theory and experimental results of clays under triaxial stress condition (Matsuoka et al., 1999).

The starting point is the relationship between specific volume and mean effective stress. Elastic unloading and reloading are given by expression C.9. This formula gives a set of swelling lines shown in Figure 123. Parameter  $\kappa$  gives the slope of these lines and determines the compressibility of the soil in unloading and reloading.

$$e - e^0 = -\kappa \ln\left(\frac{p'}{p_0'}\right) \quad (C.9)$$

The model also consists of a straight virgin consolidation line (normal compression line) given by equation C.10 and also shown in Figure 123. This occurs when a soft soil sample is slowly compressed under isotropic and perfectly drained stress conditions. The parameter  $\lambda$  is the slope of the normal compression, and  $N$  is the specific volume of the normal compression line at unit pressure. If the state of the soil is on the virgin consolidation line it is being consolidated normally. If it is under the virgin consolidation line it is overconsolidated implying elastic recoverable changes in volume.

$$e - e^0 = -\lambda \ln\left(\frac{p'}{p_0'}\right) \quad (C.10)$$

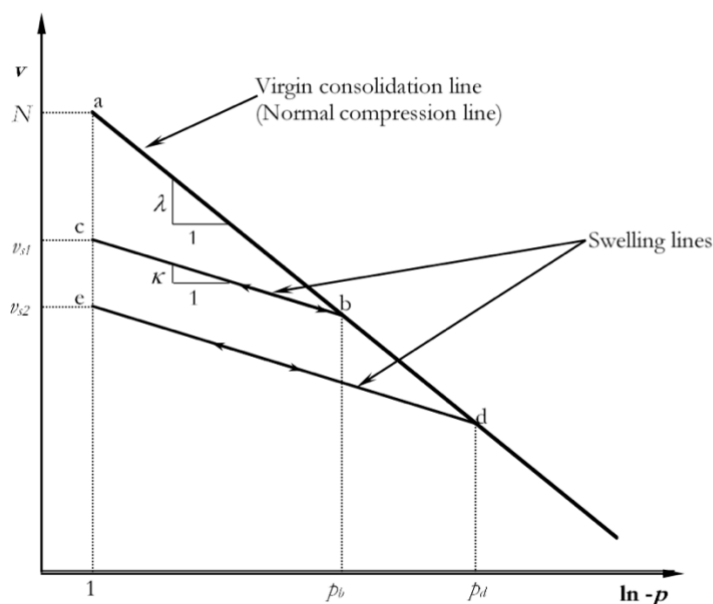


Figure 122: Void ratio versus mean stress for clay with indicated Cam-Clay parameters. (Rocscience, 2021)

The yield criterion for the modified Cam-clay model is given by Formula C.11. It is described in terms of invariants  $p'$ , the mean effective stress and  $q$ , the deviatoric stress.  $M$  is the slope of the critical state line in the  $p' - q$  plot and  $p'_0$  is the isotropic preconsolidation pressure.

$$f = q - M^2(p'p'_0 - p'^2) \quad (C.11)$$

There are two advantages of the formulation described above worth mentioning. Firstly, it has a relatively simple yield surface which depends on solely one shape parameter,  $M$ . Secondly the development of the Cam clay model is based on initial isotropic compression on reconstituted soils, hence parameter  $p'_0$  (Muir Wood, 1990). The starting state of isotropic compression may not be close to reality but is easy to apply to a soil sample.

For  $f = 0$  the yield criterion forms a yield surface in the shape of an ellipse in the  $p' - q$  plane, shown in Figure 124. This representation is based on the conventional triaxial compression test. Triaxial extension can be found by allowing  $q$  to have negative values.

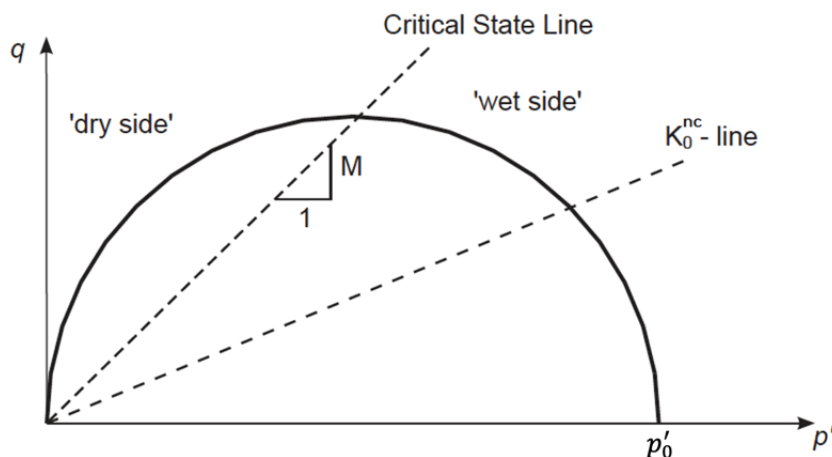


Figure 123: Yield surface of the Cam-Clay model in  $p'$ - $q$  space. (PLAXIS Material models manual, 2021)

The critical state line, with steepness  $M$ , intersects the top of the ellipse and consequently determines the height of the ellipse. It gives the relation between  $p'$  and  $q$  in state of failure, and can be written according to Formula C.12.

$$q = Mp' \quad (C.12)$$

The value of  $p'_0$  determines the length along the  $p'$ -axis of the ellipse. The value of  $p'_0$  will take different values when the soil starts hardening. The yield surface expands at constant shape as seen in Figure 125. The arrow indicates the increment of initial effective stress, marked with A, to a new configuration of effective stress, B. The yield surface will expand from the initial value of  $p'_0 = p'_{0A}$  to a new current value of  $p'_0 = p'_{0B}$ . In fact, an infinite number of surfaces exist, each one corresponding to a different value of  $p'_0$  (PLAXIS Material models manual, 2021).

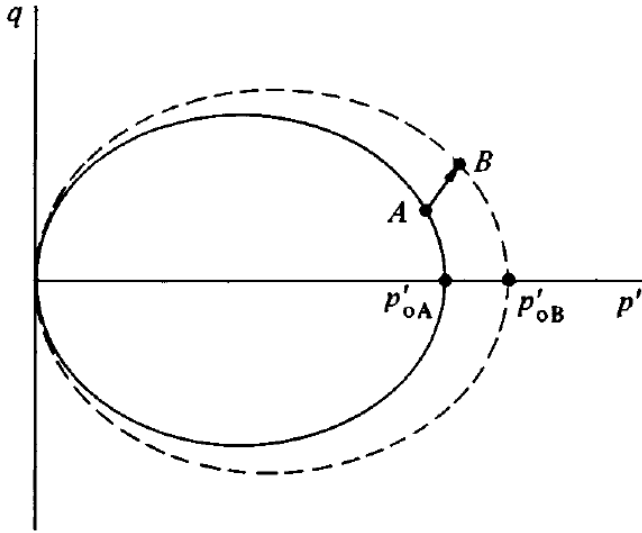


Figure 124: Expanding yield locus due to stress increment. (Muir Wood, 1990)

## C.4 Soft Soil Model

The Soft Soil model is a model which is partially based on Cam-clay theory concepts. In contrast to the Cam-Clay model, the mean effective stress is related to volumetric strain instead of the void ratio (PLAXIS Material models manual, 2021). One of the main features of this model is that it distinguishes between primary loading and unloading/reloading behaviour. It gives a good non-linear formulation of soft soil behaviour, especially for normally consolidated clays.

Formula C.13 can be used to describe the path taken during isotropic unloading and reloading. The compressibility of the soil during this elastic response is determined by parameter  $\kappa^*$ .

$$\varepsilon_v^e - \varepsilon_v^{e0} = -\kappa^* \ln \left( \frac{p' + c \cot \varphi}{p'_0 + c \cot \varphi} \right) \quad (C.13)$$

For normal compression the logarithmic relation between volumetric strain and mean effective stress is given by formula C.14. The compressibility of the soil during primary compression is given by parameter  $\lambda^*$ .

$$\varepsilon_v - \varepsilon_v^0 = -\lambda^* \ln \left( \frac{p' + c \cot \varphi}{p'_0 + c \cot \varphi} \right) \quad (C.14)$$

The yield function of the Soft Soil model is defined as:

$$f = \frac{\tilde{q}^2}{M^2(p' + c \cot \varphi)} + p' - p'_0 \quad (C.15)$$

With  $\tilde{q} = \sigma'_1 + \left( \frac{3 + \sin \varphi}{3 - \sin \varphi} - 1 \right) \sigma'_1$

For the  $f = 0$  the Soft Soil yield function can be shown as an ellipse in the  $p' - \tilde{q}$  plane shown in Figure 126.

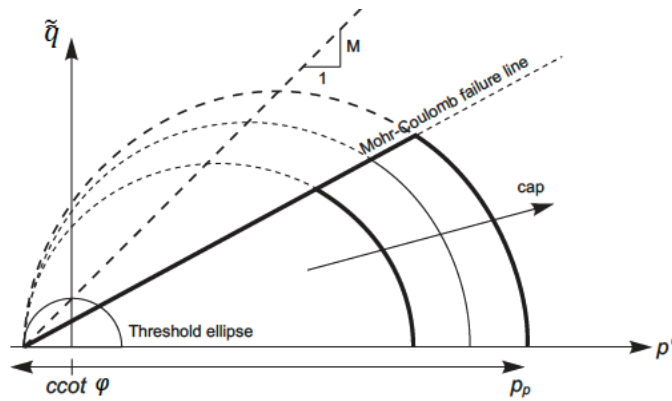


Figure 125: Soft Soil yield surface given in the  $p$ - $q$ -plane (PLAXIS Material models manual, 2021).

The parameter  $M$  is relatively high giving a steep yield cap. This ensures a better  $K_0^{nc}$  stress ratio during primary compression. For the Soft Soil model the critical state line refers to post peak failure. This interpretation differs to the critical state line for the Cam-Clay model, where the critical state line is directly related to failure. In this model, failure behaviour is according to the Mohr-Coulomb strength criterion.

A disadvantage to the Soft Soil model is that it is not suitable for other types of soil than soft soil. Other downfalls are the exclusion of the effect of anisotropy, which could be less convenient when working with organic material, secondary compression, creep and relaxation. These disadvantages are also applicable for the Mohr-Coulomb and Cam-Clay model.